Master Thesis

Simulation of the Swirling Flow of Two Immiscible Fluids in a cylindrical Container

carried out for the purpose of obtaining the degree of

Diplom-Ingenieurin (Dipl.-Ing.in or DI)

submitted at TU Wien

Faculty of Mechanical and Industrial Engineering

by

Zahra REZAEIFAR

Mat.No.: 01329281

under the supervision of

Ao.Univ.Prof. Dipl.-Ing. Dr. techn. Herbert Steinrück

Institute of Fluid Mechanics and Heat Transfer, E322

Wien, April 2024

_____

Affidavit

I declare in lieu of oath, that I wrote this thesis and carried out the associated research myself, using only the literature cited in this volume. If text passages from sources are used literally, they are marked as such.

I confirm that this work is original and has not been submitted for examination elsewhere, nor is it currently under consideration for a thesis elsewhere.

I acknowledge that the submitted work will be checked electronically-technically using suitable and state-of-the-art means (plagiarism detection software). On the one hand, this ensures that the submitted work was prepared according to the high-quality standards within the applicable rules to ensure good scientific practice "Code of Conduct" at the TU Wien. On the other hand, a comparison with other student theses avoids violations of my personal copyright.

Place and Date	*Signature*

Acknowledgements

I would like to express my sincere gratitude to Professor Herbert Steinrück for his invaluable support and guidance during my master's thesis.

I would also like to extend my heartfelt thanks to my husband, Bahram, and my daughter, Helena, for their endless love, understanding, and patience during this time. Their support has been a constant source of strength and motivation.

Contents

English Abstract

In this work, steady, axially symmetric flow is investigated in a vertical cylinder with a rotating lid containing two immiscible liquids of different densities. The flow of both fluids is described by the Navier-Stokes equations, the interface conditions, and the boundary conditions. Since the position of the interface depends on the flow, it is a free boundary value problem.

All occurring variables are related to suitable reference values and the equations are formulated in dimensionless form. In addition to the Reynolds number, the Froude number and Weber number as well as the density and viscosity ratio of the two liquids as well as the height-radius ratio of both liquid layers. In the limit case of a small height-radius ratio, the self-similar flow between two infinitely rotating disks is obtained.

The Navier-Stokes equations and boundary conditions are discretized using a spectral collocation method with Chebyshev polynomials. The resulting equations for the function values at the support points are solved using a solver for nonlinear systems of equations from the NAG program library.

The numerical method is tested on the case of a liquid and the solutions are compared with published solutions. First, self-similar solutions are discussed, then the case of flow in a container in the limit Fr=0, flat interface, is treated. The influence of all dimensionless key figures on the flow or the shape of the interface is then analyzed. It turns out that the Reynolds number has the greatest influence on the flow pattern. The Froude number has the greatest influence on the interface shape. The Weber number has rather little influence on the interface shape. For further stability analysis of the interface, shear stress and the velocity of the fluids at the interface are essential.

Deutsche Kurzfassung

In dieser Arbeit wird die stationäre, axialsymmetrische Strömung in einem vertikalen Zylinder mit rotierendem Deckel untersucht, der zwei nicht mischbare Flüssigkeiten unterschiedlicher Dichte enthält. Die Strömung beider Flüssigkeiten wird durch die Navier-Stokes-Gleichungen, die Grenzflächenbedingungen und die Randbedingungen beschrieben. Da die Lage der Grenzfläche von der Strömung abhängt, handelt es sich um ein freies Randwertproblem.

Alle auftretenden Größen werden auf geeignete Referenzwerte bezogen und die Gleichungen in dimensionsloser Form formuliert. Zusätzlich zur Reynolds-Zahl ist die Froude-Zahl und Weber-Zahl sowie das Dichte- und Viskositätsverhältnis der beiden Flüssigkeiten sowie das Höhen-Radius-Verhältnis beider Flüssigkeitsschichten. Im Grenzfall eines kleinen Höhen-Radius-Verhältnisses erhält man die selbstähnliche Strömung zwischen zwei unendlich rotierenden Scheiben.

Die Navier-Stokes-Gleichungen und die Randbedingungen werden mithilfe einer spektralen Kollokationsmethode mit Tschebyschow-Polynomen diskretisiert. Die resultierenden Gleichungen für Die Funktionswerte an den Stützpunkten werden mit einem Löser für nichtlineare Gleichungssysteme aus der NAG-Programmbibliothek gelöst.

Das numerische Verfahren wird am Fall einer Flüssigkeit getestet und die Lösungen mit veröffentlichten Lösungen verglichen. Zunächst werden selbstähnliche Lösungen diskutiert, dann wird der Fall der Strömung in einem Behälter im Grenzfall Fr=0, ebene Grenzfläche, behandelt. Dann wird der Einfluss aller dimensionslosen Kennzahlen auf die Strömung bzw. die Form der Grenzfläche analysiert. Es zeigt sich, dass die Reynolds-Zahl den größten Einfluss auf das Strömungsmuster hat. Die Froude-Zahl hat den größten Einfluss auf die Grenzflächenform. Die Weber-Zahl hat eher geringen Einfluss auf die Grenzflächenform. Für eine weitere Stabiltätsanalyse der Grenzfläche, sind Scherspannung und die Geschwindigkeit der Flüssigkeiten an der Grenzfläche von wesentlicher Bedeutung.

1 Introduction

The study of rotating flows originates from observations of natural phenomena, such as swirling water in streams and eddying winds across landscapes, which have fascinated scientists and engineers for ages. These swirling motions present challenges that can not be justified with simple explanations [1].

Rotating flows play a critical role in both natural processes and technological applications. In nature, they contribute to atmospheric circulation, ocean currents, and weather patterns. In technology, rotating flows are essential for the design and operation of various products, such as jet engines, pumps, and cyclones. Understanding and modelling rotating flows enables engineers to optimize the performance and efficiency of these devices [1].

By going deeper into the study of rotating flows, a variety of fascinating phenomena that challenge traditional explanations are discovered. These include the formation of vortices and turbulent eddies, the emergence of secondary flows driven by centrifugal and Coriolis forces, and the nonlinear interactions that give rise to resonant behaviours and instabilities [2]. Additionally, the interaction between rotating flows and solid boundaries leads to complex boundary layer dynamics, influencing everything from heat transfer to flow separation [3].

rotation of a cylindrical container filled with one or more fluids is a simple case of rotating fluids, which is not just an interesting subject for theorists but also of direct importance in many areas of engineering such as bearings, computer storage devices, viscometry, rotating machinery, and material processing units [4], [5], [6]. This phenomenon has been both numerically and experimentally studied by many researchers [7], [8], [9].

Fujimoto et al. investigated the interface topology change between two liquids in a cylinder with rotating lid experimentally and it was shown the shape of interface is a strong function of lid speed and the fluids volume fractions and its topology can result in interfacial waves and instability [10]. Using experiments Sharifullin et al. studied the momentum transfer through the interface of two immiscible liquids and shown the circulation of lower liquid is like mono-liquid measurements [9].

To simplify the governing equations for numerical or analytical solution of rotating flows, under certain conditions, axial symmetry flow behaviour can be assumed. Axial symmetry in fluid dynamics refers to a type of flow where the properties of the flow (such as velocity,

pressure, and density) are invariant around an axis of rotation. Axially symmetric flows often occur in cylindrical or conical geometries, where the flow remains consistent along the length of the cylinder or cone [8]. For example, in the experiments by Naumov et al. it was shown that under steady flow at a wide range of rotating speed axisymmetric behaviour is observed and a thin circulation layer in the vicinity of the interface is formed, which was also previously observed in the simulations [11] and confirms the validity of this assumption.

In three-dimensional flows, two stream functions are needed to fully describe the flow, as there are variations in flow properties in both the radial and tangential directions. However, in axisymmetric flows, where the flow properties remain constant around an axis of rotation, a single stream function can be used to describe the entire flow field. This simplification allows for a more straightforward analysis of axisymmetric flows, like the approach used in two-dimensional ideal flow, where only one stream function is required [12].

Similarity solutions are often employed in fluid mechanics to simplify the analysis of complex flow problems. When dealing with rotating flows with axial symmetry, similarity solutions can provide valuable insights into the behaviour of the flow field. In such cases, the governing equations of motion can often be reduced to a set of dimensionless equations through appropriate scaling [13].

Salnikov et al. compared different simulation approaches for simulation of swirling non-miscible fluids and checked them against particle image velocimetry measurements. They found out both lattice Boltzmann (LBM) and finite volume methods delivers reliable predictions in comparison with measurements but just LBM could capture the velocity shift on the interface [14].

Yang et al. investigate the flow induced by a rotating disk at the bottom of a cylindrical tank using numerical techniques and laser-Doppler velocimetry measurements. Their study elucidates the toroidal flow structure and its dependence on fluid-layer aspect ratios, particularly in the high Reynolds number regime where the flow becomes unsteady and three-dimensional [15]. Rashkovan et al. present a numerical study of liquid flows within a vertical circular cylinder with a rotating bottom, investigating the appearance of polygon shapes resulting from the rotating bottom disk. Their simulations offer insights into the mechanisms and characteristics of polygon flow structures [16].

Kahouadji and Martin Witkowski studied the numerical and experimental investigation of flow induced by a rotating disk at the bottom of an open fixed cylindrical cavity. Their study

utilizes steady axisymmetric Navier-Stokes equations solved using a Newton-Raphson algorithm, with a particular emphasis on achieving a zero normal stress balance at the free surface interface. Notably, their findings reconcile discrepancies between first-order approximations and full numerical simulations regarding free surface deflection [17].

Exploring the characteristics of flows induced by rotating disks in cylindrical tanks, provided insights into axisymmetric steady solutions and transitions to unsteady and three-dimensional flow regimes at high Reynolds numbers which enhances understanding of toroidal flow structures and spatio-temporal fluctuations [18].

The linear stability of confined potential vortices with free surfaces which was studied by Mougel et al. revealed novel resonances attributed to over-reflection phenomena in swirling flows driven by rotating bottom plates. This helped with understanding of instability mechanisms in free-surface rotating flows [19].

In this study, the flow in a vertical cylinder filled with two immiscible liquids of different densities is investigated. The rotation of the upper lid of the cylinder induces a complex flow pattern in the liquids. The aim is to investigate the flow dynamics in both fluids, as well as the displacement of the interface between them, which is known to induce instability. This instability is characterized by high-amplitude waves resulting from interface displacement [23].

2 Problem Formulation

In this section mathematical formulation and framework needed for the current study will be presented. Starting with governing equations, the needed assumptions to simplify them will be introduced and at the end similarity solution and its application to the current research will be discussed. For the sake of consistency, in this document, dimensional quantities are denoted with ~, while non-dimensional quantities are indicated without it.

The main equations for resolving hydrodynamics of two immiscible fluids are continuity and Navier-stokes. In the following these two equations and their use for this study will be discussed in detail.

Our system, as depicted in the following figure, requires a solution in cylindrical coordinates due to its inherent structure. This choice ensures that the equations are properly governed and solved within this coordinate system.

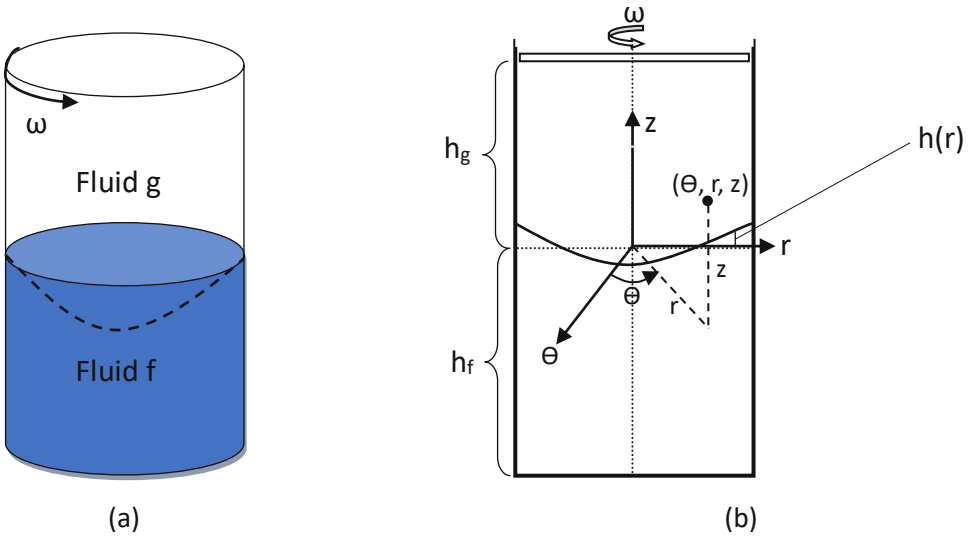

Figure 1: Problem schematic of two non-mixing fluids in a closed vertical cylinder with rotating lid, (a) heavier fluid (Fluid f) and lighter fluid (Fluid g), (b) used cylindrical coordinates, interface function (h(r)) and fluids heights

The utilized geometry for the simulations is a vertical cylinder with a radius of R and a height of H, with a lid that is rotating with angular velocity omega (ω). Inside the vessel is filled with two non-mixing fluids. The two fluids are assumed to have different densities (ρ_1, ρ_2), viscosities (μ_1, μ_2) and other physical properties, which can affect the flow behavior. The rotating lid introduces a centrifugal force, which causes the fluids to move and creates a variety of flow patterns, including vortices, shear layers, and boundary layers. The fluids do

not mix, which means that there is a distinct interface between them, and the flow characteristics can change significantly near this interface. When two immiscible fluids are rotated within the cylinder, the interface between them no longer remains flat. Consequently, it becomes necessary to calculate and account for the shape of this interface in the calculations. The movement of this interface from the flat case, denoted as 'h,' is depicted in Figure 1 and is a function of the radial distance 'r'.

To govern and solve the equations to determine the flow of both fluids, the following assumptions are considered:

- Both fluids are Newtonian, it assumes that the relationship between the shear stress and the rate of strain is linear, which allows for the use of simpler constitutive equations.
- The system is in a steady state. It means that the flow parameters do not change with time. This simplifies the equations by removing the time derivatives, making them easier to solve.
- There is axial symmetry. It means that the flow properties do not vary in the axial direction (along the length of the cylinder). This reduces the problem from three dimensions to two dimensions, simplifying the equations and making them easier to solve.

2.1 The Continuity Equation

Applying mass conservation of mass to an infinitesimal volume yields the continuity equation [20]:

$$\frac{\partial \rho}{\partial t} + \nabla \cdot (\rho \vec{V}) = 0. \tag{2-1}$$

The mentioned equation is generic and can be used in any coordinate system. In the current study liquid flow in a cylindrical vessel is studied, therefore rewriting the equation considering cylindrical coordinates, makes it easier in discretization and relevant assumptions. The continuity equation in cylindrical coordinates looks as following:

$$\frac{1}{\tilde{r}}\frac{\partial(\tilde{r}\tilde{u})}{\partial \tilde{r}} + \frac{1}{\tilde{r}}\frac{\partial \tilde{v}}{\partial \tilde{\theta}} + \frac{\partial \tilde{w}}{\partial \tilde{z}} = \nabla \cdot \vec{\tilde{V}} = 0. \tag{2-2}$$

2.2 The Navier Stokes Equations

Dynamically describing fluid motion involves applying Newton's second law to an infinitesimal fluid particle of mass $d\tilde{m}$ and volume $d\tilde{V} = d\tilde{x}\, d\tilde{y}\, d\tilde{z}$ This application leads to the derivation of the specific form of the momentum conservation equation. Writing Newton's second law as vector:

$$d\vec{\tilde{F}} = d\tilde{m}\frac{D\vec{\tilde{V}}}{D\tilde{t}} = \rho d\tilde{V}\,\frac{D\vec{\tilde{V}}}{D\tilde{t}}. \tag{2-3}$$

The forces that act on fluid elements are body forces and surface forces, where surface forces include normal and shear forces.

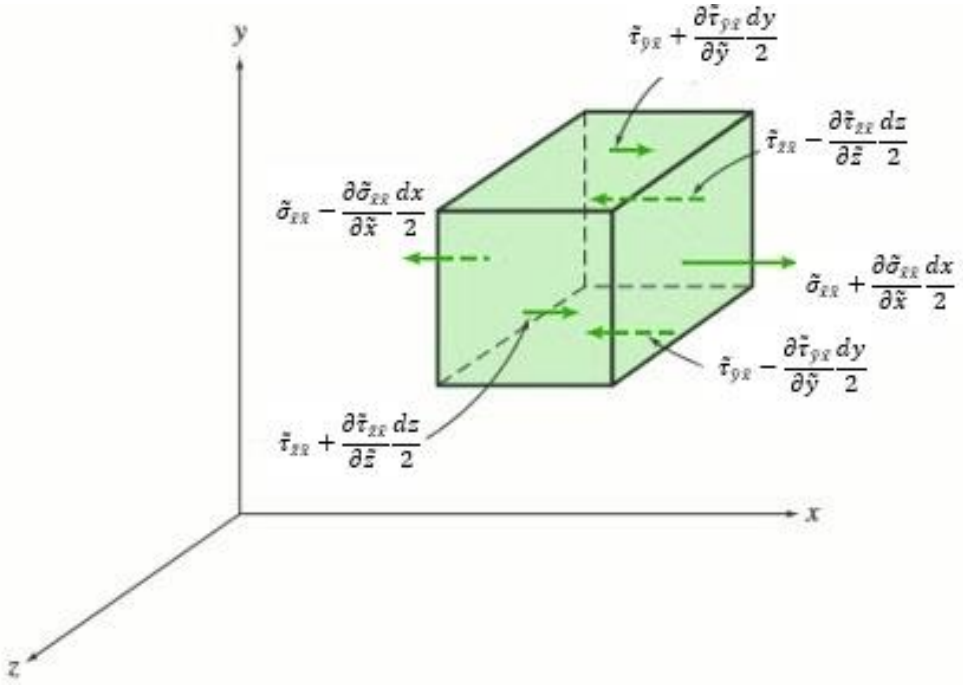

Figure 2: Stresses in x-direction on a fluid element.

By summing the surface forces in the x-direction, the surface force on the fluid element in the $\tilde{x}$ -direction can be determined as following:

$$d\tilde{F}_{S_{\tilde{x}}} = \left(\frac{\partial \tilde{\sigma}_{\tilde{x}\tilde{x}}}{\partial \tilde{x}} + \frac{\partial \tilde{\tau}_{\tilde{y}\tilde{x}}}{\partial \tilde{y}} + \frac{\partial \tilde{\tau}_{\tilde{z}\tilde{x}}}{\partial \tilde{z}}\right). \tag{2-4}$$

Considering gravity as the only body force, the forces on the fluid element in the $\tilde{x}$, $\tilde{y}$, and $\tilde{z}$ directions are illustrated below:

$$\begin{aligned} d\tilde{F}_{\tilde{x}} &= d\tilde{F}_{B_{\tilde{x}}} + d\tilde{F}_{S_{\tilde{x}}} = \left(\tilde{\rho}\tilde{g}_{\tilde{x}} + \frac{\partial \tilde{\sigma}_{\tilde{x}\tilde{x}}}{\partial \tilde{x}} + \frac{\partial \tilde{\tau}_{\tilde{y}\tilde{x}}}{\partial \tilde{y}} + \frac{\partial \tilde{\tau}_{\tilde{z}\tilde{x}}}{\partial \tilde{z}}\right) d\tilde{x}d\tilde{y}d\tilde{z} \\ d\tilde{F}_{\tilde{y}} &= d\tilde{F}_{B_{\tilde{y}}} + d\tilde{F}_{S_{\tilde{y}}} = \left(\tilde{\rho}\tilde{g}_{\tilde{y}} + \frac{\partial \tilde{\tau}_{\tilde{x}\tilde{y}}}{\partial \tilde{x}} + \frac{\partial \tilde{\sigma}_{\tilde{y}\tilde{y}}}{\partial \tilde{y}} + \frac{\partial \tilde{\tau}_{\tilde{z}\tilde{y}}}{\partial \tilde{z}}\right) d\tilde{x}d\tilde{y}d\tilde{z} \end{aligned} \tag{2-5}$$

$$d\tilde{F}_{\tilde{z}} = d\tilde{F}_{B_{\tilde{z}}} + d\tilde{F}_{S_{\tilde{z}}} = \left(\tilde{\rho}\tilde{g}_{\tilde{z}} + \frac{\partial \tilde{\tau}_{\tilde{x}\tilde{z}}}{\partial \tilde{x}} + \frac{\partial \tilde{\tau}_{\tilde{y}\tilde{z}}}{\partial \tilde{y}} + \frac{\partial \tilde{\sigma}_{\tilde{z}\tilde{z}}}{\partial \tilde{z}} \right) d\tilde{x}d\tilde{y}d\tilde{z}.$$

Replacing the force components from Equation (2-5) for the force components into the $\tilde{x}$, y, and z components of (2-3) yields the differential equations of motion.

$$\begin{aligned}
\tilde{\rho}\tilde{g}_{\tilde{x}} + \frac{\partial \tilde{\sigma}_{\tilde{x}\tilde{x}}}{\partial \tilde{x}} + \frac{\partial \tilde{\tau}_{y\tilde{x}}}{\partial \tilde{y}} + \frac{\partial \tilde{\tau}_{\tilde{z}\tilde{x}}}{\partial \tilde{z}} &= \tilde{\rho}\left(\frac{\partial \tilde{u}}{\partial \tilde{t}} + \tilde{u}\frac{\partial \tilde{u}}{\partial \tilde{x}} + \tilde{v}\frac{\partial \tilde{u}}{\partial \tilde{y}} + \tilde{w}\frac{\partial \tilde{u}}{\partial \tilde{z}}\right) \\
\tilde{\rho}\tilde{g}_{\tilde{y}} + \frac{\partial \tilde{\tau}_{\tilde{x}y}}{\partial \tilde{x}} + \frac{\partial \tilde{\sigma}_{\tilde{y}\tilde{y}}}{\partial \tilde{y}} + \frac{\partial \tilde{\tau}_{\tilde{z}\tilde{y}}}{\partial \tilde{z}} &= \tilde{\rho}\left(\frac{\partial \tilde{v}}{\partial \tilde{t}} + \tilde{u}\frac{\partial \tilde{v}}{\partial \tilde{x}} + \tilde{v}\frac{\partial \tilde{v}}{\partial \tilde{y}} + \tilde{w}\frac{\partial \tilde{v}}{\partial \tilde{z}}\right) \\
\tilde{\rho}\tilde{g}_{\tilde{z}} + \frac{\partial \tilde{\tau}_{\tilde{x}z}}{\partial \tilde{x}} + \frac{\partial \tilde{\tau}_{\tilde{y}z}}{\partial \tilde{y}} + \frac{\partial \tilde{\sigma}_{\tilde{z}\tilde{z}}}{\partial \tilde{z}} &= \tilde{\rho}\left(\frac{\partial \tilde{w}}{\partial \tilde{t}} + \tilde{u}\frac{\partial \tilde{w}}{\partial \tilde{x}} + \tilde{v}\frac{\partial \tilde{w}}{\partial \tilde{y}} + \tilde{w}\frac{\partial \tilde{w}}{\partial \tilde{z}}\right).
\end{aligned} \tag{2-6}$$

So, the Navier-Stokes equation in coordinate free form can be written as follows [20]:

$$\tilde{\rho}\frac{D\tilde{V}}{D\tilde{t}} = \nabla\tilde{S} + \tilde{b} \tag{2-7}$$

where $\tilde{S} = -\tilde{p}I + \tilde{T}$ represents the stress tensor, $\tilde{p}$ denotes the pressure, I stands for the identity tensor, $\tilde{T}$ signifies the viscous stress tensor and $\tilde{b}$ is body forces such as weight. Writing the viscous stress tensor in cylindrical coordinates, the components are:

$$\begin{aligned}
\tilde{\tau}_{\tilde{r}\tilde{r}} &= \tilde{\mu}\left(2\frac{\partial \tilde{u}}{\partial \tilde{r}} - \frac{2}{3}(\nabla.\tilde{V})\right) \\
\tilde{\tau}_{\tilde{\theta}\tilde{\theta}} &= \tilde{\mu}\left((\frac{1}{\tilde{r}}\frac{\partial \tilde{v}}{\partial \tilde{\theta}} + \frac{\tilde{v}}{\tilde{r}}) - \frac{2}{3}(\nabla.\tilde{V})\right) \\
\tilde{\tau}_{\tilde{z}\tilde{z}} &= \tilde{\mu}\left(2\frac{\partial \tilde{w}}{\partial \tilde{z}} - \frac{2}{3}(\nabla.\tilde{V})\right) \\
\tilde{\tau}_{\tilde{\theta}\tilde{r}} &= \tilde{\tau}_{\tilde{r}\tilde{\theta}} = \tilde{\mu}\left(\frac{\partial}{\partial \tilde{r}}(\left(\frac{\tilde{v}}{r}\right)) + \frac{1}{\tilde{r}}\frac{\partial \tilde{u}}{\partial \tilde{\theta}}\right) \\
\tilde{\tau}_{\tilde{\theta}\tilde{z}} &= \tilde{\tau}_{\tilde{z}\tilde{\theta}} = \tilde{\mu}\left(\frac{\partial \tilde{v}}{\partial \tilde{z}} + \frac{1}{\tilde{r}}\frac{\partial \tilde{u}}{\partial \tilde{\theta}}\right) \\
\tilde{\tau}_{\tilde{z}\tilde{r}} &= \tilde{\tau}_{\tilde{r}\tilde{z}} = \tilde{\mu}\left(\frac{\partial \tilde{w}}{\partial \tilde{r}} + \frac{\partial \tilde{u}}{\partial \tilde{z}}\right)
\end{aligned} \tag{2-8}$$

To calculate the flow in a vertical cylinder, the Navier-Stokes equation in cylindrical coordinates is applied. The Navier-Stokes equation in cylindrical coordinates for an incompressible fluid with constant viscosity and density is given by [20]:

$$\begin{aligned}
&\tilde{\rho}\left(\frac{\partial \tilde{u}}{\partial \tilde{t}} + \tilde{u}\frac{\partial \tilde{u}}{\partial \tilde{r}} + \frac{\tilde{v}}{\tilde{r}}\frac{\partial \tilde{u}}{\partial \tilde{\theta}} - \frac{\tilde{v}^2}{\tilde{r}} + \tilde{w}\frac{\partial \tilde{u}}{\partial \tilde{z}}\right) \\
&\qquad = \tilde{\rho}\tilde{g}_{\tilde{r}} - \frac{\partial \tilde{p}}{\partial \tilde{r}} + \tilde{\mu}\left\{\frac{\partial}{\partial \tilde{r}}\left(\frac{1}{\tilde{r}}\frac{\partial}{\partial \tilde{r}}[\tilde{r}\tilde{u}]\right) + \frac{1}{\tilde{r}^2}\frac{\partial^2 \tilde{u}}{\partial \tilde{\theta}^2} - \frac{2}{\tilde{r}^2}\frac{\partial \tilde{v}}{\partial \tilde{\theta}} + \frac{\partial^2 \tilde{u}}{\partial \tilde{z}^2}\right\}
\end{aligned} \tag{2-9}$$

$$\tilde{\rho}\left(\frac{\partial\tilde{v}}{\partial\tilde{t}}+\tilde{u}\frac{\partial\tilde{v}}{\partial\tilde{r}}+\frac{\tilde{v}}{\tilde{r}}\frac{\partial\tilde{v}}{\partial\tilde{\theta}}+\frac{\tilde{u}\tilde{v}}{\tilde{r}}+\tilde{w}\frac{\partial\tilde{v}}{\partial\tilde{z}}\right)$$
$$=\tilde{\rho}\tilde{g}_{\tilde{\theta}}-\frac{1}{\tilde{r}}\frac{\partial\tilde{p}}{\partial\tilde{\theta}}+\tilde{\mu}\left\{\frac{\partial}{\partial\tilde{r}}\left(\frac{1}{\tilde{r}}\frac{\partial}{\partial\tilde{r}}[\tilde{r}\tilde{v}]\right)+\frac{1}{\tilde{r}^2}\frac{\partial^2\tilde{v}}{\partial\tilde{\theta}^2}+\frac{2}{\tilde{r}^2}\frac{\partial\tilde{u}}{\partial\tilde{\theta}}+\frac{\partial^2\tilde{v}}{\partial\tilde{z}^2}\right\}$$
$$\tilde{\rho}\left(\frac{\partial\tilde{w}}{\partial\tilde{t}}+\tilde{u}\frac{\partial\tilde{w}}{\partial\tilde{r}}+\frac{\tilde{v}}{\tilde{r}}\frac{\partial\tilde{w}}{\partial\tilde{\theta}}+\tilde{w}\frac{\partial\tilde{w}}{\partial\tilde{z}}\right)=\tilde{\rho}\tilde{g}_{\tilde{z}}-\frac{\partial\tilde{p}}{\partial\tilde{z}}+\tilde{\mu}\left\{\frac{1}{\tilde{r}}\frac{\partial}{\partial\tilde{r}}\left(\tilde{r}\frac{\partial\tilde{w}}{\partial\tilde{r}}\right)+\frac{1}{\tilde{r}^2}\frac{\partial^2\tilde{w}}{\partial\tilde{\theta}^2}+\frac{\partial^2\tilde{w}}{\partial\tilde{z}^2}\right\}.$$

The Navier-Stokes equations, coupled with the continuity equation, form a set of four coupled equations that describe the flow of fluids. These equations, involving velocity fields and pressure, are fundamental for understanding a wide range of fluid flow.

In the presence of axial symmetry and under steady-state conditions, the derivatives with respect to the azimuthal angle (θ) and time (t) will be zero. Considering the gravity in z-direction in a vertical cylinder, gravity forces act only in this direction. Consequently, the continuity equation and Navier-Stokes equations can be simplified as following:

Continuity equation:

$$\frac{1}{\tilde{r}}\frac{\partial(\tilde{r}\tilde{u})}{\partial\tilde{r}}+\frac{\partial\tilde{w}}{\partial\tilde{z}}=0 \tag{2-10}$$

Navier-Stokes equations:

$$\tilde{\rho}\left(\tilde{u}\frac{\partial\tilde{u}}{\partial\tilde{r}}-\frac{\tilde{v}^2}{\tilde{r}}+\tilde{w}\frac{\partial\tilde{u}}{\partial\tilde{z}}\right)=-\frac{\partial\tilde{p}}{\partial\tilde{r}}+\tilde{\mu}\left\{\frac{\partial}{\partial\tilde{r}}\left(\frac{1}{\tilde{r}}\frac{\partial}{\partial\tilde{r}}[\tilde{r}\tilde{u}]\right)+\frac{\partial^2\tilde{u}}{\partial\tilde{z}^2}\right\}$$
$$\tilde{\rho}\left(\tilde{u}\frac{\partial\tilde{v}}{\partial\tilde{r}}+\frac{\tilde{u}\tilde{v}}{\tilde{r}}+\tilde{w}\frac{\partial\tilde{v}}{\partial\tilde{z}}\right)=\tilde{\mu}\left\{\frac{\partial}{\partial\tilde{r}}\left(\frac{1}{\tilde{r}}\frac{\partial}{\partial\tilde{r}}[\tilde{r}\tilde{v}]\right)+\frac{\partial^2\tilde{v}}{\partial\tilde{z}^2}\right\} \tag{2-11}$$
$$\tilde{\rho}\left(\tilde{u}\frac{\partial\tilde{w}}{\partial\tilde{r}}+\tilde{w}\frac{\partial\tilde{w}}{\partial\tilde{z}}\right)=\tilde{\rho}\tilde{g}_{\tilde{z}}-\frac{\partial\tilde{p}}{\partial\tilde{z}}+\tilde{\mu}\left\{\frac{1}{\tilde{r}}\frac{\partial}{\partial\tilde{r}}\left(\tilde{r}\frac{\partial\tilde{w}}{\partial\tilde{r}}\right)+\frac{\partial^2\tilde{w}}{\partial\tilde{z}^2}\right\}.$$

To solve fluid flow problem using these equations, it's important to carefully consider the appropriate boundary conditions. These conditions are crucial constraints for solving the mentioned differential equations. The specified boundary conditions for simulation of a vertical cylinder are wall and bottom cylinder which due to the non-slip condition, all velocity terms are zero, lid boundary at the top of the cylinder, both radial and axial velocity terms are zero, while the tangential velocity aligns with that of the lid and the interface between immiscible fluids which will be discusses in detail in the following section.

2.3 Interface Boundary Conditions

The interface boundary conditions define the behaviour of the interface in simulation, capturing both the kinematic aspects of fluid motion and the mechanical equilibrium conditions at the interface.

2.3.1 Kinematics Boundary Conditions

These conditions describe the motion of the interface. In this case, the zero normal velocity condition reflects the immiscibility of the fluids and ensures that there is no velocity component normal to the interface. Additionally, the consistent tangential velocity terms ensure that there is no relative motion between the fluids and the boundary, typically enforced by the no-slip boundary condition.

2.3.2 The Dynamic Boundary Conditions in Tangential Direction

These boundary conditions ensure the continuity of tangential shear stress between the two fluids. The shear stress is calculated as follows:
The surface at the interface can be characterized by the following equation:

$$\vec{\tilde{x}}(\tilde{r},\tilde{\theta}) = \tilde{r}\vec{e}_r + \tilde{h}(\tilde{r},\tilde{\theta})\vec{e}_z. \tag{2-12}$$

By considering the problem axially symmetric and removal of the theta, the equation yields:

$$\vec{\tilde{x}}(\tilde{r}) = \tilde{r}\vec{e}_r + \tilde{h}(\tilde{r})\vec{e}_z. \tag{2-13}$$

The tangential vector in r-direction is defined as the derivative $\vec{x} = \vec{x}(r,\theta)$ with respect to the arc-length in that direction:

$$\vec{t}_R = \frac{1}{\left\|\frac{\partial\vec{\tilde{x}}}{\partial\tilde{r}}\right\|}\frac{\partial\vec{\tilde{x}}}{\partial r}$$
$$\vec{t}_\theta = \frac{1}{\left\|\frac{\partial\vec{\tilde{x}}}{\partial\tilde{\theta}}\right\|}\frac{\partial\vec{\tilde{x}}}{\partial\theta} \tag{2-14}$$

In the present case, they read as follows:

$$\vec{t}_R = \frac{1}{\sqrt{1+\tilde{h}_r^2}}\left(\vec{e}_r + \tilde{h}_r\vec{e}_z\right)$$

$$\vec{t}_\theta = \frac{1}{\sqrt{1+\frac{1}{r}\tilde{h}_\theta^2}}\left(\vec{e}_\theta + \frac{1}{\tilde{r}}\tilde{h}_\theta\vec{e}_z\right). \tag{2-15}$$

In the axial symmetric problem, where the theta variable is removed, the tangential vector in the azimuthal direction ($\vec{t}_\theta$) and its corresponding derivatives with respect to theta will be removed from consideration. Therefore, only the tangential vector in the radial direction ($\vec{t}_R$) and its derivatives with respect to r will be considered. The normal vector is obtained as the normalized cross-product of the tangential vectors. In the present case, under axial symmetry assumption, the normal vector is calculated as follows:

$$\vec{n} = \frac{1}{\sqrt{1+\tilde{h}_r^2}}\left(\vec{e}_z - \tilde{h}_r\vec{e}_r\right). \tag{2-16}$$

The strain rate tensor describes the local deformation of a material across time and space. In the cylindrical coordinate system, the infinitesimal strain tensor is represented by six components [21], which are shown already in Equation (2-8). Considering axial symmetry, they are represented as follows:

$$\begin{aligned}
\tilde{\dot{\varepsilon}}_{rr} &= 2\tilde{u}_r \\
\tilde{\dot{\varepsilon}}_{\theta\theta} &= \frac{2}{\tilde{r}}(\tilde{u}) \\
\tilde{\dot{\varepsilon}}_{zz} &= 2\tilde{w}_z \\
\tilde{\dot{\varepsilon}}_{\theta r} &= \tilde{\dot{\varepsilon}}_{r\theta} = \left(\tilde{v}_r - \frac{1}{\tilde{r}}\tilde{v}\right) \\
\tilde{\dot{\varepsilon}}_{zr} &= \tilde{\dot{\varepsilon}}_{rz} = (\tilde{w}_r + \tilde{u}_z) \\
\tilde{\dot{\varepsilon}}_{z\theta} &= \tilde{\dot{\varepsilon}}_{\theta z} = \tilde{v}_z.
\end{aligned} \tag{2-17}$$

The following equations represent shear rates derived from strain rate:

Shear rate in the normal direction:

$$\tilde{s}_n = \frac{1}{1+\tilde{h}_r^2}\left(\tilde{h}_r^2\tilde{\dot{\varepsilon}}_{rr} + \tilde{\dot{\varepsilon}}_{zz} - 2\tilde{h}_r\tilde{\dot{\varepsilon}}_{rz}\right). \tag{2-18}$$

Shear rate in r the direction ($\theta = const$):

$$\tilde{s}_r = \frac{1}{(1+\tilde{h}_r^2)}\left((1-\tilde{h}_r^2)\tilde{\dot{\varepsilon}}_{rz} + \tilde{h}_r\tilde{\dot{\varepsilon}}_{zz} - \tilde{h}_r\tilde{\dot{\varepsilon}}_{rr}\right). \tag{2-19}$$

Shear rate in the θ direction ($r = const$):

$$\tilde{s}_\theta = \frac{1}{\sqrt{(1+\tilde{h}_r^2)}}\left(\tilde{\dot{\varepsilon}}_{z\theta} - \tilde{h}_r\tilde{\dot{\varepsilon}}_{r\theta}\right). \tag{2-20}$$

These equations describe the mechanisms of deformation and shear within the fluid medium, particularly under the conditions of axial symmetry. Dynamic boundary conditions in tangential direction can be seen in Equation (2-21):

$$\tilde{\mu}_F\tilde{s}_{F,r} = \tilde{\mu}_G\tilde{s}_{G,r}$$
$$\tilde{\mu}_F\tilde{s}_{F,\theta} = \tilde{\mu}_G\tilde{s}_{G,\theta}. \tag{2-21}$$

These boundary conditions ensure continuity of the tangential shear stress between the two fluids, where μ represents dynamic viscosity and s represents shear rate.

2.3.3 The Dynamic Boundary Conditions in Normal Direction

Considering the stress balance in normal direction. We must take into account the pressure, the viscous normal stresses and interfacial tension then we have dynamic boundary condition in normal direction which can be seen in the following:

$$-\tilde{p}_F + \tilde{\rho}_F\tilde{g}\tilde{h} + \tilde{\mu}\tilde{s}_{F,n} = -\tilde{p}_G + \tilde{\rho}_G\tilde{g}\tilde{h} + \tilde{\sigma}\kappa + \tilde{\mu}_2\tilde{s}_{G,n}. \tag{2-22}$$

With κ is the Gauss-curvature of interface.

2.3.4 Dimensionless Formulation

To simulate the equations of motion in dimensionless coordinates, we'll use the container radius $\tilde{R}$ as the reference length and the circumferential speed of the top lid $\tilde{R}\tilde{\omega}$ as the reference velocity. The pressure will be scaled accordingly by $\left(\tilde{R}\tilde{\omega}\right)^2\tilde{\rho}$. Then we have the dimensionless number as following:

$$p_F = \frac{\tilde{p}_F}{\tilde{\rho}_F\left(\tilde{R}\tilde{\omega}\right)^2}, \qquad p_G = \frac{\tilde{p}_G}{\tilde{\rho}_G\left(\tilde{R}\tilde{\omega}\right)^2} \tag{2-23}$$

$$\mathrm{Fr} = \frac{\tilde{\rho}_F}{\Delta\tilde{\rho}}\frac{\tilde{u}^2}{\tilde{g}\tilde{R}}, \qquad \mathrm{We} = \frac{\tilde{\rho}_F\tilde{u}^2\tilde{R}}{\tilde{\sigma}}, \qquad \mathrm{Re} = \frac{\tilde{\rho}_F\tilde{u}\tilde{R}}{\tilde{\mu}_F}, \qquad \rho = \frac{\tilde{\rho}_G}{\tilde{\rho}_F}, \qquad \mu = \frac{\tilde{\mu}_G}{\tilde{\mu}_F},$$

$$h_G = \frac{\tilde{h}_G}{\tilde{R}}, \qquad h_F = \frac{\tilde{h}_F}{\tilde{R}}, \qquad h = \frac{\tilde{h}}{\tilde{R}}.$$

Alternative dimensionless numbers are:

$$\mathrm{Ek} = \frac{1}{\mathrm{Re}}, \qquad \mathrm{Bo} = \frac{\mathrm{We}}{\mathrm{Fr}}, \qquad \nu = \frac{\tilde{\nu}_G}{\tilde{\nu}_F}. \tag{2-24}$$

When the mentioned axial symmetric steady state Navier-Stokes and continuity equations in cylindrical coordinates are scaled with a defined reference length, they lead to the following dimensionless equations:

Continuity equation:

$$U_r + \frac{1}{r}U + W_z = 0 \tag{2-25}$$

Navier-Stokes equations:

$$\begin{aligned} UU_r + WU_z - \frac{V^2}{r} &= -p_r + \frac{1}{Re}\left(U_{rr} + \frac{U_r}{r} + U_{zz} - \frac{U}{r^2}\right) \\ UW_r + WW_z &= -p_z + \frac{1}{Re}\left(W_{rr} + \frac{W_r}{r} + W_{zz}\right) \\ UV_r + WV_z + \frac{VU}{r} &= \frac{1}{Re}\left(V_{rr} + \frac{V_r}{r} + V_{zz} - \frac{V}{r^2}\right) \end{aligned} \tag{2-26}$$

The dimensionless equation for the dynamic boundary condition in the normal direction is as follows:

$$h = \frac{\tilde{\rho}_F}{\Delta\tilde{\rho}}\frac{\tilde{u}^2}{\tilde{g}\tilde{R}}(p_F - \rho p_G) + \frac{\tilde{\sigma}}{\tilde{R}^2\Delta\tilde{\rho}\tilde{g}} - \frac{\tilde{\mu}_F\tilde{u}}{\tilde{R}^2\Delta\tilde{\rho}\tilde{g}}(s_{F,n} - \mu s_{G,n}),$$

$$h = \mathrm{Fr}(p_F - \rho p_G) + \underbrace{\frac{\mathrm{Fr}}{\mathrm{We}}}_{\frac{1}{\mathrm{Bo}}}\kappa - \frac{\mathrm{Fr}}{\mathrm{Re}}(s_{F,n} - \mu s_{G,n}). \tag{2-27}$$

These equations represent the dynamic boundary conditions in the normal direction. They balance the pressure, gravitational effects, viscous stresses, surface tension, and surface curvature between the two fluids. Where μ denotes dynamic viscosity, σ denotes surface tension, and κ denotes surface curvature.

The Gauss curvature of a surface, particularly an interface between two media, is a fundamental concept in differential geometry. It provides a measure of how the surface bends and curves within its local environment. The Gauss curvature is defined as the trace of the Weingarten mapping, which relates the normal vectors of points on the surface to the normal vectors of the surface's tangent plane[22].

Mathematically, let S be a smooth surface in $\mathbb{R}^3$with a unit normal vector field n. The Weingarten mapping, denoted by L, maps tangent vectors to the surface to tangent vectors on the surface, and it is given by [22]

$$L(v) = -D_V n. \tag{2-28}$$

where D_V denotes the directional derivative along the tangent vector v. The Gauss curvature k at a point on the surface is then defined as the determinant of the Weingarten mapping [22]:

$$k = \det(L). \tag{2-29}$$

Alternatively, the Gauss curvature can be expressed as the product of the principal curvatures at that point. Here the surface curvature κ is calculated as follows:

$$\kappa = -\frac{1}{\sqrt{1+h_r^2}}\left(\frac{h_{rr}}{1+h_r^2}+\frac{1}{r}h_r\right). \tag{2-30}$$

To eliminate pressure from the dynamic boundary condition, it should be differentiated with respect to the radial component χ in computational coordinates (the computational coordinates will be explained in detail in section 3.1), and the equation will be expressed as:

$$h_\chi = \mathrm{Fr}\left(p_{F,\chi} - \rho p_{G,\chi} + \frac{\partial}{\partial\chi}\left(\frac{1}{We}\kappa - \frac{1}{Re}\left(s_{F,n} - \mu s_{G,n}\right)\right)\right) \tag{2-31}$$
$$h_r(0) = h_r(1) = 0.$$

At $z = h(r)$ the pressure term is computed as:

$$p_{F,\chi} = p_{F,r} + h' p_{F,z}. \tag{2-32}$$

Here, $k = \frac{2}{r^2}\int_0^r r' h(r') dr'$ represents the average height of the interface over the circular area with radius *r* around the axis of rotation where:

$$\frac{r}{2}k_r + k = h \tag{2-33}$$

and $k(0) = k(1) = 0$.

In the context of two-dimensional, incompressible fluid dynamics, the introduction of a stream function, denoted as $F(r,z)$, facilitates the fulfillment of the continuity equation:

$$U = \frac{1}{r}\frac{\partial F}{\partial z}$$
$$W = -\frac{1}{r}\frac{\partial F}{\partial r}. \tag{2-34}$$

Substituting into the derived simplified dimensional Navier-Stokes equations yields the following expressions:

$$-\frac{1}{r^3}F_z^2 + \frac{1}{r^2}(F_z F_{rz} - F_r F_{zz}) - \frac{V^2}{r} = -p_r + \frac{1}{\mathrm{Re}}\left(\frac{1}{r}F_{zrr} - \frac{1}{r^2}F_{zr} + \frac{1}{r}F_{zzz}\right)$$
$$-\frac{1}{r^3}F_z F_r - \frac{1}{r^2}(F_z F_{rr} - F_r F_{rz}) = -p_z + \frac{1}{\mathrm{Re}}\left(-\frac{1}{r^3}F_r + \frac{1}{r^2}F_{rr} - \frac{1}{r}F_{rrr} - \frac{1}{r}F_{rzz}\right). \tag{2-35}$$

The vorticity $G(r,z)$, is defined as the curl of the velocity vector field. Eliminating the pressure from the momentum equations yields the vorticity transport equation, which is expressed as:

$$G = U_z - W_r. \tag{2-36}$$

The similarity forms are defined in the following:

$$F = r^2 f$$
$$V = rv \tag{2-37}$$
$$G = rg.$$

After replacing the vorticity function and applying the similarity forms $F = r^2 f, V = rv$ and $G = rg$ into the derived equations, they will look as following:

$$(r(f_z v_r - f_r v_z) + 2f_z v - 2f v_z) = \frac{1}{Re}(v_{rr} + \frac{1}{r}v_r + v_{zz})$$
$$(r(f_z g_r - f_r g_z) + 2g_z f - 2v v_z) = \frac{1}{Re}(g_{rr} + \frac{3}{r}g_r + g_{zz}) \tag{2-38}$$
$$g = \left(g_{rr} + \frac{3}{r}f_r + f_{zz}\right).$$

These equations, which are derived from Navier-Stokes equations, show the relationship between the stream function, vorticity, and tangential velocity.

The equations are valid for $h(r,t) < z < h_G$. However, $-h_F < z < h(r,t)$, v must be replaced by 1.

2.4 Self-Similar Flow Between Infinite Discs

Considering the similarity solution for the flow between two infinitely extended parallel rotating disks, which leads to the independence of the functions f, g, and v with respect to 'r', the following ordinary differential equations (ODE) can be derived:

$$2f_z v - 2f v_z = Ek_w(v_{zz})$$
$$2g_z f - 2v v_z = Ek_w(g_{zz}) \tag{2-39}$$
$$g = f_{zz}.$$

Which satisfy the subsequent boundary conditions:

$$f_z(0) = f(0) = v(0) = f_z(1) = f(1) = 0, \quad v(1) = 1.$$

And the Reynolds number is calculated based on the distance between the disks.

$$Re = \frac{\tilde{\omega}^2 \tilde{h}}{\tilde{\nu}} \tag{2-40}$$

The similarity solutions transform the partial differential equation (PDE) into an ordinary differential equation, simplifying the system. These equations are then solved for both a single fluid and two fluids between the disks.

3 Numerical Methods

In this section, numerical methods for solving partial and ordinary differential equations will be discussed. Firstly, the necessity of introducing new coordinates and how the equations are derived in these coordinates will be explained. Next, it will be shown that to numerically solve the equations, they need to be discretized. For this purpose, the spectral method based on Chebyshev polynomials will be employed. The discretized equations, either in computational or cylinder coordinates, will be implemented in a C program. Subsequently, they will be solved using the NAG library, with boundary conditions applied.

3.1 Computational Coordinates

By rotating two immiscible fluids in a cylinder, the interface between the two fluids is not a flat surface anymore and the shape needs to be calculated and considered in the calculations. To fulfill the previously mentioned boundary condition on the interface, the coordinate system needs to be shifted to comply with the new shape of the interface. Introducing coordinates that align with the interface simplifies the description of interface-related phenomena. This alignment makes the mathematical formulation more intuitive and straightforward, leading to a clearer understanding of the physical processes occurring at the interface. Overall, the introduction of such coordinates significantly enhances the ability to study and analyze the complex dynamics of the interface between immiscible fluids. In the following the computation of the new coordinate system and the calculations of different derivatives are explained.

The new coordinate system is designed to align tangentially and perpendicularly to the interface. This can be done by aligning one coordinate axis with the direction along the interface and making the other axis orthogonal to it. This new coordinate, denoted as (χ, ξ or χ, ζ, for lower or upper fluid respectively), is determined as follows by considering the axis and radius of the cylinder (physical coordinates z, r).

$$\begin{aligned} \chi &= r \\ \zeta &= \frac{z - h(r)}{h_G - h(r)} = 1 - \frac{h_G - z}{h_G - h} \quad \text{for } h(r) < z < h_G \\ \xi &= \frac{z + h_F}{h_F + h(r)} - 1 \text{ for } -h_F < z < h(r). \end{aligned} \tag{3-1}$$

For the velocity field $V(r,z)$, two cases are considered based on the value of z:

$$V(r,z)=\begin{cases}\tilde{V}\left(r,1-\dfrac{h_G-z}{h_G-h(r)}\right), & h(r)<z<h_G,\\ \hat{V}\left(r,\dfrac{z+h_F}{h_F+h(r)}-1\right), & -h_F(r)<z<h(r).\end{cases} \tag{3-2}$$

In the new coordinate system, the first derivatives are calculated as following:

$$\begin{aligned}\frac{\partial V}{\partial r}&=\frac{\partial\xi}{\partial r}\frac{\partial\hat{V}}{\partial\xi}+\frac{\partial\hat{V}}{\partial\chi}\\ \frac{\partial V}{\partial z}&=\frac{\partial\xi}{\partial z}\frac{\partial\hat{V}}{\partial\xi}.\end{aligned} \tag{3-3}$$

For the first and second derivatives, the computations for ζ followed a similar approach as those for ξ. Such as the first derivatives, the second derivatives can be calculated as following:

$$\begin{aligned}\frac{\partial^2 V}{\partial r^2}&=\frac{\partial^2\xi}{\partial r^2}\frac{\partial\hat{V}}{\partial\xi}+\left(\frac{\partial\xi}{\partial r}\right)^2\frac{\partial^2\hat{V}}{\partial\xi^2}+2\frac{\partial\xi}{\partial r}\frac{\partial^2\hat{V}}{\partial\xi\,\partial\chi}+\frac{\partial^2\hat{V}}{\partial\chi^2}\\ \frac{\partial^2 V}{\partial z\,\partial r}&=\frac{\partial^2\xi}{\partial r\,\partial z}\frac{\partial\hat{V}}{\partial\xi}+\frac{\partial\xi}{\partial r}\frac{\partial\xi}{\partial z}\frac{\partial^2\hat{V}}{\partial\xi^2}+\frac{\partial\xi}{\partial z}\frac{\partial^2\hat{V}}{\partial\chi\,\partial\xi}\\ \frac{\partial^2 V}{\partial z^2}&=\left(\frac{\partial\xi}{\partial z}\right)^2\frac{\partial^2\hat{V}}{\partial\xi^2}\end{aligned} \tag{3-4}$$

Derivatives of the coordinate transformation for upper fluid (referred as gas):

$$\begin{aligned}&\zeta_z=\frac{1}{h_G-h(r)},\qquad \zeta_r=+\frac{z-h_G}{\left(h_G-h(r)\right)^2}h'=\zeta\frac{h'}{h_G-h(r)},\\ &\zeta_{zz}=0,\qquad \zeta_{rz}=\frac{h'(r)}{\left(h_G-h(r)\right)^2},\\ &\zeta_{rr}=2\frac{z-h_G}{(h_G-h(r))^3}h'(r)^2+\frac{z-h_G}{(h_G-h(r))^2}h''(r)=2\xi\frac{h'(r)^2}{(h_G(r)-h(r))^2}+\xi\frac{h''(r)}{h_G-h(r)}\end{aligned} \tag{3-5}$$

And for lower fluid (referred to as liquid - Flüssigkeit):

$$\begin{aligned}&\xi_z=\frac{1}{h(r)+h_F},\qquad \xi_r=-\frac{z+h_F}{(h(r)+h_F)^2}h'=-\xi\frac{h'}{h(r)+h_F}\\ &\xi_{zz}=0,\qquad \xi_{rz}=-\frac{h'(r)}{(h(r)+h_F)^2},\\ &\xi_{rr}=2\frac{z+h_F}{(h(r)+h_F)^3}h'(r)^2-\frac{z+h_F}{(h(r)+h_F)^2}h''(r)=2\xi\frac{h'(r)^2}{(h(r)+h_F)^2}-\xi\frac{h''(r)}{h(r)+h_F}.\end{aligned} \tag{3-6}$$

3.2 Spectral Collocation Method

To solve the differential equations systems mentioned so far, numerical methods are utilized, requiring discretization. Spectral methods are employed for discretization and after applying relevant boundary conditions, the discretized equations are solved using the NAG library in C [23].

Spectral collocation methods are popular for solving differential equations. Instead of using local interpolants like finite difference and finite element methods, spectral methods employ a global interpolant (e.g., a polynomial) of high degree. The unknown solution is approximated by this interpolant, and its derivatives are computed using spectral differentiation matrices [2].

The spectral method will be employed to solve the differential equations derived from the Navier-Stokes equations in cylindrical coordinates. This method is an approach for solving partial differential equations, like the Navier-Stokes equations, employing basis functions [24]. These methods offer superior accuracy for problems with smooth solutions, converging exponentially faster than finite difference and finite element methods. However, they come with the drawbacks of full matrices (not sparse), tighter stability restrictions, and less flexibility with irregular domains [2].

The unknown functions in differential equations are approximated by interpolating the function with a polynomial at the Chebyshev-Gauss-Lobatto nodes [2]:

$$x_j := \cos\frac{\pi j}{N}, \quad j = 0,1,\dots,N \text{ where } -1 < x_j < 1. \tag{3-7}$$

The unknown function f is approximated by projecting it onto a polynomial basis using the following expression[2]:

$$P_N(x) = \frac{\sum_{K=0}^{N} \frac{\lambda_k}{x - x_k} f_k}{\frac{\lambda_k}{x - x_k}}. \tag{3-8}$$

The λ_k is determined by [2]:

$$\eta_k = \sum_{\substack{j=0 \\ j \neq k}}^{N} \ln|x - x_k| \,, \qquad \lambda_k = (-1)^k e^{-\eta_k} \tag{3-9}$$

To compute the first-order differentiation matrix:

$$D_{ij} = \frac{1}{x_i - x_j}\frac{\lambda_j}{\lambda_i} \text{ for } i \neq j. \tag{3-10}$$

$$D_{ii} = -\sum_{j=0, j\neq i}^{N} D_{ij},\ i = 0,1,\dots,N.$$

And for higher-order differentiation matrices:

$$D_{ij}{}^{l} = \frac{l}{x_i - x_j}\left(\frac{\lambda_j}{\lambda_i} D_{ii}{}^{l-1} - D_{ij}{}^{l-1}\right) \text{ for } i \neq j.$$
$$D_{ii}{}^{l} = -\sum_{j=0, j\neq i}^{N} D_{ij}{}^{l},\ i = 0,1,\dots,N \tag{3-11}$$

The equation provided is used to determine the approximated first derivative of the function f. A similar formula is utilized for higher-order derivatives:

$$\dot{f}_j = \sum_{i=0}^{N} D_{ij} f_j \tag{3-12}$$

This equation computes the first derivative of $\dot{f}_j$, where f_j represents the derivative, and D_{ij} denotes the differentiation matrix. Continuing, the application of the spectral method for solving the system of partial equations can be exemplified. Considering axial symmetry in the cylindrical coordinate system the theta dimension can be excluded. The unknown function f, which serves as an unknown variable in a partial equation, has two independent variables r and z within the domain $0 < r < 1$ and $0 < z < h$. For computational purposes, nodes are required in both the radial (r) and axial (z) directions. Specifically, nodes are established for the radial direction and axial directions. After determining these nodes in each dimension, they are mapped onto their respective domains. The mapping process involves determining r_j for the radial direction and z_j for the axial directions. The mapping utilizes the cosine function to transform x_j into the desired domain. To derive r_j, x_j is determined by:

$$x_j \coloneqq \cos\frac{\pi j}{N_r},\ j = 0,1,\dots,N_r \text{ where } -1 < x_j < 1. \tag{3-13}$$

Here, N_r signifies the count of nodes in the radial dimension. The mapping of x_j to the domain $[0,1]$ yields r_j. To find z_j, x_j is defined as:

$$x_j \coloneqq \cos\frac{\pi j}{N_z},\ j = 0,1,\dots,N_z \text{ where } -1 < x_j < 1. \tag{3-14}$$

Here, N_z denotes the count of nodes in the z direction and the mapping of x_j to the domain $[0,h]$ yields z_j. The total nodes are $N_r \times N_z$, the partial derivatives for each nodes should be determined, so The differentiation matrices for each variable r and z will be calculated analogously to Equations (3-10) and (3-11). Then, the partial derivatives can be computed following Equation (3-12). By substituting the unknown function and its derivatives into the system of partial equations at each node, excluding those located on the boundaries, and

applying boundary condition equations for nodes situated on the boundaries, the equations system is obtained to solve. The values of the function v, f, g at the nodes (r_i, z_j) where $r_i \in [0,1]$ and $z_j \in [0, \mathrm{h}]$ are used a as unknowns. Thus, in case of a single fluid in a container, we have $N_{eq} = 3\,(Nr+1) \times (Nz+1)$ unknowns and the same number of equations. In case of two fluids for Fr=0 (fixed surface) we have $N_{eq} = (Nr+1) \times (3Nz1 + 3Nz2 + 6)$ unknowns ($Nz1$ and $Nz1$ represent the number of nodes in the z-direction for each upper and lower fluid, respectively). Finally in case of a free interface, we must consider the deviation $h(r)$ of the interface form the equilibrium position at the nodes r_i as additional unknowns then we have $N_{eq} = (Nr+1) \times (3Nz1 + 3Nz2 + 8)$ numbers of unknowns.

3.3 Testing the Numerical Method

Here, the focus is on testing the described numerical method. The NAG (Numerical Algorithms Group) library is a collection of mathematical and statistical algorithms, designed to be used by developers and researchers in various fields of science, engineering, and finance. It is a comprehensive library that provides a wide range of numerical routines for solving various mathematical problems, such as linear algebra, optimization, numerical integration, and differential equations. In this study the NAG library will be used for solving the discretized equations. In continue a brief overview of the code for solving differential equations using the Chebyshev spectral methods and the `c05qbc` solver is provided. It highlights the key components and their roles in the numerical solution process:

a) Solver c05qbc:

The nag_zero_nonlin_eqns_easy function (c05qbc) offers a straightforward solution for solving a system of nonlinear equations, utilizing a modified version of the Powell hybrid method [25]. The system of equations is formulated as follows:

$$f_i(x_1, x_2, \dots, x_n) = 0 \quad i = 1,2, \dots, n. \tag{3-15}$$

This solver effectively handles stiff differential equations outlined in the diffgl function (explained in the following - 3). It employs advanced techniques to efficiently solve these equations. The solver iteratively refines the solution until reaching a specified tolerance level, ensuring high accuracy in the final solution.

b) setmatrices Function

The setmatrices function implements differentiation matrices using Chebyshev-Gauss-Lobatto collocation. Here is a breakdown of the code of the function in mathematical terms for a single fluid in similarity form:

a) Initialization:

- Initialize necessary variables and arrays.
- Set up the Chebyshev-Gauss-Lobatto collocation points s_i using the formula:

$$s_i = -cos\,(\frac{i\pi}{N}) \tag{3-16}$$

where N is the number of points and $-1 < s_i < 1$. Consequently, the s_i values will be mapped to the interval $[0, z]$.

b) Calculation of Weighting Functions:

- Calculate the weighting functions $\lambda_i$using the formula from [2]:

$$\lambda_i = (-1)^i exp\,(-\sum_{j=0, j\neq i}^{N} \log \mid s_i - s_j \mid) \tag{3-17}$$

c) First Derivative Matrix D1:

- Calculate the first derivative matrix entries $D1(i,j)$ using the formula:

$$D1_{ij} = \frac{1}{s_i - s_j}\frac{\lambda_j}{\lambda_i} \text{ for } i \neq j. \tag{3-18}$$

- Use the negative sum trick to calculate the diagonal entries:

$$D1_{ii} = -\sum_{j=0, j\neq i}^{N} D1_{ij} \tag{3-19}$$

d) Second Derivative Matrix $D2$:

- Calculate the second derivative matrix entries $D2(i,j)$ using the formula:

$$D2_{ij} = \frac{2}{s_i - s_j}(\frac{\lambda_j}{\lambda_i} D1_{ii} - D1_{ij}) \text{ for } i \neq j. \tag{3-20}$$

- Use the negative sum trick to calculate the diagonal entries:

$$D2_{ii} = -\sum_{j=0,j\neq i}^{N} D2_{ij} \tag{3-21}$$

3. diffgl Function

The diffgl function in the code serves as the user-defined equivalent of the fcn function required by the NAG library's c05qbc solver. The fcn function must be implemented by the user to enable the solution of nonlinear equations using c05qbc. Here's the definition of fcn:

```
void fcn(Integer n, const double x[], double fvec[], Nag_Comm * comm, Integer *iflag)
```

Figure 3: Definition of fcn

and Its arguments include:

- n (Integer): Number of equations.
- x: Components of the point for function evaluation (not to be confused with 'x' representing Chebyshev-Gauss-Lobatto nodes, as depicted in the original documentation of the NAG library; here, it is presented in its original form).
- fvec: The function values $f_i(x_1, x_2, \dots, x_n)$.
- comm: Pointer to communication structure.
- iflag: Acts as a status flag, potentially used to terminate execution.

In the diffglg function, the array y represents the unknown variables in our system of equations, akin to the array x in the fcn function. The f array stores the corresponding function values. So, the diffglg for a single fluid in similarity form works as follows:

a) Calculation of First and Second Derivatives:

For each dependent variable y_j - which in this similarity solution can be represented by the f, g or v function from equation (3-22), calculate its first derivative and second derivative $\frac{d^2y_j}{dz^2}$ with respect to the independent variable z. In this similarity solution, we only have z as the independent variable.

$$\frac{dy_j}{dz} = \sum_{k=0}^{N} D1_{jk} y_k$$

$$\frac{d^2y_j}{dz^2} = \sum_{k=0}^{N} D2_{jk} y_k \tag{3-23}$$

b) Express the array f as the system of differential equations for solving f, v, and g from equation (2-39).

c) Implementing boundary conditions for the similarity form of equations system, considering only one fluid in the container.

For validation, an analogous code was employed to simulate the flow of two immiscible fluids in a cylindrical container with a free interface. Surface displacements at the interface across various mesh sizes were compared using the root mean square (RMS) method to understand any differences. Results indicated that the mesh size used to solve the equations ($Nr = 25$, $Nz = 60$) achieved an acceptable level of accuracy, as evidenced by close overlap in surface displacements across different mesh sizes.

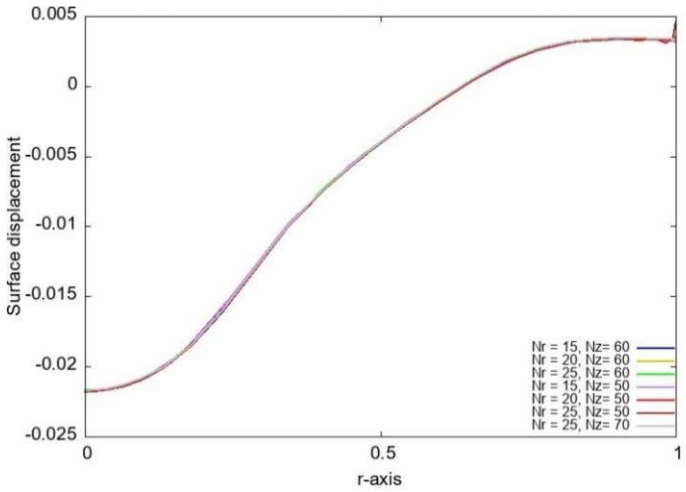

Figure 4: Surface displacement of the Interface Between Two Immiscible Fluids at Reynolds = 1000, with a Density Ratio of 2 and Dynamic Viscosity Ratio of 1. Utilizing Different Mesh Grids.

Additionally, the root mean square (RMS) method was employed to quantify the discrepancy between different mesh sizes, ensuring consistent conditions and precise error assessment.

$$RMS = \sqrt{\frac{1}{n}\sum_{i=1}^{n}(y_{A,i} - y_{B,i})^2} \tag{3-24}$$

where $y_{A,i}$ and $y_{B,i}$ are the values of data sets A and B , respectively. Due to the different number of grid points, interpolation is necessary to ensure an equal number of data points for both data sets. The table below summarizes the Root Mean Square (RMS) values for each pair of data sets, facilitating a comprehensive understanding of the differences between various mesh sizes.

Table 1: Root Mean Square (RMS) Values Between Each Pair of Data Sets

	Nr = 15, Nz = 60	Nr = 20, Nz = 60	Nr = 25, Nz = 60	Nr = 15, Nz = 50	Nr = 20, Nz = 50	Nr = 25, Nz = 50	Nr = 25, Nz = 70
Nr = 15, Nz = 60	0	1.3 e-04	1.3 e-04	1.7 e-05	1.4 e-04	3.0 e-04	1.3 e-04
Nr = 20, Nz = 60	1.3 e-04	0	7.9 e-05	1.4 e-04	1.3 e-05	2.3 e-04	6.3 e-05
Nr = 25, Nz = 60	1.3 e-04	7.9 e-05	0	1.3 e-04	8.8 e-05	2.7 e-04	2.6 e-05
Nr = 15, Nz = 50	1.7 e-05	1.4 e-04	1.3 e-04	0	1.3 e-04	3.7 e-04	1.4 e-04
Nr = 20, Nz = 50	1.4 e-04	1.3 e-05	8.8 e-05	1.3 e-04	0	2.3 e-04	7.0 e-05
Nr = 25, Nz = 50	3.0 e-04	2.3 e-04	2.7 e-04	3.7 e-04	2.3 e-04	0	2.5 e-04
Nr = 25, Nz = 70	1.3 e-04	6.3 e-05	2.6 e-05	1.4 e-04	7.0 e-05	2.5 e-04	0

4 Results

In this section the results of similarity and non-similarity solutions for one and two fluids, considering different relative properties are presented and discussed.

4.1 The Flow of One Fluid Between Two Infinite Rotating Discs

In this section, the results of a similarity solution are presented, initially focusing on a single fluid, and then extending to two fluids, each analyzed at various Reynolds numbers. The numerical solution involves the utilization of eighty cells positioned between the two disks. In the similarity form, all functions are solved in a non-dimensional context, where they are characterized by a single parameter, $'z'$. Diagrams are plotted for $'z'$ ranging from -1 to 1, with varying functions. The equations are solved for different Reynolds numbers, each represented by a distinct color in the diagrams.

In Figure 5a Tangential Velocity concerning $'z'$ for different Reynolds numbers is shown. As observed in the diagram, due to the non-slip boundary condition, the tangential velocity on the lid (at $z = 1$) equals one, while at the bottom $(z = 0)$, it is zero. for most $'z'$ values, the tangential velocity maintains a constant value $\omega \approx 0.4$; however, deviations from this constant value occur near the bottom and lid. With an increase in Reynolds number, the tangential velocity tends to remain more constant across various $'z'$ values.

The subsequent diagram (Figure 5b) illustrates the Radial Velocity between two disks. Once again, due to the non-slip boundary condition, the radial velocity at both the lid and the bottom remains zero for all Reynolds numbers. For most $'z'$ values, the radial velocity stays at zero, except near the top and bottom where it's not zero. Also, as the Reynolds number increases, the difference from zero radial velocity becomes smaller because of less viscosity at higher Reynolds numbers.

The final diagram (Figure 5c) in the results of the Similarity solution illustrates the Axial Velocity. Like the previous cases, due to the no-slip boundary condition, the axial velocity is zero at both the bottom and the top. As one moves away from the bottom and top, the axial velocity reaches a constant value. This constant value decreases as the Reynolds number increases.

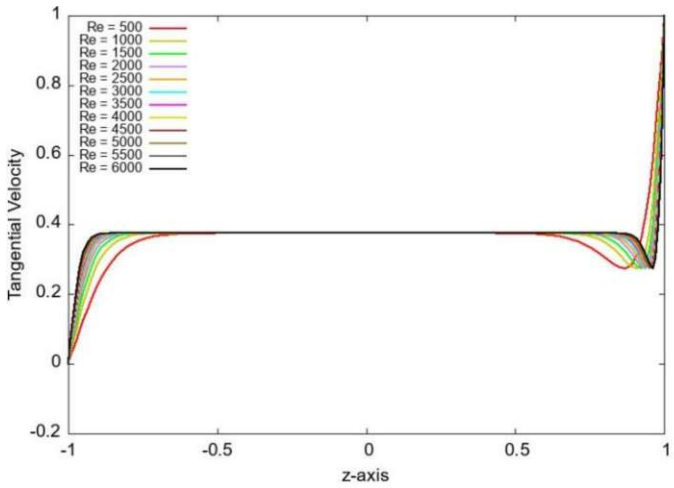

(a)

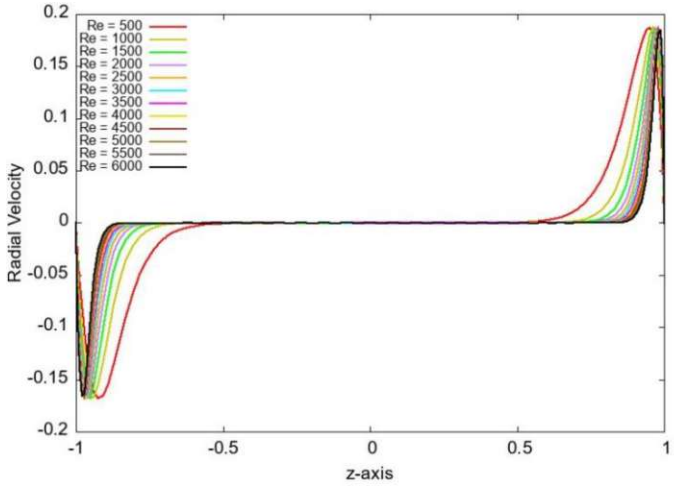

(b)

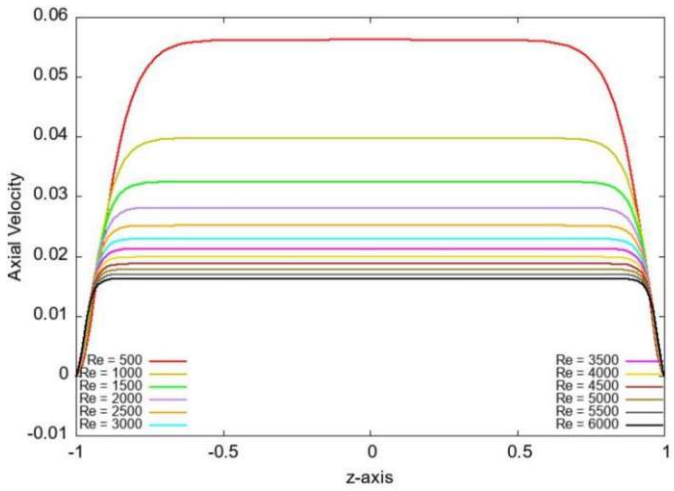

(c)

Figure 5:Velocity Components in Single Fluid Similarity Solution with 80-Node Mesh across Various Reynolds Numbers. (a) Tangential Velocity (b) Radial Velocity (c) Axial Velocity

4.1.1 Comparison with Results from Literature

In this section, the results of the radial velocity will be compared with those reported in the paper [26]. A direct one-to-one comparison is not feasible due to differences in the boundary conditions of our solution compared to those in the paper. The paper discusses a setup where both the bottom and top disks are rotated with relative angular velocity. However, in this study, only the top disk is rotated. Therefore, adjustments and considerations will be made to account for these differences during the comparison process.

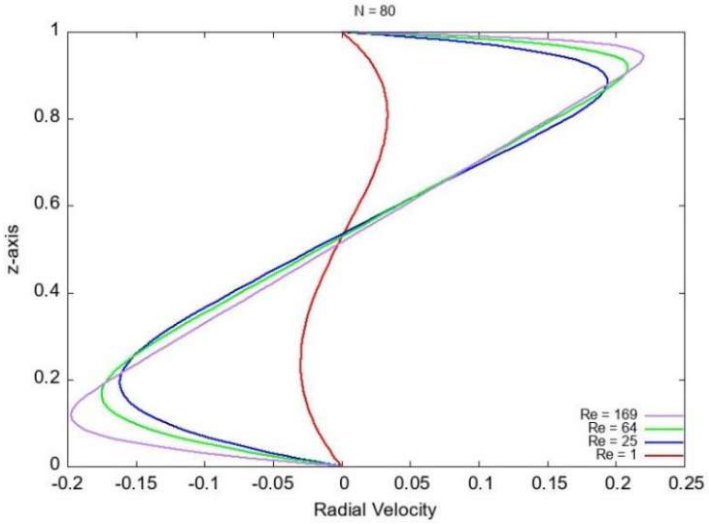

Figure 6: Radial Velocity Profile Obtained from this study

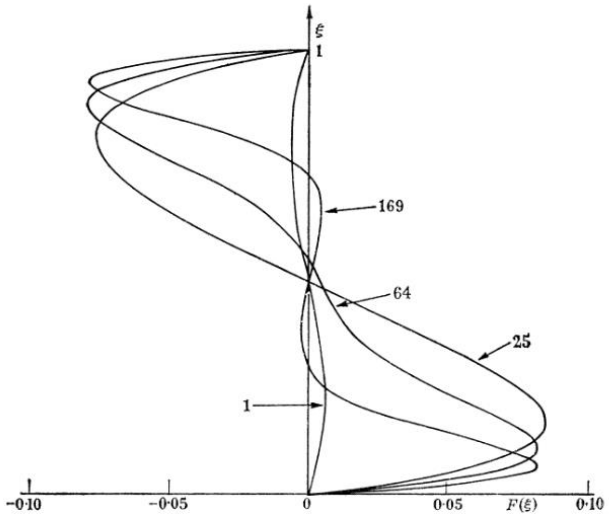

Figure 7: Radial Velocity Profile Reported in Reference Paper[26]

By comparing the results in the paper and this study in Figure 6 and Figure 7, it can be observed that the radial velocity at the top is zero. By comparing the results presented in the paper with those of this study, as depicted in Figures 6 and 7, it becomes apparent that the radial velocity at the top is zero. Subsequently, it increases quadratically in absolute terms, then decreases until it approaches zero once more, near the midpoint of the disks. Beyond this point, it demonstrates a similar mirrored behavior; the velocity increases quadratically in the opposite direction, then decreases again until reaching zero velocity at the bottom.

4.2 The Flow of Two Immiscible Fluid Between Two Infinite Rotating Discs

The following diagrams illustrate the results of similarity solutions for two fluids, considering three different density ratios (2, 25, and 50) and two distinct viscosity ratios (1 and 0.5), across various Reynolds numbers. To avoid overcrowding the diagrams, only two cases are showcased here, with the remaining cases available for reference in the appendix. The initial results (Figure 8(a and Figure 9a) showcase the tangential velocity obtained from a similarity solution applied to two different fluids. The tangential velocity in the upper fluid mirrors the behavior observed in a scenario with only one fluid, reaching a stable value at high Reynolds numbers.

As the density ratio (lower fluid density to upper fluid density) increases from 2 to 50, the constant value for tangential velocity in the upper fluid is observed at higher Reynolds numbers. For instance, with a density ratio of 2(Figure 8a), its constant value is achieved at Reynolds 500. Conversely, with a density ratio of 50(Figure 9a), a higher Reynolds number is necessary to reach its constant value. However, as the density ratio continues to climb, this constant value decreases. As mentioned earlier, the constant value for tangential velocity in a single fluid is approximately 0.4. With an increasing density ratio in two fluids, the value in the upper fluid decreases, converging to approximately 0.4. To clarify, at a density ratio of 2, the constant value for tangential velocity in the upper fluid is roughly 0.65, while with a density ratio of 50, it decreases to around 0.45. Indeed, an increasing density ratio signifies that the lower fluid becomes heavier. Consequently, the flow in the upper fluid more closely resembles the flow in a scenario with only one fluid situated between disks.

In a stable scenario, the impact of viscosity is reduced. Therefore, as the Reynolds number increases, the influence of viscosity becomes less pronounced.

In Figures Figure 8b and Figure 9b, like the tangential velocity, achieving a stable configuration for radial velocity requires higher Reynolds numbers as the density ratio increases. For instance, stability is reached at Reynolds number 5000 with a density ratio of 2. However, at a density ratio of 50, stability is not achieved at Reynolds number 5000; a higher Reynolds number is required. As the density ratio increases, the radial velocity in the lower fluid decreases, indicating that it becomes heavier than the upper fluid. Simultaneously, reducing the viscosity ratio results in an increase in the radial velocity in the lower fluid.

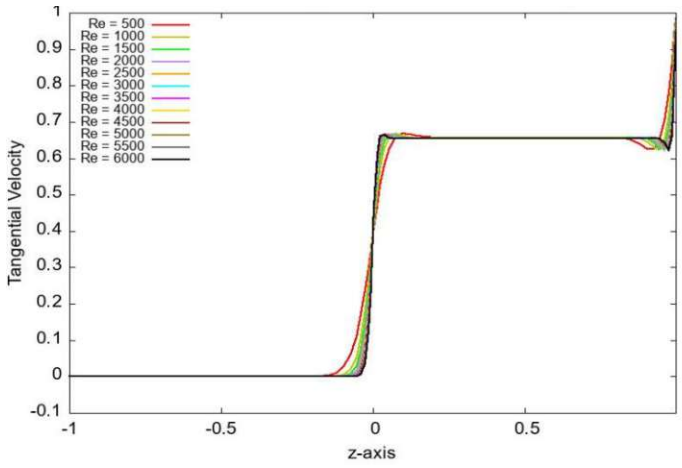

(a)

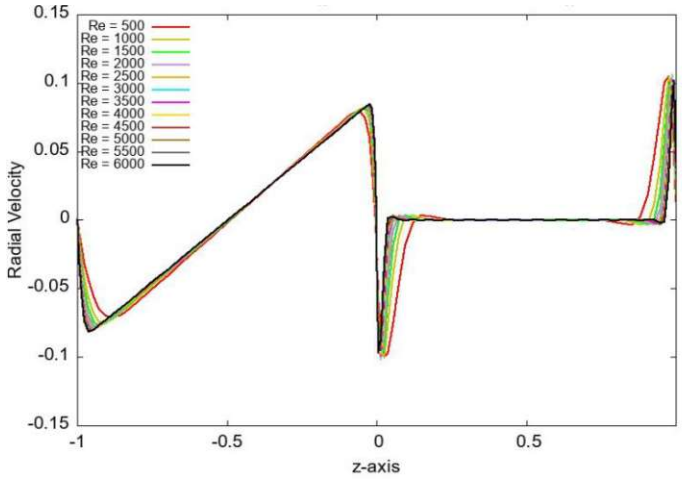

(b)

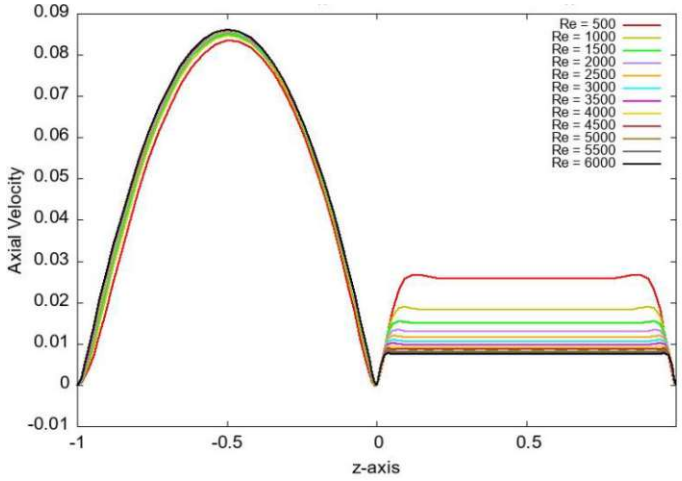

(c)

Figure 8 : Velocity components in Two Immiscible Fluids Similarity Solution with 80-Node Mesh Across Various Reynolds Numbers, Density Ratio 2, and Viscosity Ratio 1.(a) Tangential Velocity (b) Radial velocity (c) Axial velocity

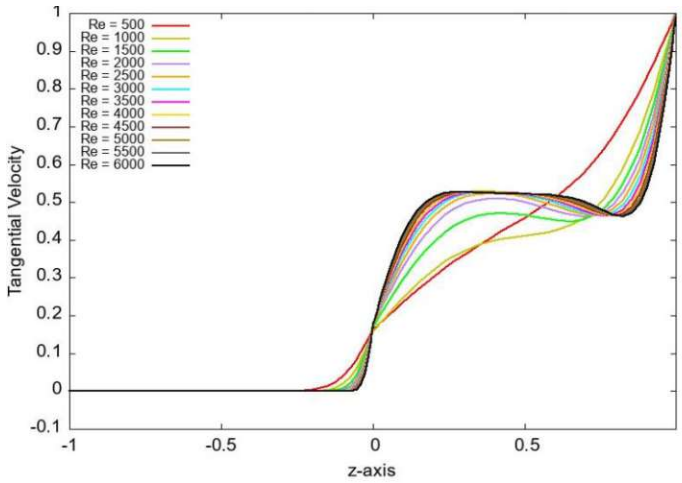

(a)

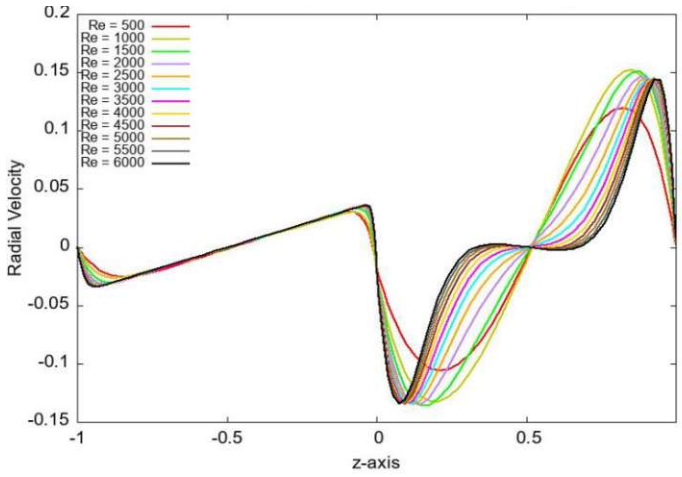

(b)

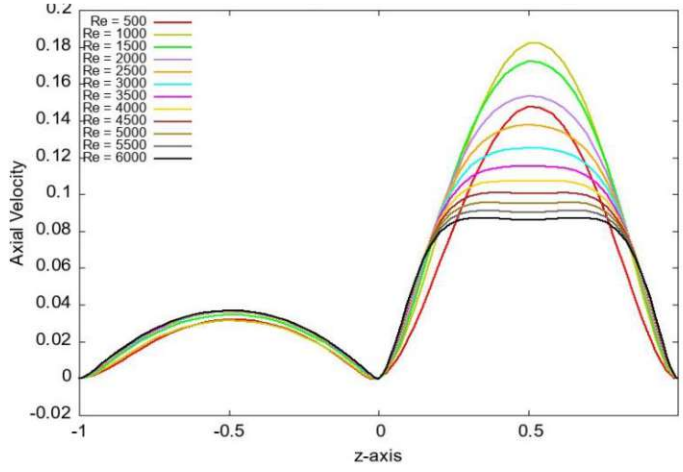

(c)

Figure 9: Velocity components in Two Immiscible Fluids Similarity Solution with 80-Node Mesh Across Various Reynolds Numbers, Density Ratio 50, and Viscosity Ratio 0.5. (a) Tangential Velocity (b) Radial velocity (c) Axial velocity

In Figures, Figure 8c and Figure 9c, achieving stability in axial velocity involves adjusting Reynolds numbers and density ratios. Higher Reynolds numbers are necessary for stability as the density ratio increases, analogous to the behavior observed in tangential and radial velocity. For example, stability may be attained at Reynolds number 5000 when the density ratio is 2, but not when the density ratio is 50, requiring a higher Reynolds number. Decreasing the density ratio leads to an increase in axial velocity in the lower fluid. In stable configurations, reducing the viscosity ratio generally results in higher axial velocity. However, at higher Reynolds numbers, the influence of viscosity on axial velocity diminishes. In specific cases, such as Reynolds number 5000 with a density ratio of 50, where stability is not achieved, the conventional relationship between viscosity ratio and axial velocity may not hold as expected.

4.3 The Flow of Fluid in a Cylindrical Container

This section is dedicated to solving equations in the non-similarity form, with a specific focus on a single fluid within a vertical cylinder. The functions in the non-similarity form are characterized by both parameters 'r' and 'z.' Like the similarity form, all functions are resolved in a non-dimensional context. The equations are solved for Reynolds numbers ranging from 500 to 6000. In this section, like the previous one, only two cases are presented to prevent overcrowding the diagrams. The remaining cases can be referred to in the appendix. Additionally, we extend our analysis to include Reynolds numbers of 50, 300, 750 and 2000, providing a comprehensive comparison through contour plots, in line with existing literature. Subsequent sections will further explore the resolution of these equations for two non-mixing fluids within a vertical cylinder.

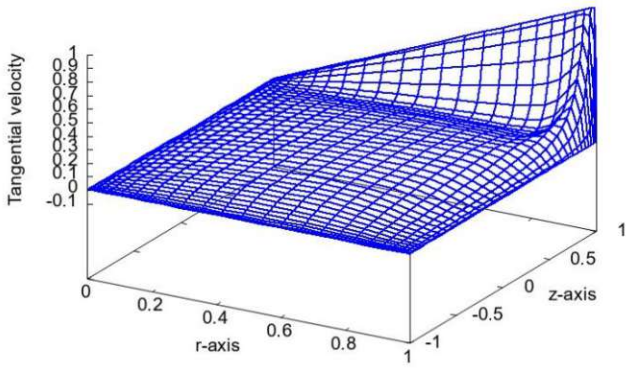

(a)

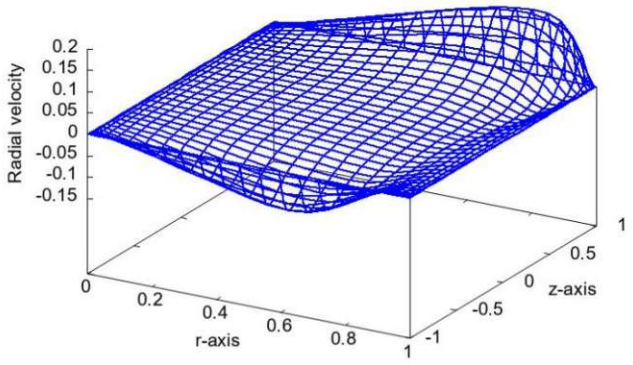

(b)

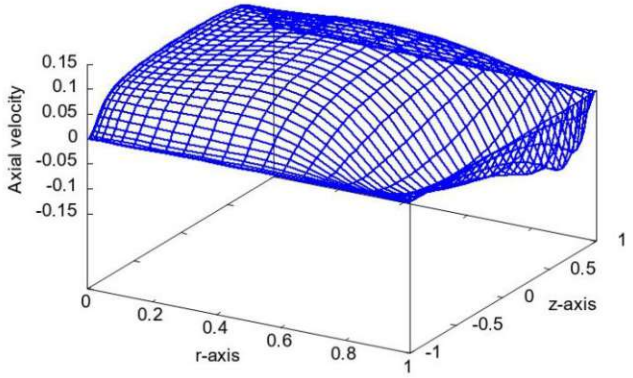

(c)

Figure 10: Velocity components in Single Fluid at Re = 500: Mesh grid (25r x 40z). (a) Tangential Velocity (b) Radial velocity (c) Axial velocity

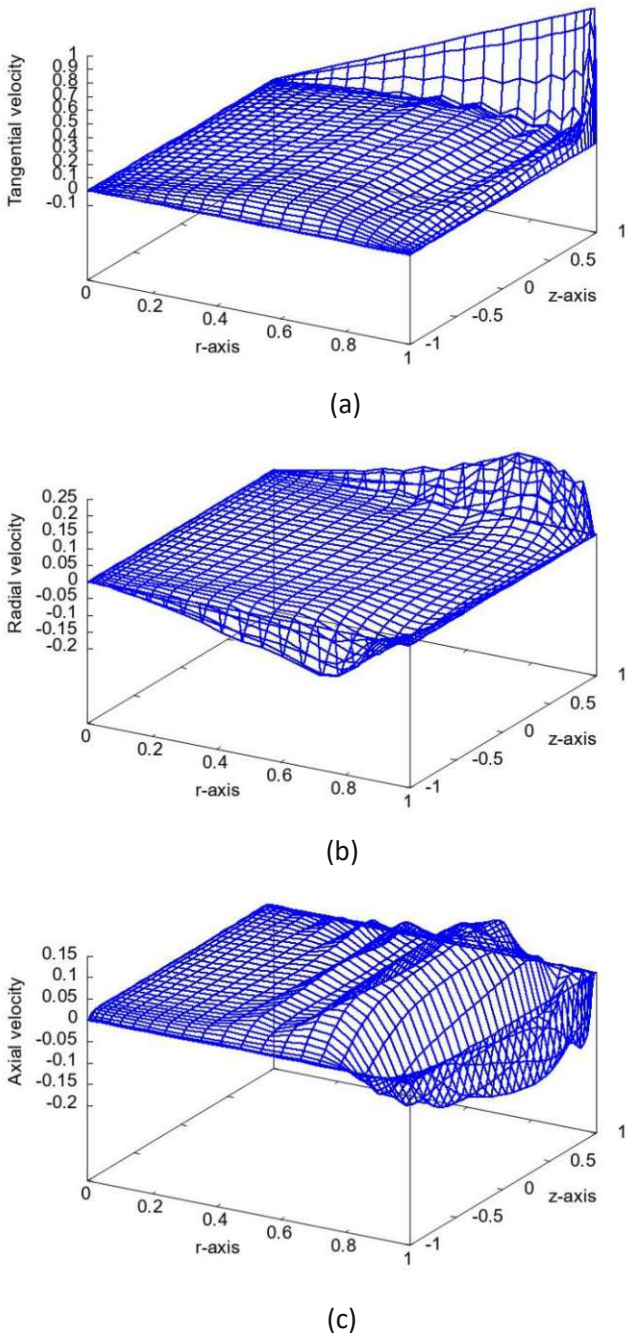

Figure 11: Velocity components in Single Fluid at Re = 6000: Mesh grid (25r x 40z). (a) Tangential Velocity (b) Radial velocity (c) Axial velocity

The initial functions (Figure 10a and Figure 11a) presented in this section focus on tangential velocity. As observed in the diagrams, on the upper surface of the fluid, which is in contact with the lid, the velocity is the same as the lid's velocity due to the non-slip condition. Consequently, at r = 0 on the top surface, the velocity is zero, and as 'r' increases on the top surface, the velocity also increases. Similarly, in contact with the surfaces at the bottom and wall of the cylinder, the velocity is zero due to the non-slip boundary condition.

Compared to the similarity solution, the tangential velocity function in the non-similarity solution exhibits similar behavior at each 'r,' especially away from the boundaries (r = 0 and 1). This similarity increases with distance from the boundaries.

As evident in the radial velocity graphs (Figure 10b and Figure 11b), there are peaks and valleys near the boundaries. As the Reynolds number increases, these features shift closer to the boundaries. When compared to the similarity solution, the radial velocity exhibits similar behavior, particularly away from the boundaries (r = 0 and 1).

The axial velocity graphs (Figure 10c and Figure 11c) display a valley near the cylinder wall. Increasing Reynolds number enhances the variation of axial velocity with 'r.' Like radial and tangential velocity, axial velocity exhibits similarity with the similarity solution, albeit in a narrower range, which diminishes as Reynolds number increases.

4.3.1 Comparison with Results from Literature

In the following, the contour plots for three parameters—stream function, vorticity, and azimuthal velocity—are displayed at different Reynolds numbers: 50, 300, 750, 1000, and 2000. These plots illustrate the variation of these parameters in the cylinder and allow for comparison with available data.

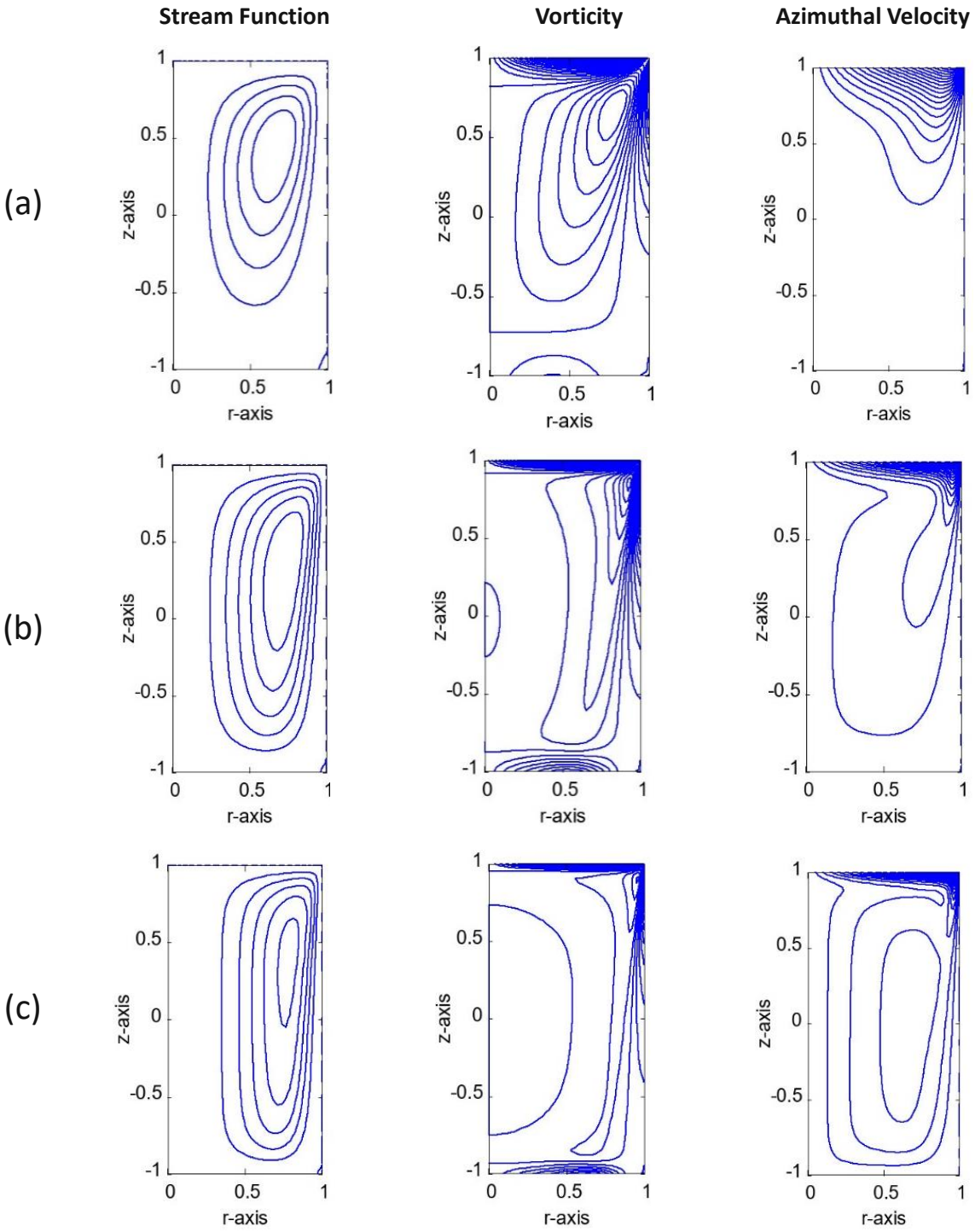

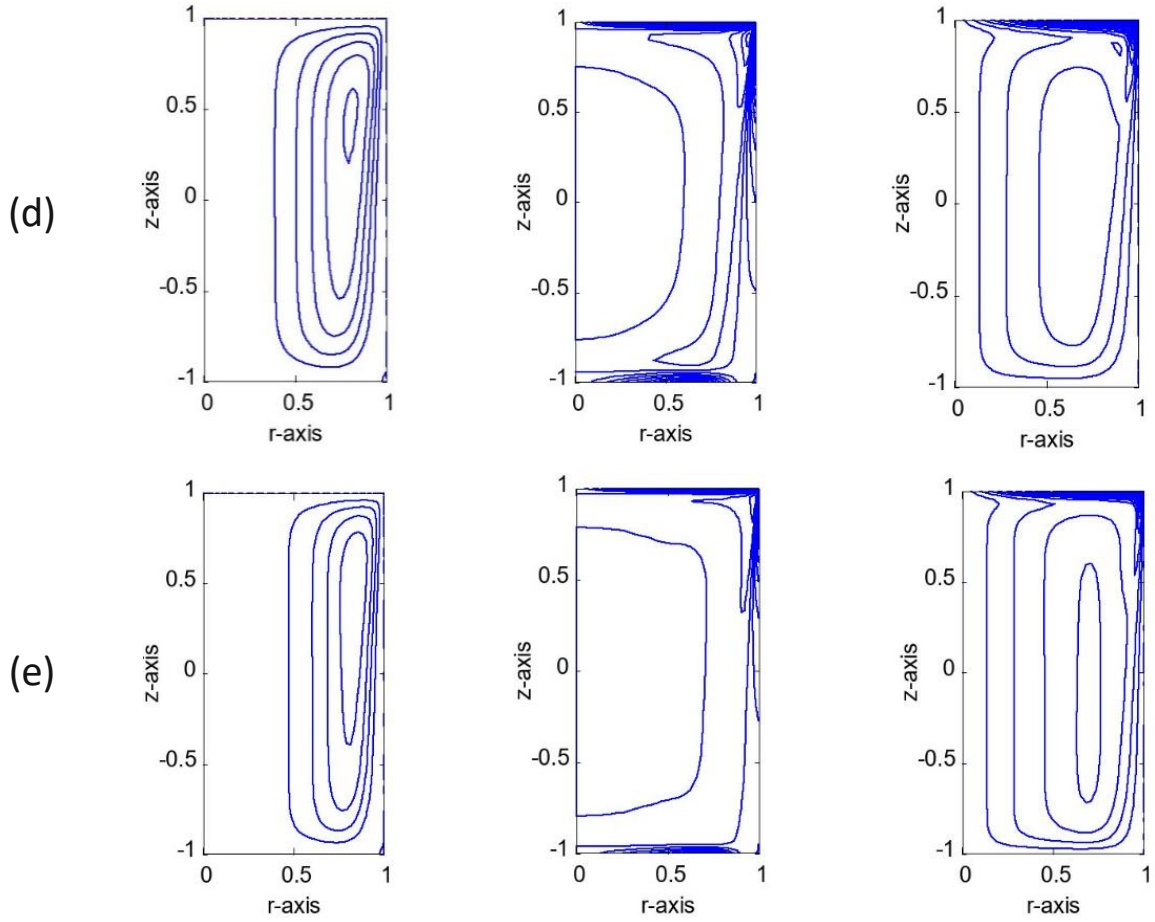

Figure 12: Isolines of Stream Function, Vorticity, and Azimuthal Velocity for h/R=2and Reynolds Numbers: (a) Re=50, (b) Re=300, (c) Re=750, (d) Re=1000 and (e) Re=2000

The stream function, a scalar function widely employed in fluid dynamics, serves to visualize flow patterns within a two-dimensional flow field. Contour lines on a stream function plot represent constant values of the stream function. Streamlines, which are lines parallel to the flow direction, can be visualized by drawing tangent lines to these contour lines. An examination of stream function diagrams Figure 12 at different Reynolds numbers reveals that an increase in Reynolds number causes the maximum of the stream function to shift closer to the wall of the cylinder. As Reynolds number increases, the changes in the flow pattern around the wall and bottom of the cylinder also increase.

Vorticity is a measure of the local spinning motion of fluid particles within a fluid flow. According to the diagram Figure 12, as the Reynolds number increases, the change in vorticity, especially at points farther from the wall, decreases. Contour plots in Figure 12, show as the Reynolds number increases, the change in azimuthal velocity near the bottom of the cylinder increases.

To compare the results with the paper [27], the focus lies on maintaining a constant height-to-radius ratio of one. Simulations were conducted for Reynolds numbers of 50, 500, and 2000. However, limitations arising from the solver provided by NAG restricted the use of a finer grid due to memory allocation errors. Nonetheless, consistent patterns in streamlines, vorticity, and azimuthal velocity were noted across both datasets. The discrepancy between the diagrams presented in the paper and our findings warrants further investigation and is posed as an open question.

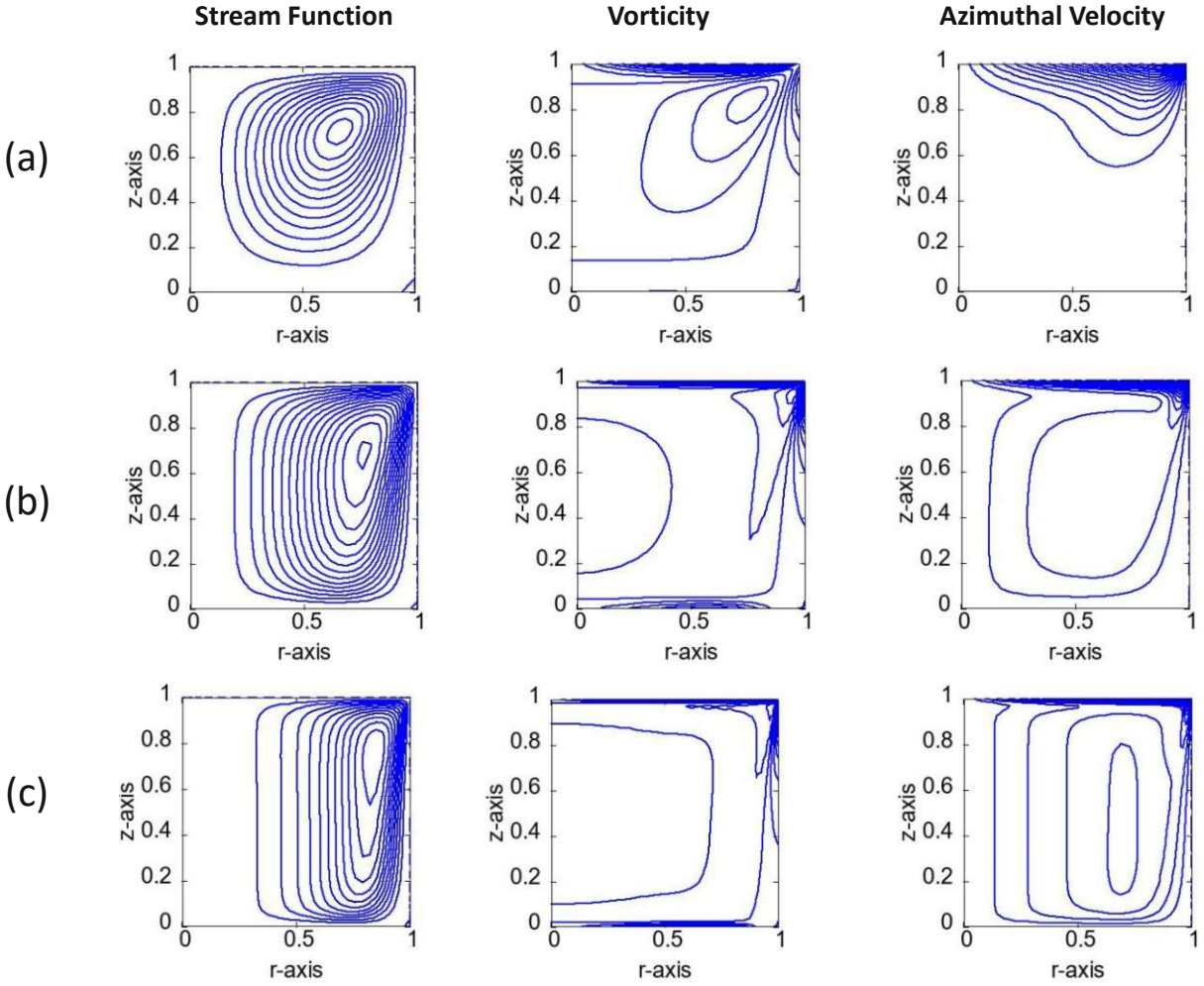

Figure 13: Isolines of Stream Function, Vorticity, and Azimuthal Velocity for h/R=1 and Reynolds Numbers: (a) Re=50, (b) Re=500, (c) Re=2000 generated using the solver developed in this thesis.

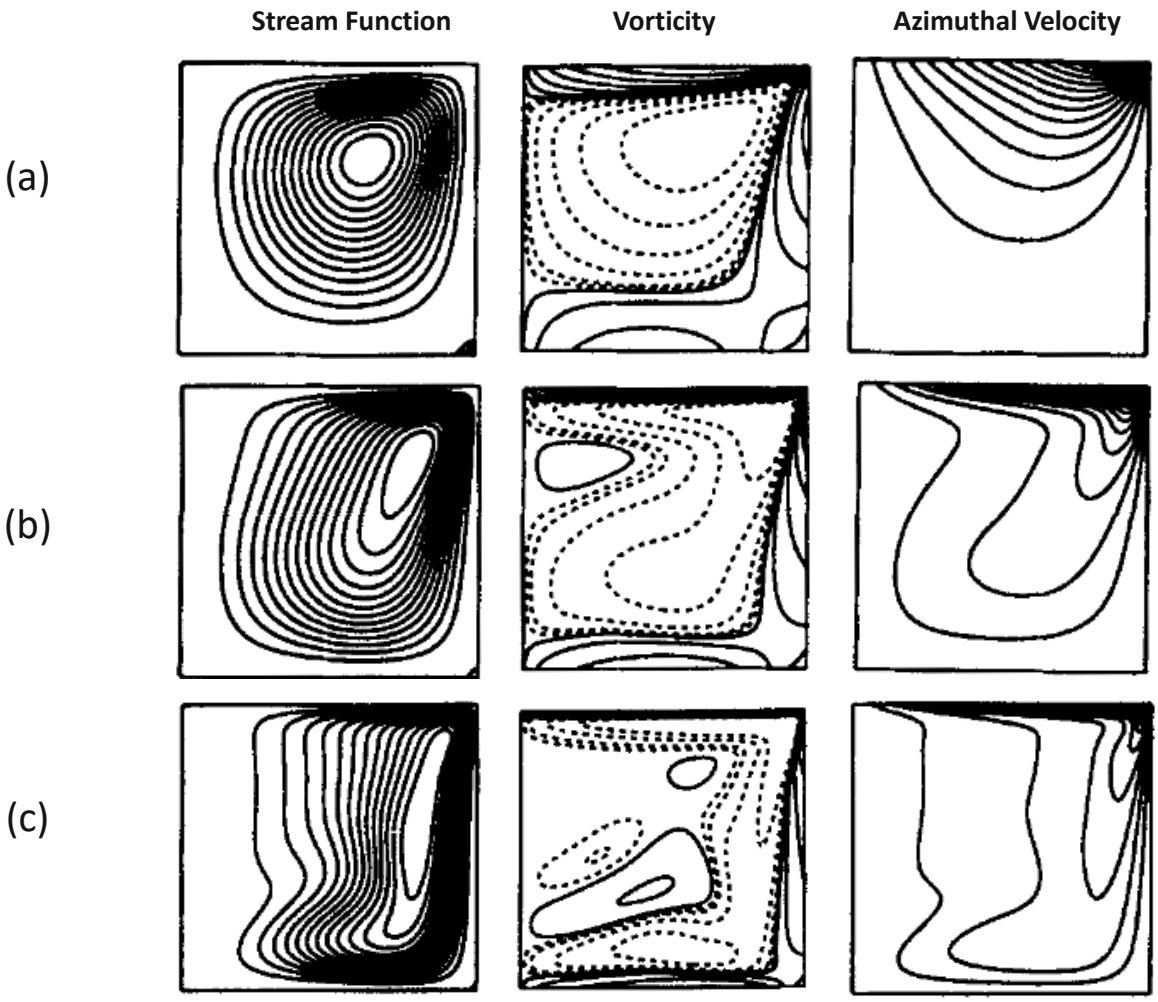

Figure 14: Isolines of Stream Function, Vorticity, and Azimuthal Velocity for h/R=1 and Reynolds Numbers: (a) Re=50, (b) Re=500, (c)Re=2000 Adapted from [22].

4.4 The Flow of Two Immiscible Fluids in a Cylindrical Container

In this section, non-similarity solutions are addressed for a system involving two fluids, which is divided into two parts. The first part considers a flat interface between two miscible fluids, where the limit $Fr = 0$ is applicable. The second part deals with a free interface, where $Fr > 0$.

4.4.1 The Limit Fr = 0

Here is the focus on scenarios where the interface between these non-mixing fluids remains flat, and there is no need for explicit calculations of the interface shape. The emphasis is on understanding the behavior and of the non-similarity solutions in the context of two distinct

fluids, providing valuable insights into the dynamics of interfaces between immiscible fluids without the need for detailed interface characteristics computations.

In the subsequent diagrams, similar to those in the single-fluid case, diagrams depicting axial, radial, and tangential velocity are presented for two cases to avoid overcrowding. The remaining cases can be found in the appendix. Additionally, in this section, like the single-fluid case, counter plots for stream function, vorticity, and azimuthal velocity will be provided for specific cases to enhance understanding of the flow characteristics in both fluids.

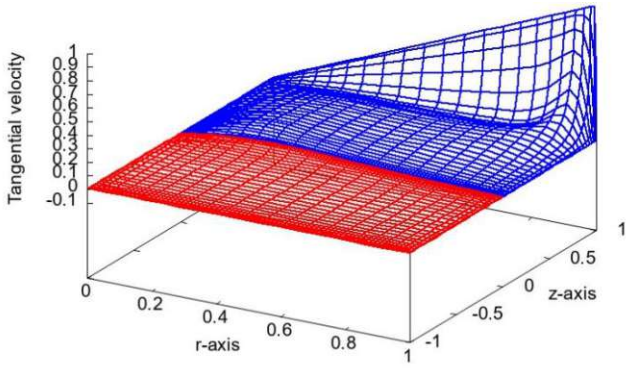

(a)

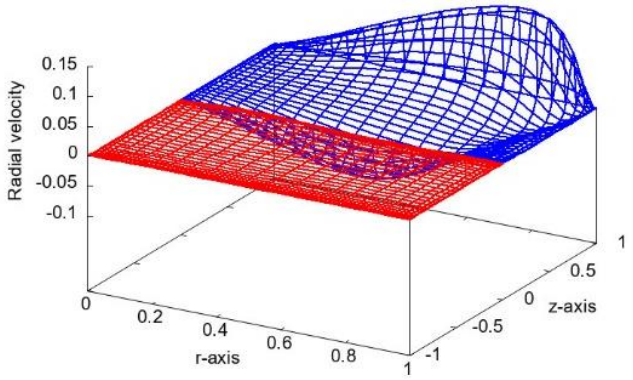

(b)

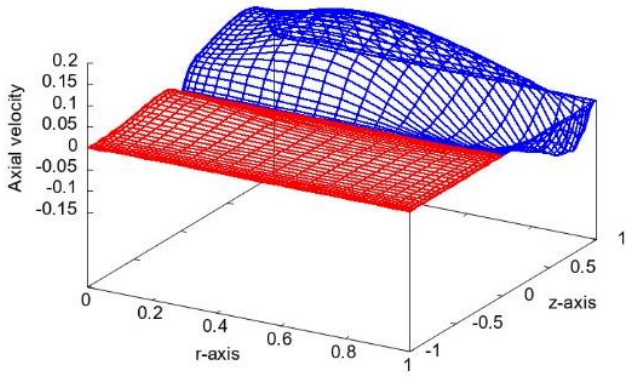

(c)

Figure 15: Velocity components in Two Immiscible Fluids at Re=500, with a Density Ratio of 2 and Dynamic Viscosity Ratio of 1. Mesh Grid: Nr=25, $Nz_{UpFluid}$=30, $Nz_{downfluid}$=30.). (a) Tangential Velocity (b) Radial velocity (c) Axial velocity

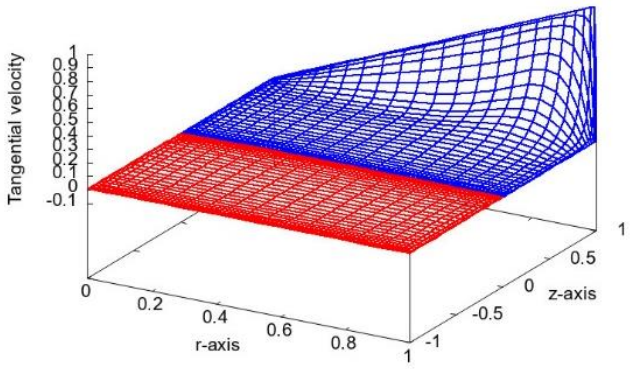

(a)

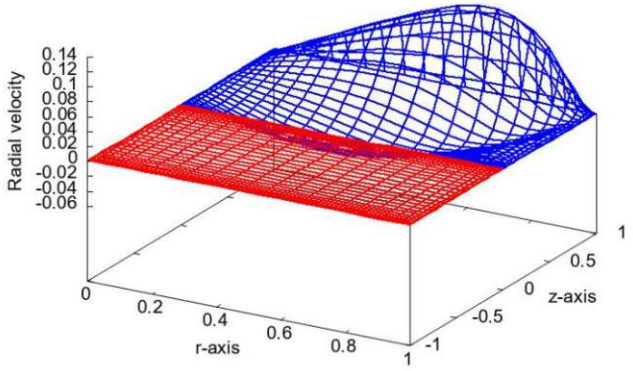

(b)

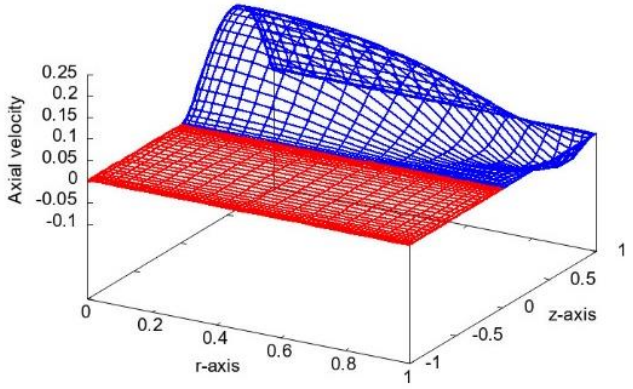

(c)

Figure 16: Velocity components in Two Immiscible Fluids at Re=6000, with a Density Ratio of 50 and Dynamic Viscosity Ratio of 0.5. Mesh Grid: Nr=25, $Nz_{UpFluid}$=30, $Nz_{downfluid}$=30.). (a) Tangential Velocity (b) Radial velocity (c) Axial velocity

In the above diagrams, a rise in the density ratio between fluids shows a change in the upper fluid's behavior, like a single fluid. Additionally, the interface between fluids behaves like a motionless wall. This trend was previously discussed in the similarity solution section. With an increase in Reynolds number, it is observed that the flow in the lower fluid increases.

Examining the tangential velocity diagrams in non-similarity solutions reveals that as one moves away from the boundaries (at r = 0 and r = 1), the solution becomes more akin to the similarity solution.

The radial velocity diagrams in the upper fluid display peaks and valleys. The magnitudes of these peaks and valleys decrease when the upper fluid has higher viscosity. In these observations, the influence of density and viscosity ratios becomes evident at different Reynolds numbers for radial velocity.

Increasing the Reynolds number leads to an increase in the axial velocity in the lower fluid. The impact of viscosity ratio on axial velocity becomes more noticeable with lower Reynolds numbers and in situations with smaller density differences.

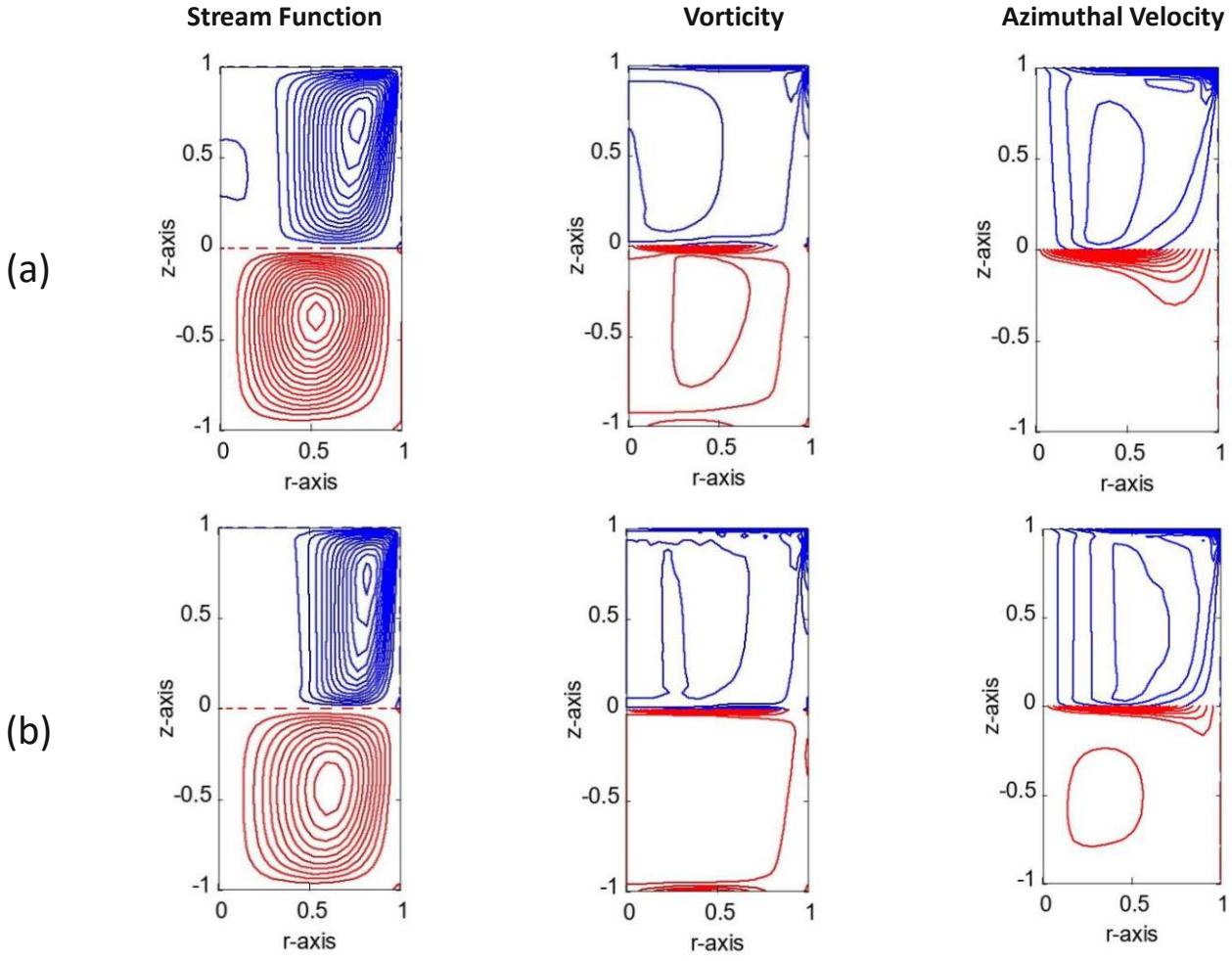

(c)

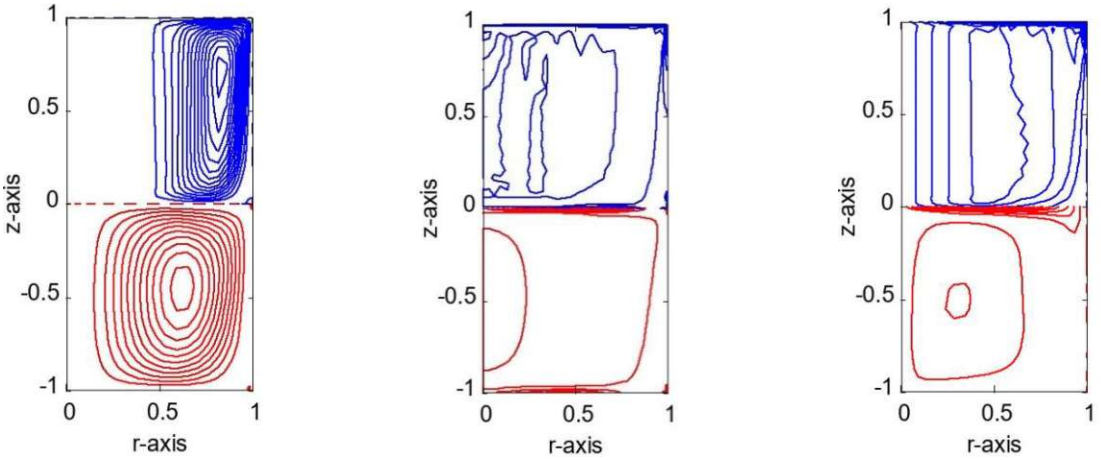

Figure 17: Isolines of Stream Function, Vorticity, and Azimuthal Velocity in Two Immiscible Fluids with a Density ratio 2 , dynamic viscosity ratio 1 and Reynolds Numbers: (a) Re=1000, (b) Re=3000, (c) Re=6000. Mesh Grid: Nr=25, $Nz_{UpFluid}$=30, $Nz_{downfluid}$=30.

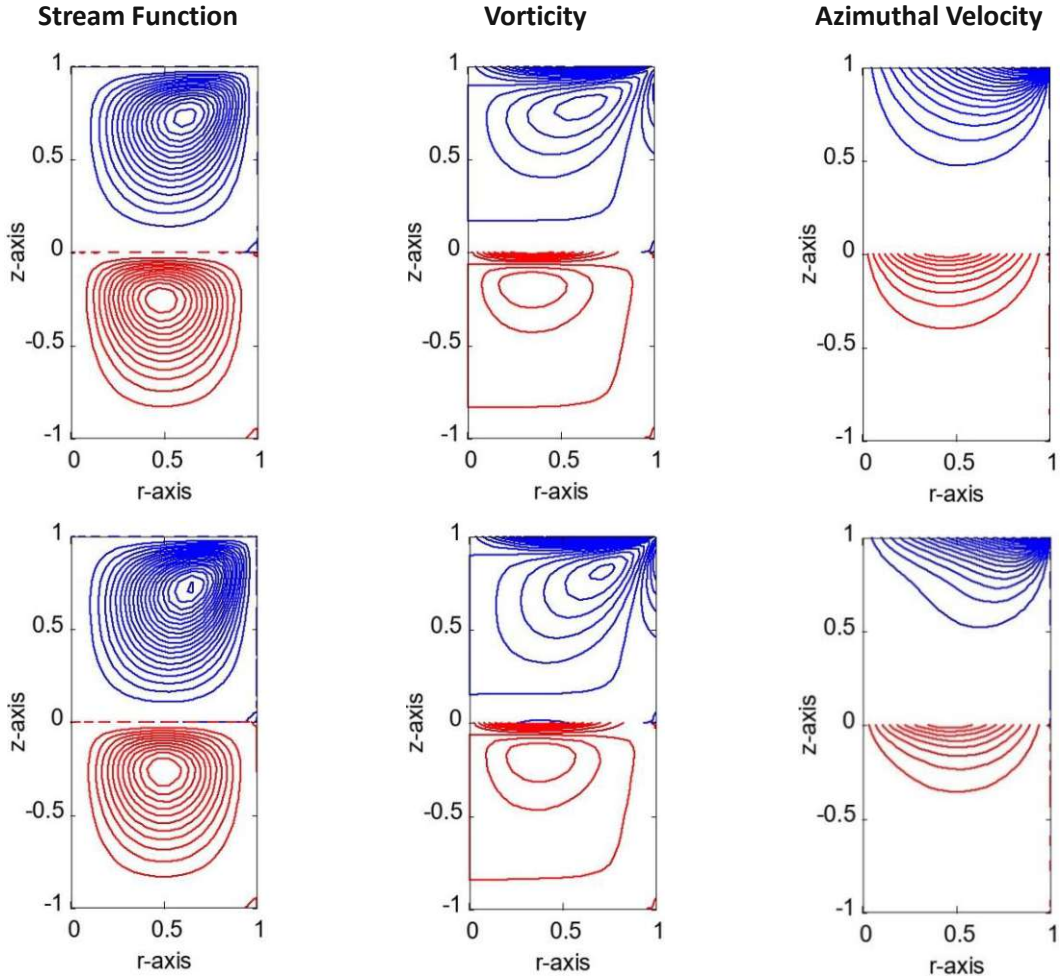

(c)

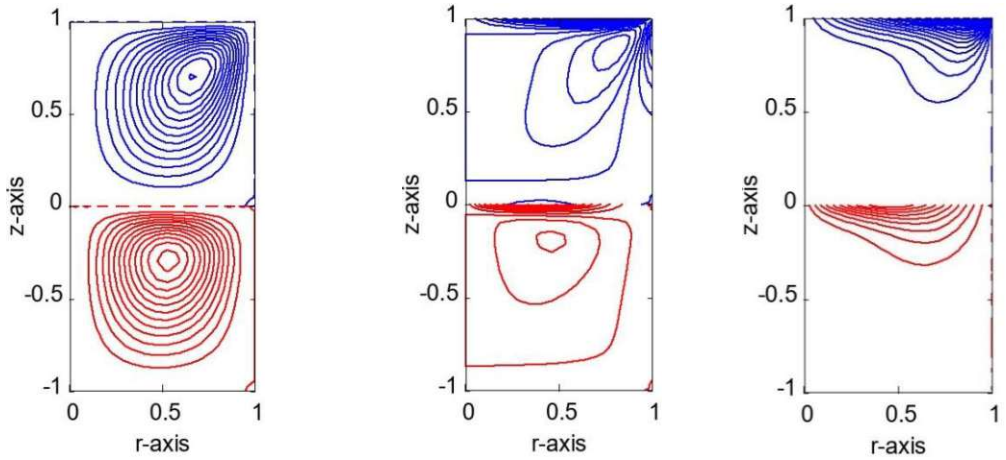

Figure 18: Isolines of Stream Function, Vorticity, and Azimuthal Velocity in Two Immiscible Fluids with a Density ratio 50 , dynamic viscosity ratio 0.5 and Reynolds Numbers: (a) Re=1000, (b) Re=3000, (c) Re=6000. Mesh Grid: Nr=25, $Nz_{UpFluid}$=30, $Nz_{downfluid}$=30.

According to Figure 17, in the streamlines diagram at Reynolds 1000 a vortex can be observed in the center, which diminishes as Reynolds increases. As Reynolds increases, the streamlines in the upper fluid move closer to the wall.

By comparing the diagrams in Figures 17 and 16, it can be observed that as the density ratio of the two fluids increases, the behavior of the fluid in the upper fluid becomes more similar to that of a single fluid in a cylinder.

4.4.2 Fr > 0: Free Interface Problem

In this section, the interface between two immiscible fluids is analyzed. As previously mentioned, the solution must incorporate parameters such as pressure difference and surface displacement at the interface. Accordingly, the equation for pressure difference at the interface and the surface displacement at the interface are integrated into the system of equations. Initially, the surface tension and the difference in normal stress on the interface are overlooked in the surface displacement equation. Nevertheless, in subsequent analyses, both parameters are considered to assess their impact on the solution.

In this section, our main goal is to illustrate essential interface parameters, including surface displacement, pressure difference, and shear stress in both radial and tangential directions. The investigation will encompass a range of Reynolds numbers, ranging from 500 to 6000, while ensuring a constant Froude number of one.

In terms of numerical solution, a grid comprising 25 points is employed in the radial direction, along with 60 grids in the axial direction (30 for the upper fluid and 30 for the lower fluid).

The analysis of surface displacement at the interface between two fluids will be undertaken for three distinct cases, each characterized by different density ratios and viscosity ratios.

As seen in the surface displacement diagrams and their comparison, it is evident that the surface displacement at the interface approaches zero as the density difference increases until the Reynolds number is sufficiently large (not achieved here). Therefore, our analyses in the previous section, assuming a flat interface, remain valid for scenarios characterized by a high difference in density. Additionally, an increase in viscosity in the upper fluid results in a smoother displacement of the surface. The surface displacement exhibits a wave pattern, with peak towards the wall and valley at the center. The axial symmetry is evident in the zero-slope observed at the center. Furthermore, an increase in Reynolds number corresponds to a proportional augmentation in surface displacement.

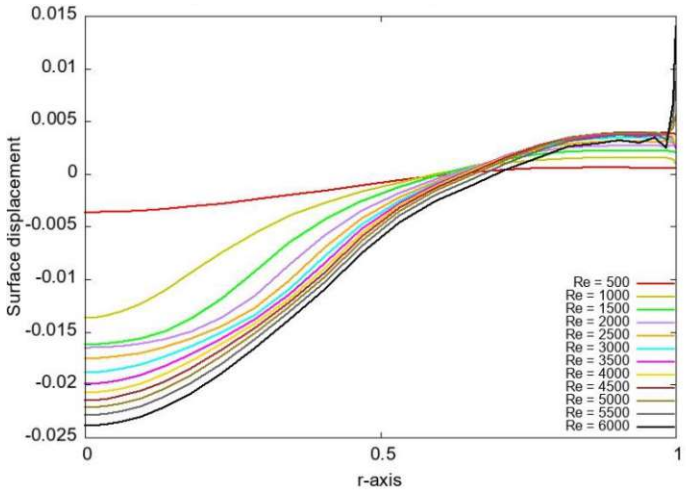

Figure 19: Surface displacement Surface displacement of Interface Between Two Immiscible Fluids at Different Reynolds Numbers, with a Density Ratio of 2 and Dynamic Viscosity Ratio of 0.5. Mesh Grid: Nr=25, $Nz_{UpFluid}$=30, $Nz_{DownFluid}$=30.

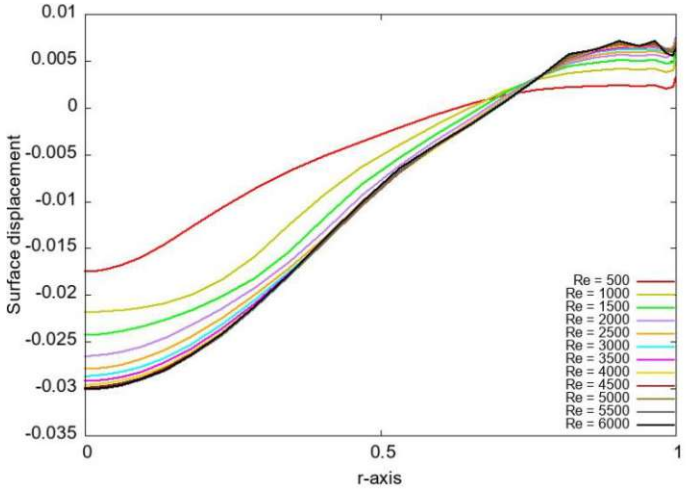

Figure 20: Surface displacement of Interface Between Two Immiscible Fluids at Different Reynolds Numbers, with a Density Ratio of 2 and Dynamic Viscosity Ratio of 1. Mesh Grid: Nr=25, $Nz_{UpFluid}$=30, $Nz_{DownFluid}$=30.

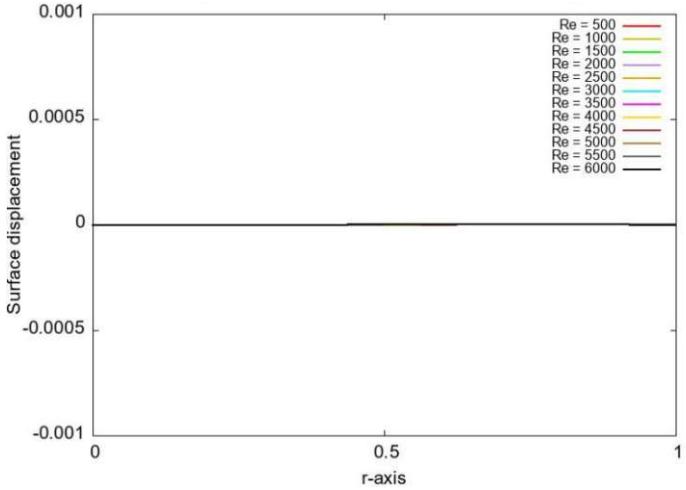

Figure 21: Surface displacement of Interface Between Two Immiscible Fluids at Different Reynolds Numbers, with a Density Ratio of 50 and Dynamic Viscosity Ratio of 1. Mesh Grid: Nr=25, $Nz_{UpFluid}$=30, $Nz_{DownFluid}$=30.

From this point onward, the analysis of other interface parameters between two fluids will exclusively concentrate on the case where the surface displacement was the most pronounced, as observed in the latest diagrams.

Because the Froude Number is fixed at one, and both surface tension and normal stress differences between the two fluids at the interface are disregarded in the system's surface equation, the behavior of the pressure difference closely mirrors that of the surface displacement. This correspondence is evident in the case presented below.

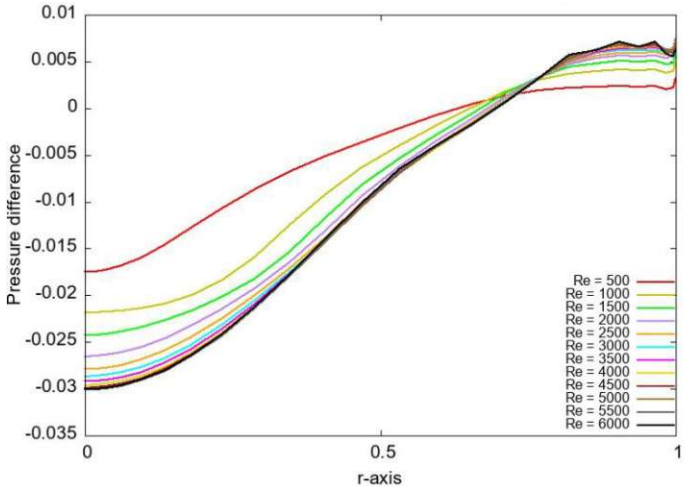

Figure 22: Pressure difference across the Interface Between Two Immiscible Fluids at Different Reynolds Numbers, with a Density Ratio of 2 and Dynamic Viscosity Ratio of 1. Mesh Grid: Nr=25, $Nz_{UpFluid}$=30, $Nz_{DownFluid}$=30.

In both the tangential and radial shear stress diagrams, there are observable peaks that, as the Reynolds number increases, shift towards the wall. The tangential and radial shear stresses exhibit an upward trend with increasing Reynolds numbers.

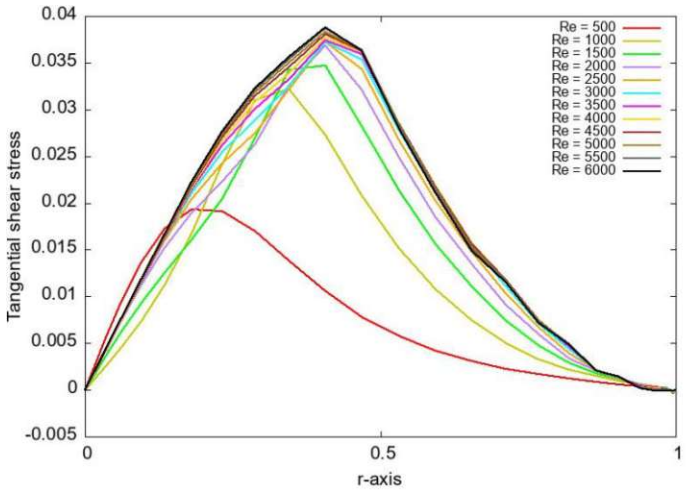

Figure 23: Tangential shear stress across the Interface Between Two Immiscible Fluids at Different Reynolds Numbers, with a Density Ratio of 2 and Dynamic Viscosity Ratio of 1. Mesh Grid: Nr=25, $Nz_{UpFluid}$=30, $Nz_{DownFluid}$=30.

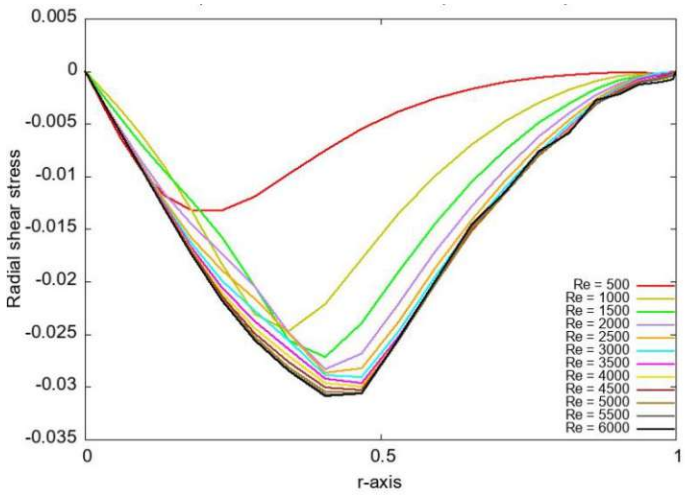

Figure 24: Radial shear stress across the Interface Between Two Immiscible Fluids at Different Reynolds Numbers, with a Density Ratio of 2 and Dynamic Viscosity Ratio of 1. Mesh Grid: Nr=25, $Nz_{UpFluid}$=30, $Nz_{DownFluid}$=30.

In the following diagrams Figure 25, the results of velocity components at the interface are shown.

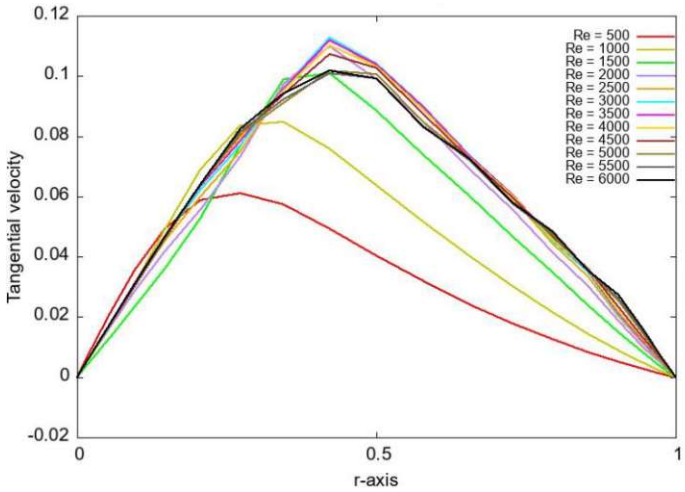

(a)

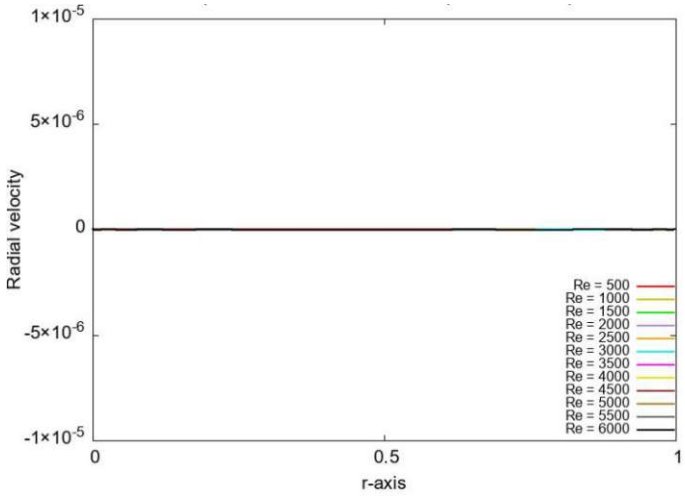

(b)

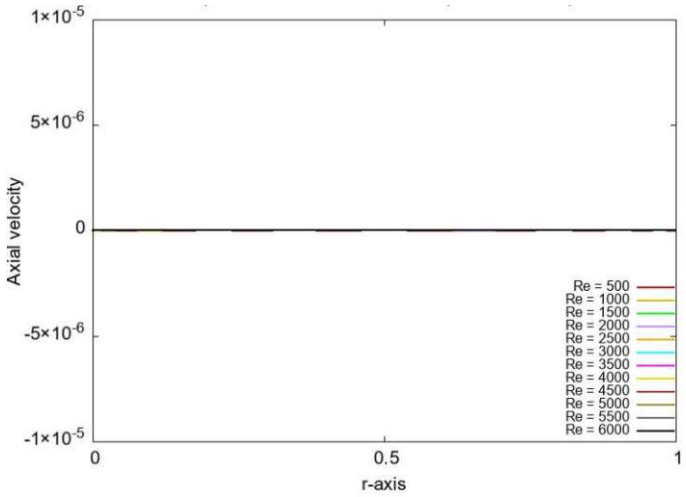

(c)

Figure 25:Velocity components across the Interface Between Two Immiscible Fluids at Different Reynolds Numbers, with a Density Ratio of 2 and Dynamic Viscosity Ratio of 1. Mesh Grid: Nr=25, $Nz_{UpFluid}$=30, $Nz_{DownFluid}$=30.(a) Tangential Velocity (b) Radial velocity (c) Axial velocity

For better comprehension, velocity components at r = 0.75 with respect to z-axis of the cylinder are presented in Figure 26.

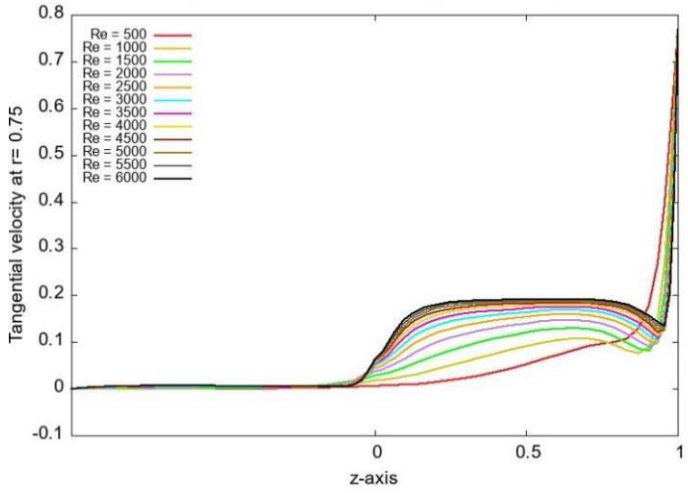

(a)

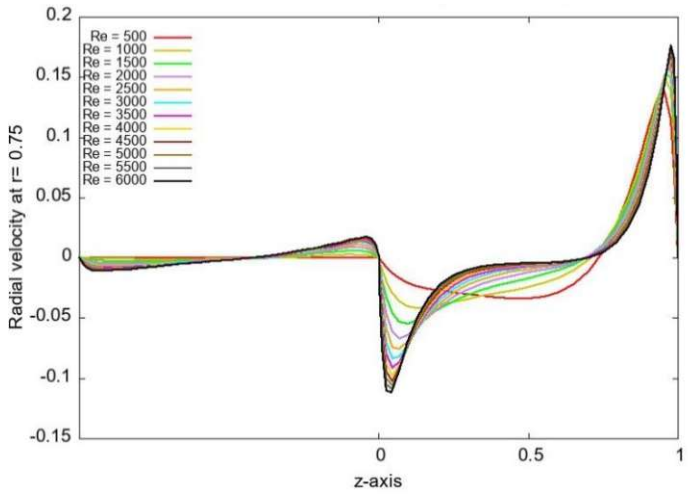

(b)

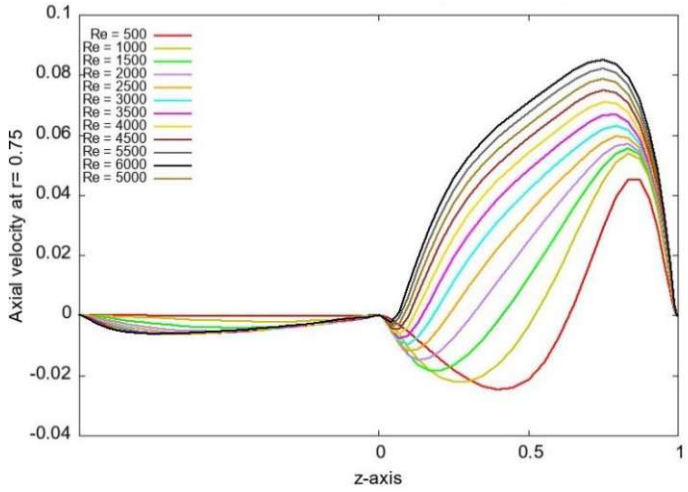

(c)

Figure 26: Velocity components at r = 0.75, at Different Reynolds Numbers, with a Density Ratio of 2 and Dynamic Viscosity Ratio of 1. Mesh Grid: Nr=25, $Nz_{UpFluid}$=30, $Nz_{DownFluid}$=30.(a) Tangential Velocity (b) Radial velocity (c) Axial velocity

In the subsequent analysis, a comparison of the stream function for the mentioned case at Reynolds 6000, considering the interface displacement and assuming a flat interface between the two fluids, will be performed. This comparison aims to reveal that at this Reynolds number, the interface displacement in this case does not significantly impact the flow in both fluids.

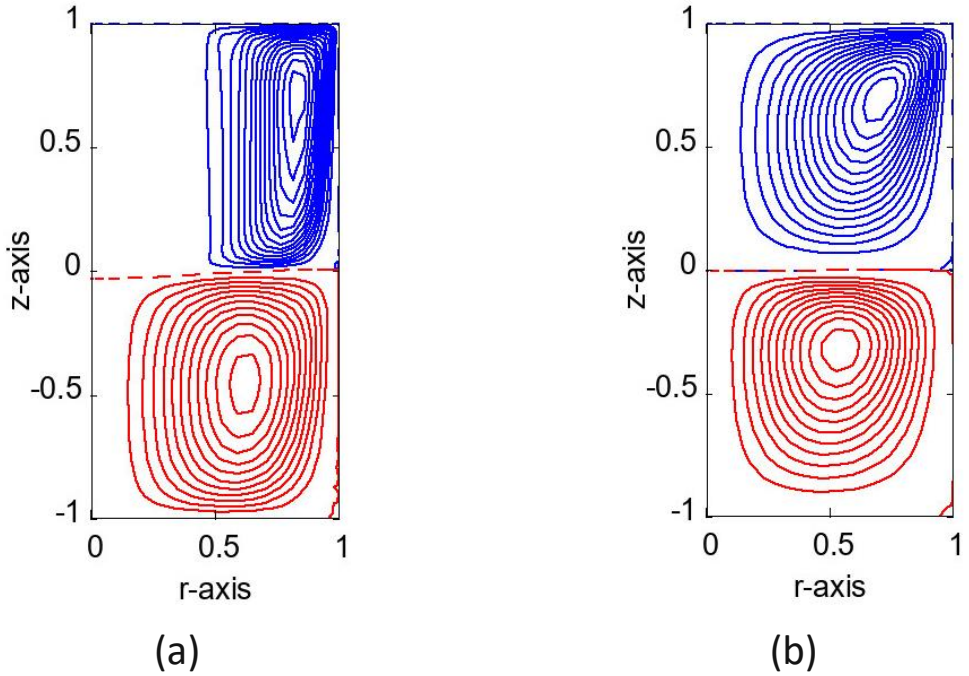

Figure 27: Stream Function in Two Immiscible Fluids at Reynolds=6000. (a): Density Ratio of 2 and Dynamic Viscosity Ratio of 1. (b): Density Ratio of 50 and Dynamic Viscosity Ratio of 1. Mesh Grid: Nr=25, NzUpFluid=30, NzDownFluid=30.

Until now, the influence of surface tension and normal stress difference at the interface in comparison to the pressure difference has been overlooked. The current objective is to incorporate these factors and analyze the interface parameters across various Weber numbers.

For this purpose, the Reynolds number is fixed at 1000, while the Froude number remains consistently at one. The density ratio and viscosity ratio are maintained at constant values.

The diagram showcases the surface displacement of the interface for various Weber numbers, encompassing the scenario where neither surface tension nor normal stress difference at the interface is considered. Upon closer examination of the surface displacement diagram, it becomes apparent that in comparison to the pressure difference, the effects of surface tension and normal stress difference are relatively smaller. Additionally, as the Weber number increases, the influence of surface tension diminishes.

These observations suggest that varying the Weber number has minimal effects on the interface parameters, as depicted in the diagrams.

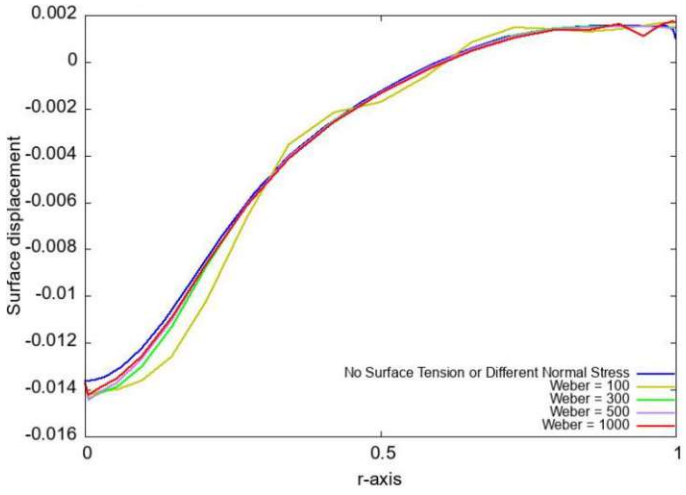

Figure 28: Surface displacement Surface displacement of Interface Between Two Immiscible Fluids at Reynolds = 1000 and different Weber numbers, with a Density Ratio of 2 and Dynamic Viscosity Ratio of 1. Mesh Grid: Nr=25, $Nz_{UpFluid}$=30, $Nz_{DownFluid}$=30.

When the Froude number is set to one, the pressure difference and surface displacement exhibit similar behaviors at the interface. However, introducing considerations for surface tension and normal stress difference at the interface very slightly diminishes this similarity.

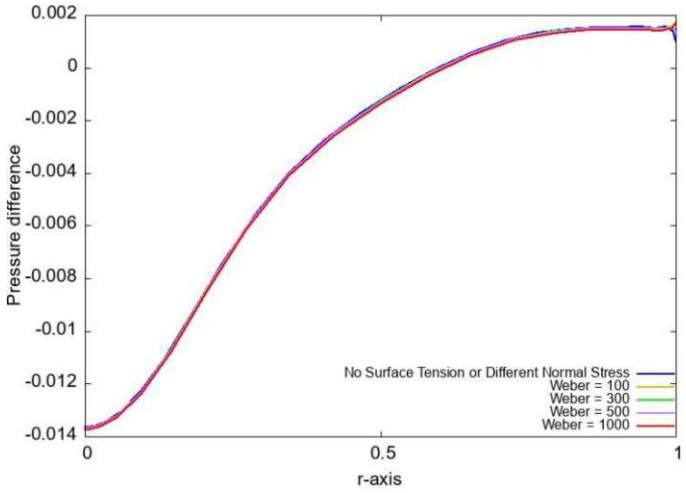

Figure 29: Pressure difference across the Interface Between Two Immiscible Fluids at Reynolds = 1000 and different Weber numbers, with a Density Ratio of 2 and Dynamic Viscosity Ratio of 1. Mesh Grid: Nr=25, $Nz_{UpFluid}$=30, $Nz_{DownFluid}$=30.

Considering the surface tension and normal stress difference at the interface between fluids, it appears that the pressure difference at the interface has a greater effect on the resulting tangential and radial stress. Therefore, it may be appropriate to ignore these effects in the calculation.

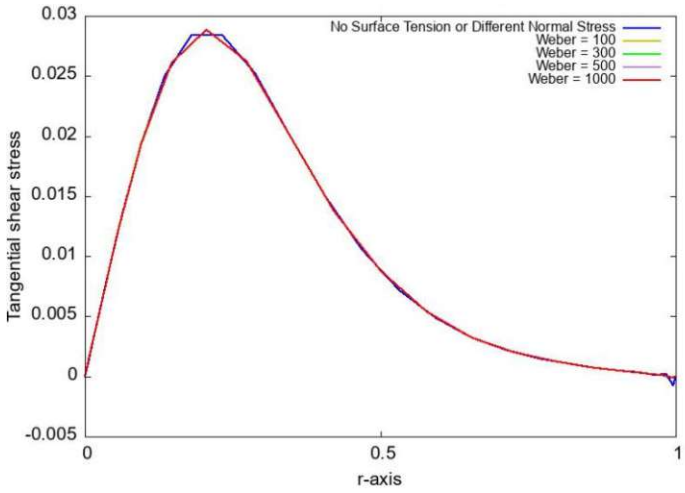

Figure 30: Tangential Shear stress across the Interface Between Two Immiscible Fluids at Reynolds = 1000 and different Weber numbers, with a Density Ratio of 2 and Dynamic Viscosity Ratio of 1. Mesh Grid: Nr=25, $Nz_{UpFluid}$=30, $Nz_{DownFluid}$=30.

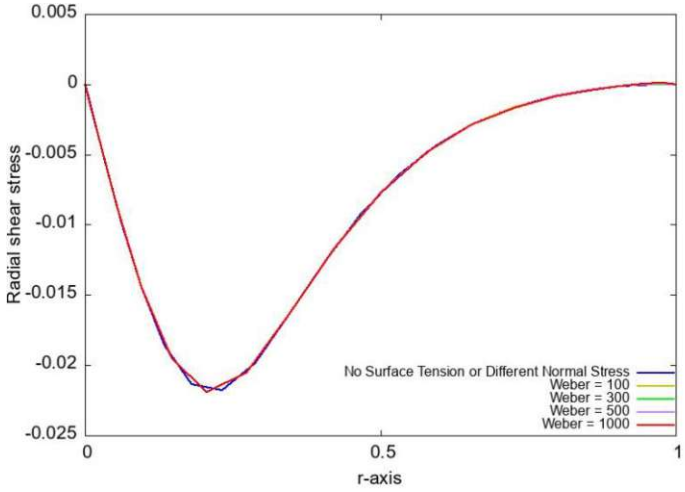

Figure 31: Radial shear stress across the Interface Between Two Immiscible Fluids at Reynolds = 1000 and different Weber numbers, with a Density Ratio of 2 and Dynamic Viscosity Ratio of 1. Mesh Grid: Nr=25, $Nz_{UpFluid}$=30, $Nz_{DownFluid}$=30.

The following plot compares the magnitude of the pressure difference component with the $\frac{\mathrm{Fr}}{\mathrm{Web}}\,\kappa$ and $\frac{\mathrm{Fr}}{\mathrm{Re}}\left(s_{F,n}-\mu s_{G,n}\right)$components of the surface displacement equation(2-27)as a function of radial distance from the center.

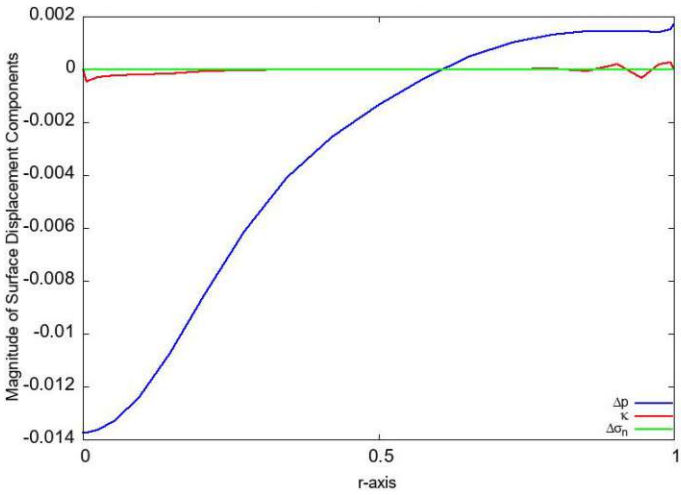

Figure 32: Magnitude of Surface Displacement Components in Interface Between Two Immiscible Fluids at Reynolds = 1000, Weber = 1000, with a Density Ratio of 2 and Dynamic Viscosity Ratio of 1. . Mesh Grid: Nr=25, $Nz_{UpFluid}$=30, $Nz_{DownFluid}$=30.

The x-axis represents the radial distance from the center of the surface. The y-axis indicates the magnitude of each component contributing to the surface displacement equation at each radial distance.

- Δp: Represents the difference in pressure at interface.
- κ: Represents the curvature of the surface.
- $\Delta\sigma_n$: Represents the change in normal stress at the interface.

The plot highlights the relative magnitudes of the pressure difference component compared to curvature and delta normal stress. Based on the comparison, if the pressure difference component significantly outweighs curvature and delta normal stress, simplification of the surface displacement equation by omitting these components can be considered.

4.5 Comparison with Experiments

Here we attempt to compare our results with exact experimental data[28]. For this purpose, our code is configured to match the experimental setup, including the density ratio, viscosity ratio, and the height of each fluid. The tangential velocity at the interface is investigated for comparison with the data. It is observed that increasing the Reynolds number reduces the difference between the result.

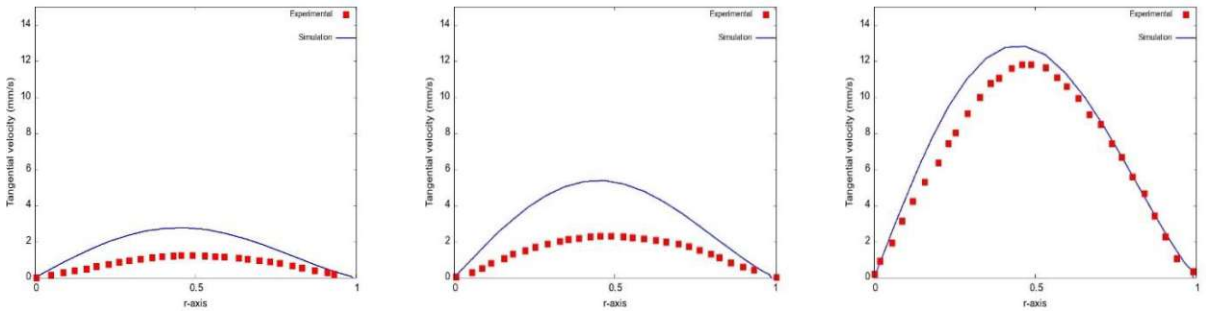

(a) (b) (c)

Figure 33: Tangential Velocity at interface between two fluids to compared with experimental data (a) Re = 50 (b) Re = 100 (c) Re = 250

In our comparison, we employed the simulation with a grid size of (Nr = 25 and Nz = 60). Unfortunately, we encountered a memory allocation error when attempting to use a finer grid. This limitation could potentially lead to differences in the results. Additionally, our numerical solutions were based on assumptions such as axial symmetry, although in reality, axial symmetry was not present. Furthermore, we did not adjust the Weber and Froude numbers in our simulation due to their absence in the paper. Despite their seemingly minor influence, these parameters could still impact the results.

5 Conclusion

This study investigated the flow behavior of two immiscible liquids in a vertical cylinder with a rotating lid. By employing Navier-Stokes equations in cylindrical coordinates and utilizing spectral methods as a numerical solution, the flow characteristics of both fluids were determined.

The research examined the velocity components behavior, including tangential, radial, and axial velocities, across a spectrum of Reynolds numbers and other dimensional parameters such as density ratio, viscosity ratio, Weber number, and more, by analyzing both similarity and non-similarity solutions.

To analyse the flows in both liquids, treated as separate phases due to their non-mixing nature, the Navier-Stokes equations in cylindrical coordinates were applied. Certain assumptions, such as axial symmetry and steady state, were considered to simplify these equations.

Initially, a similarity solution was employed to describe the flow between two disks of infinite length. This solution effectively removes any dependence on radial variables from the equations, leaving only the z-axis as the sole variable. Although the similarity solution lacked detailed insights, it provided a broad perspective on the flow characteristics in both single-fluid and two-fluid scenarios.

In this thesis, the interface between fluids was addressed step by step; at first equations were solved under the assumption of a flat interface between the two fluids, and these results were subsequently used as initial values for equations resolving interfaces.

For single-fluid cases, the similarity solution revealed consistent velocity patterns across Reynolds numbers, with tangential velocity reaching a constant value. Extending the analysis to two-fluid systems highlighted the influence of density and viscosity ratios on flow behavior, particularly near boundaries. As density ratios increase, it was observed that the upper fluid demonstrates behavior increasingly resembling that of a single fluid.

In non-similarity solutions, counter plots for stream function, vorticity, and azimuthal velocity were used to better understand the flow.

When examining free interface scenarios between two fluids, Reynolds numbers, viscosity ratio, density ratio, Weber, and Froude numbers were considered. It was observed that an increase in Reynolds number corresponded to an increase in the displacement of the

interface. However, this increase depends on factors such as the density ratio and other dimensionless numbers like the Froude and Weber numbers. For example, a higher density ratio between the two fluids resulted in a lower surface displacement compared to cases with lower density ratios.

As a topic for future investigation the instability at the interface between the fluids is of special importance. This instability leads to the formation of waves with significant amplitudes. This phenomenon is observed e.g. in Francis turbines during the condenser mode, where the water level in the draft tube decreases. As a result, the turbine's runner rotates in the air, and this rotational movement of the rotor has the potential to generate a substantial surface wave with a significant amplitude [29]. This amplitude can be as large as the diameter of the draft tube.

6 References

[1] P. Childs, *Rotating flow*. Elsevier, 2010.

[2] R. Baltensperger and M. R. Trummer, “Spectral differencing with a twist,” *SIAM journal on scientific computing*, vol. 24, no. 5, pp. 1465–1487, 2003.

[3] N. Rott and W. S. Lewellen, “Boundary layers in rotating flows,” in *Applied Mechanics: Proceedings of the Eleventh International Congress of Applied Mechanics Munich (Germany) 1964*, 1966, pp. 1030–1036.

[4] Y. Jaluria, “Fluid flow phenomena in materials processing—the 2000 freeman scholar lecture,” *J. Fluids Eng.*, vol. 123, no. 2, pp. 173–210, 2001.

[5] V. Prasad, H. Zhang, and A. P. Anselmo, “Transport phenomena in Czochralski crystal growth processes,” *Adv Heat Transf*, vol. 30, pp. 313–435, 1997.

[6] K. Stewartson, “On the flow between two rotating coaxial disks,” in *Mathematical Proceedings of the Cambridge Philosophical Society*, 1953, pp. 333–341.

[7] H. U. Vogel, “Experimentelle Ergebnisse über die laminare Strömung in einen zylindrischen Gehäuse mit darin rotierender Scheibe,” *Max Plank Inst. Berichi*, vol. 6, 1968.

[8] M. P. Escudier, “Observations of the flow produced in a cylindrical container by a rotating endwall,” *Exp Fluids*, vol. 2, no. 4, pp. 189–196, 1984.

[9] B. R. Sharifullin and I. V Naumov, “Angular momentum transfer across the interface of two immiscible liquids,” *Thermophysics and Aeromechanics*, vol. 28, no. 1, pp. 65–76, 2021.

[10] S. Fujimoto and Y. Takeda, “Topology changes of the interface between two immiscible liquid layers by a rotating lid,” *Phys Rev E*, vol. 80, no. 1, p. 15304, 2009.

[11] I. V Naumov, V. G. Glavny, B. R. Sharifullin, and V. N. Shtern, “Formation of a thin circulation layer in a two-fluid rotating flow,” *Phys Rev Fluids*, vol. 4, no. 5, p. 54702, 2019.

[12] P. K. Kundu, I. M. Cohen, and D. R. Dowling, *Fluid mechanics*. Academic press, 2015.

[13] G. N. Lance and M. H. Rogers, “The axially symmetric flow of a viscous fluid between two infinite rotating disks,” *Proc R Soc Lond A Math Phys Sci*, vol. 266, no. 1324, pp. 109–121, 1962.

[14] M. V Salnikov, I. S. Vozhakov, I. V Naumov, and R. I. Mullyadzhanov, “Swirling flow of two immiscible fluids in a cylindrical container: Lattice Boltzmann and volume-of-fluid study,” *Physics of Fluids*, vol. 36, no. 1, 2024.

[15] W. Yang, I. Delbende, Y. Fraigneau, and L. M. Witkowski, “Large axisymmetric surface deformation and dewetting in the flow above a rotating disk in a cylindrical tank: spin-up and permanent regimes,” *Phys Rev Fluids*, vol. 5, no. 4, p. 44801, 2020.

[16] A. Rashkovan, S. D. Amar, U. Bieder, and G. Ziskind, “Analysis of polygonal vortex flows in a cylinder with a rotating bottom,” *Applied Sciences*, vol. 11, no. 3, p. 1348, 2021.

[17] L. Kahouadji and L. M. Witkowski, “Free surface due to a flow driven by a rotating disk inside a vertical cylindrical tank: axisymmetric configuration,” *Physics of Fluids*, vol. 26, no. 7, 2014.

[18] W. Yang, I. Delbende, Y. Fraigneau, and L. M. Witkowski, “Axisymmetric rotating flow with free surface in a cylindrical tank,” *J Fluid Mech*, vol. 861, pp. 796–814, 2019.

[19] J. Mougel, D. Fabre, L. Lacaze, and T. Bohr, “On the instabilities of a potential vortex with a free surface,” *J Fluid Mech*, vol. 824, pp. 230–264, 2017.

[20] P. J. Pritchard and J. W. Mitchell, *Fox and McDonald’s introduction to fluid mechanics*. John Wiley & Sons, 2016.

[21] T. Wierzbicki, “Mechanical Engineering Structural Mechanics,” 2013.

[22] M. P. Do Carmo, *Differential geometry of curves and surfaces: revised and updated second edition*. Courier Dover Publications, 2016.

[23] J. Phillips, *The NAG Library: a beginners guide*. Oxford University Press, Inc., 1987.

[24] D. A. Kopriva, *Implementing spectral methods for partial differential equations: Algorithms for scientists and engineers*. Springer Science & Business Media, 2009.

[25] J. J. Moré, B. S. Garbow, and K. E. Hillstrom, “User guide for MINPACK-1,” 1980.

[26] G. N. Lance and M. H. Rogers, “The axially symmetric flow of a viscous fluid between two infinite rotating disks,” *Proc R Soc Lond A Math Phys Sci*, vol. 266, no. 1324, pp. 109–121, 1962.

[27] A. Y. Gelfgat, P. Z. Bar-Yoseph, and A. Solan, “Stability of confined swirling flow with and without vortex breakdown,” *J Fluid Mech*, vol. 311, pp. 1–36, 1996.

[28] I. V Naumov, B. R. Sharifullin, and V. N. Shtern, “Flow at the interface of two rotating fluids,” in *Journal of Physics: Conference Series*, 2019, p. 12026.

[29] H. Steinrück and A. Maly, “The growth of a rotary gravitiy wave in a cylindrical container,” *Wasserwirtsch. Extra*, vol. 109, pp. 24–29, 2019.

7 Appendix

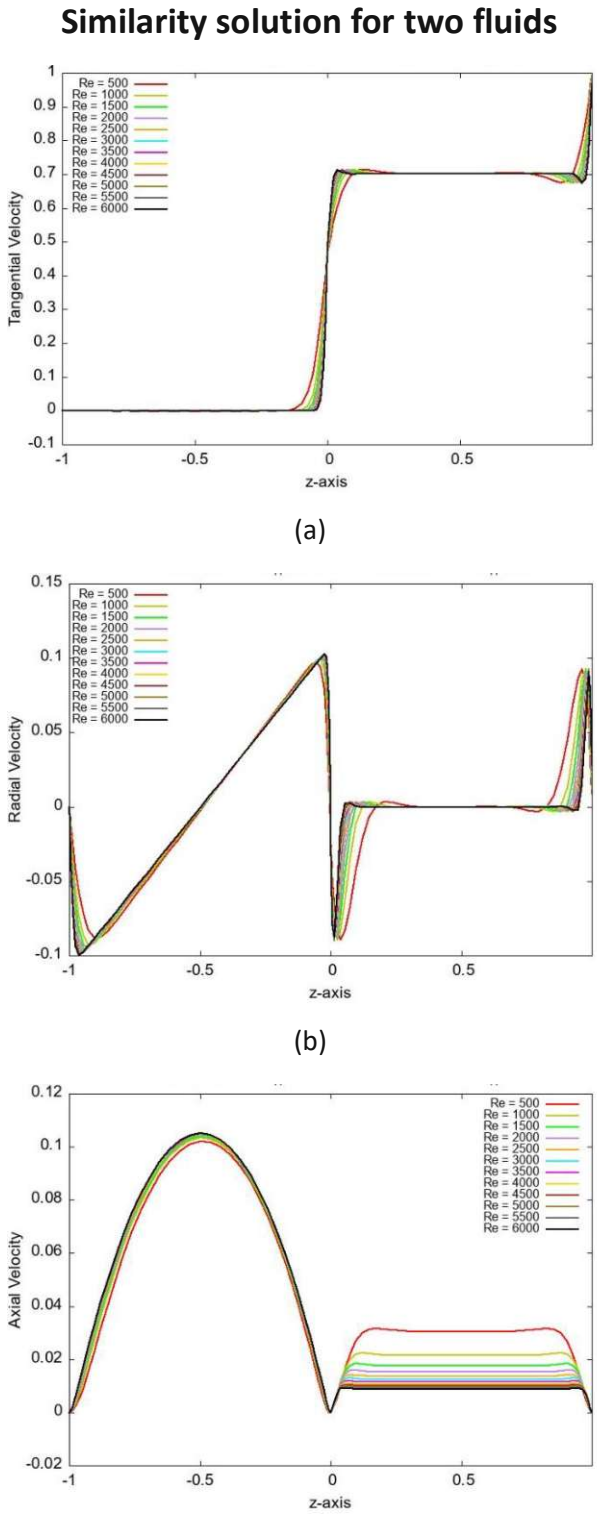

Figure 34:Velocity components in Two Immiscible Fluids Similarity Solution with 80-Node Mesh Across Various Reynolds Numbers, Density Ratio 2, and Viscosity Ratio 0.5. (a) Tangential velocity (b) Radial Velocity (c) Axial Velocity

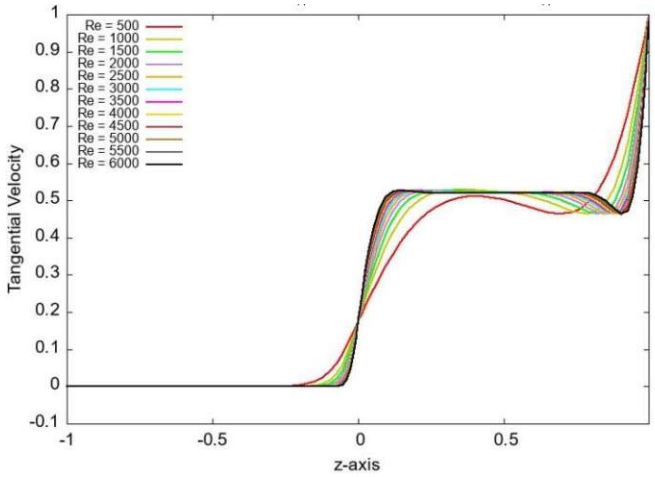

(a)

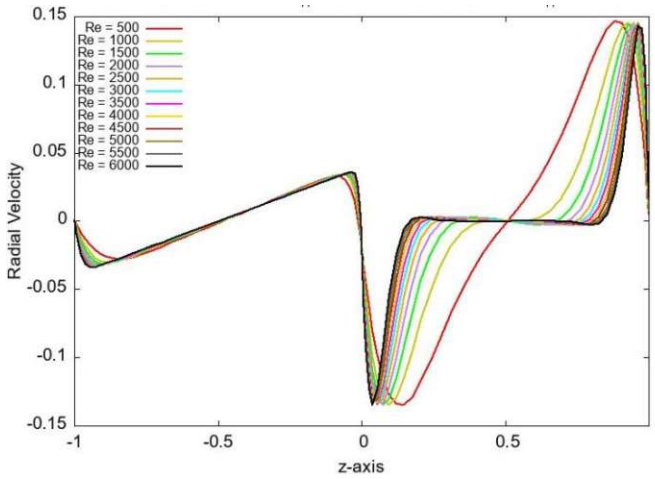

(b)

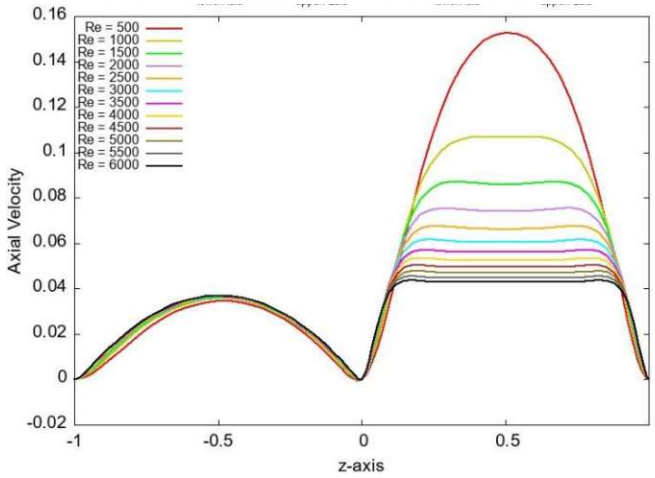

(c)

Figure 35: Velocity components in Two Immiscible Fluids Similarity Solution with 80-Node Mesh Across Various Reynolds Numbers, Density Ratio 25, and Viscosity Ratio 1. (a) Tangential velocity (b) Radial Velocity (c) Axial Velocity

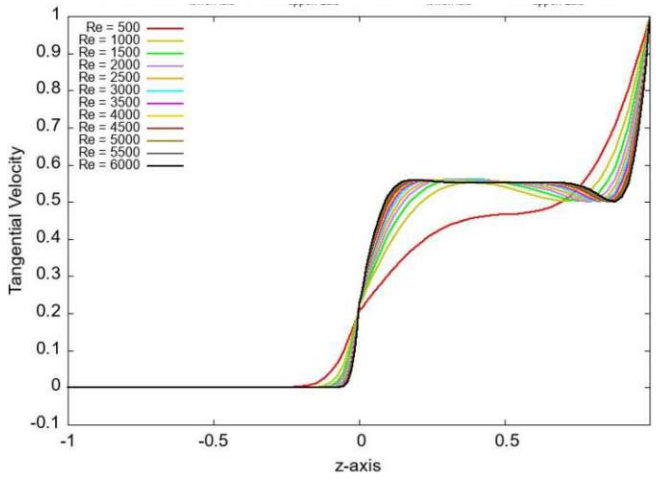

(a)

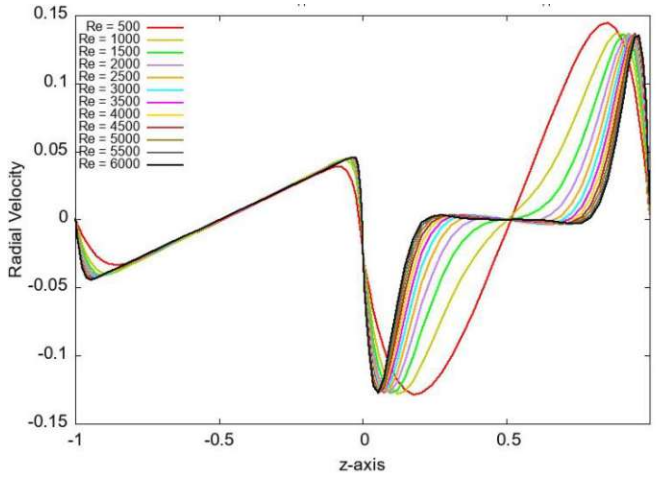

(b)

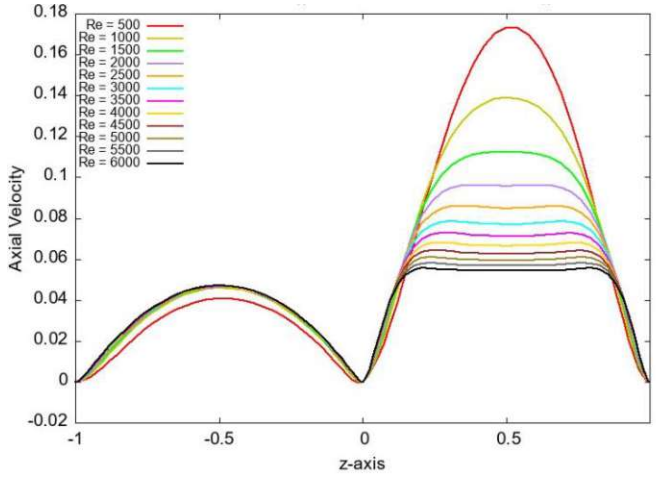

(c)

Figure 36: Velocity components in Two Immiscible Fluids Similarity Solution with 80-Node Mesh Across Various Reynolds Numbers, Density Ratio 25, and Viscosity Ratio 0.5. (a) Tangential velocity (b) Radial Velocity (c) Axial Velocity

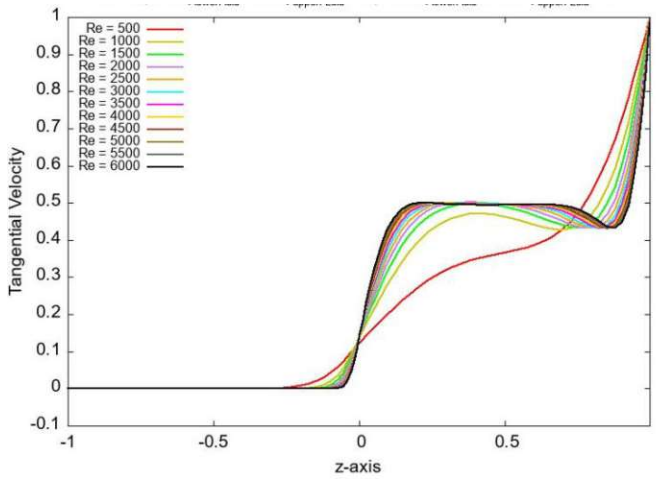

(a)

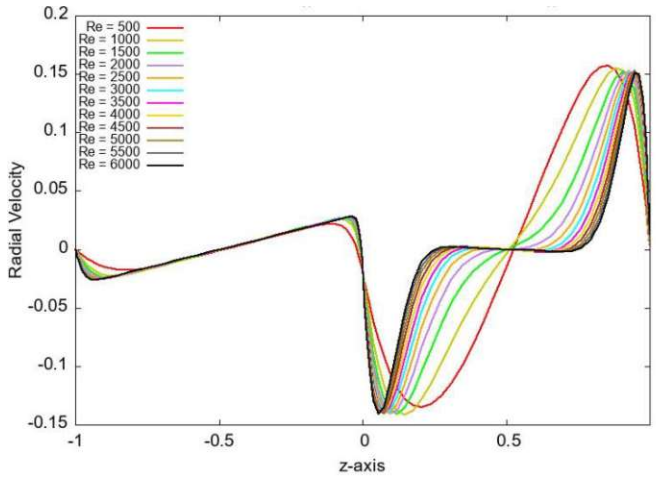

(b)

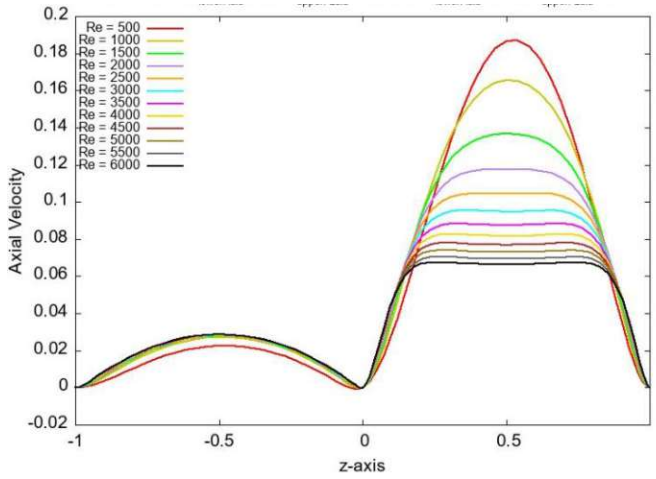

(c)

Figure 37: Velocity components in Two Immiscible Fluids Similarity Solution with 80-Node Mesh Across Various Reynolds Numbers, Density Ratio 50, and Viscosity Ratio 1. (a) Tangential velocity (b) Radial Velocity (c) Axial Velocity

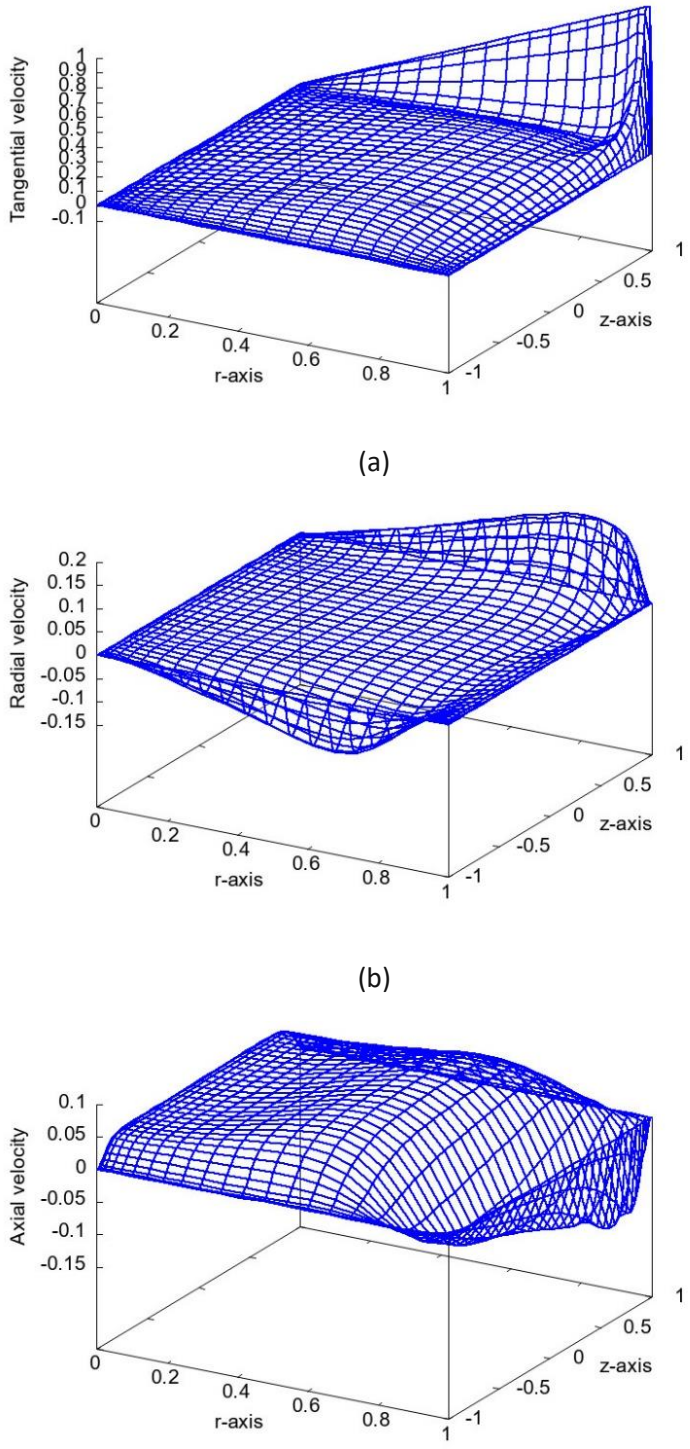

Figure 38: Velocity components in Single Fluid at Re = 1000: Mesh grid (25r x 40z). (a) Tangential velocity (b) Radial Velocity (c) Axial Velocity

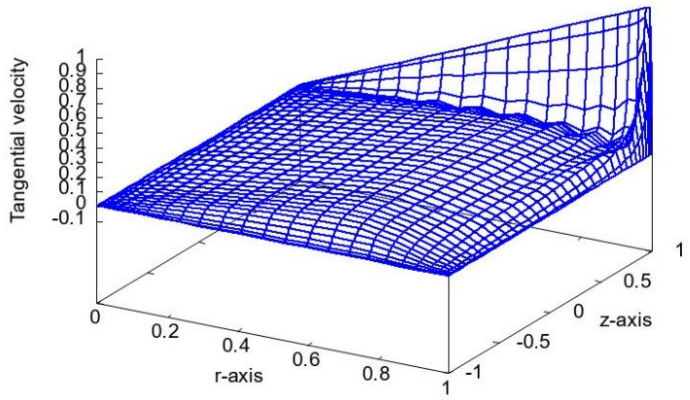

(a)

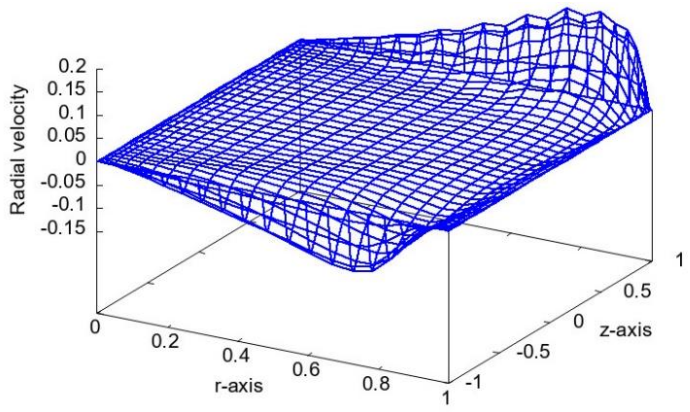

(b)

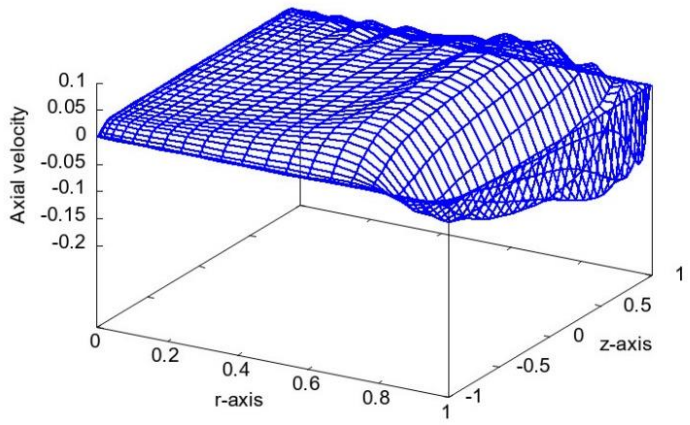

(c)

Figure 39: Velocity components in Single Fluid at Re = 3000: Mesh grid (25r x 40z). (a) Tangential velocity (b) Radial Velocity (c) Axial Velocity

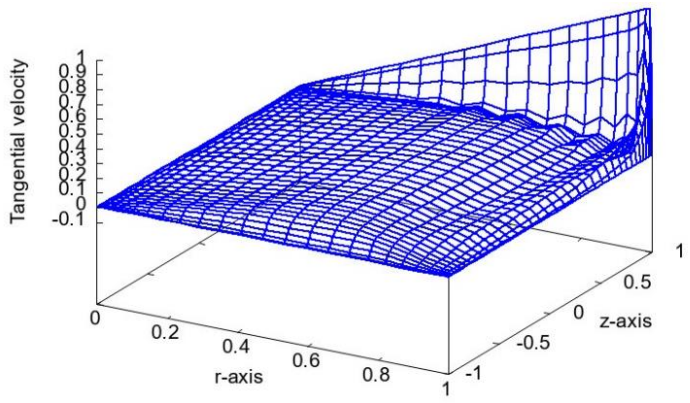

(a)

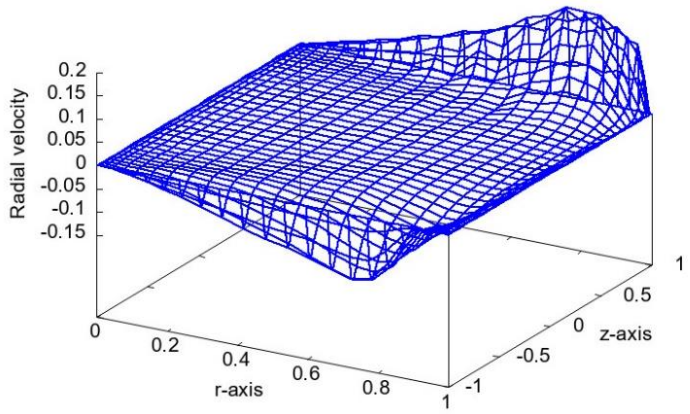

(b)

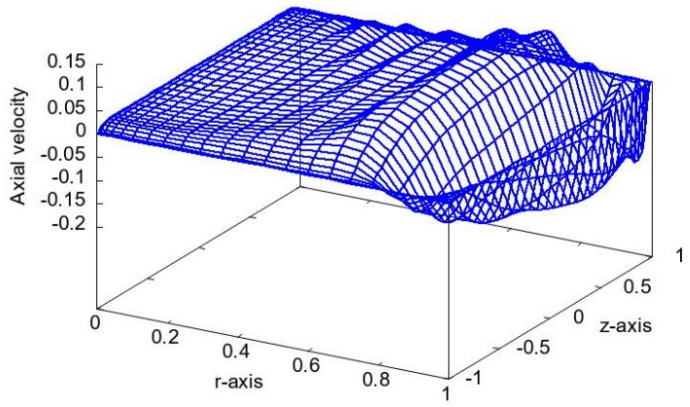

(c)

Figure 40: Velocity components in Single Fluid at Re = 5000: Mesh grid (25r x 40z). (a) Tangential velocity (b) Radial Velocity (c) Axial Velocity

Velocity components by non-similarity solution for two immiscible fluids

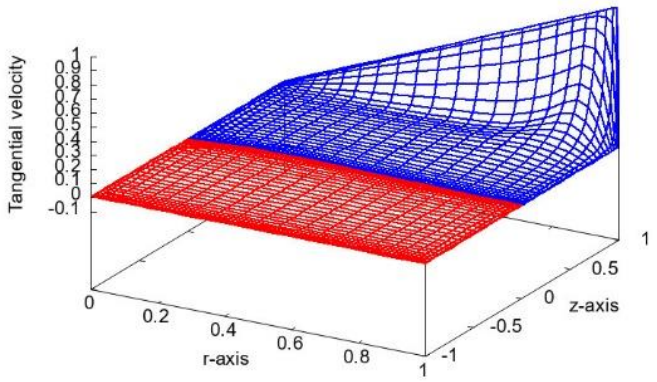

(a)

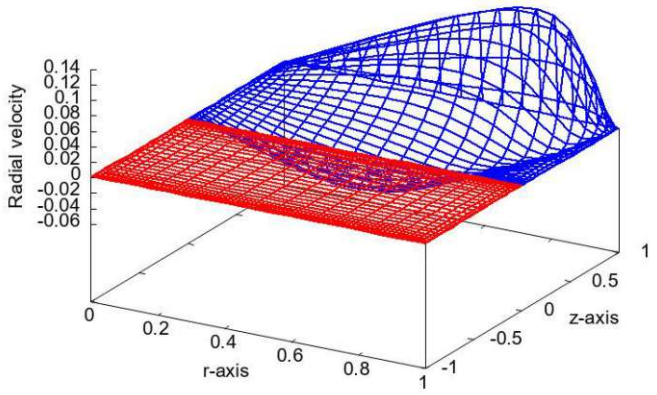

(b)

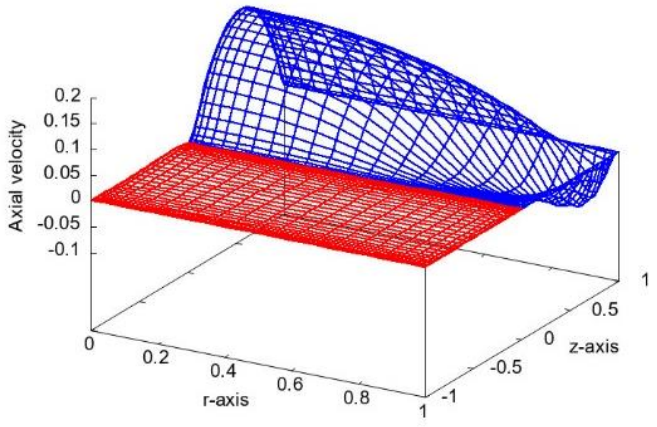

(c)

Figure 41: Velocity components in Two Immiscible Fluids at Re=500, with a Density Ratio of 2 and Dynamic Viscosity Ratio of 0.5. Mesh Grid: Nr=25, $Nz_{UpFluid}$=30, $Nz_{downfluid}$=30. (a) Tangential velocity (b) Radial Velocity (c) Axial Velocity

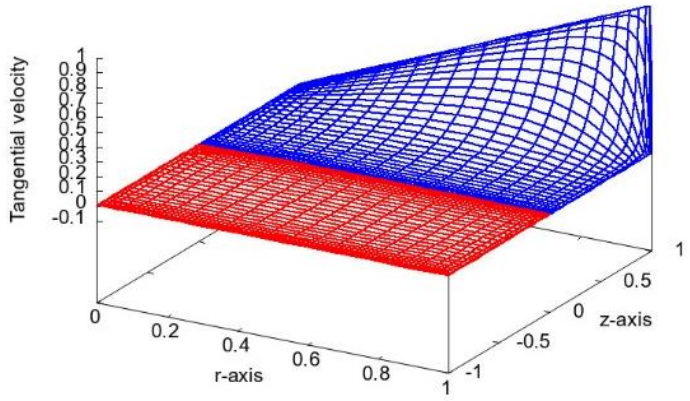

(a)

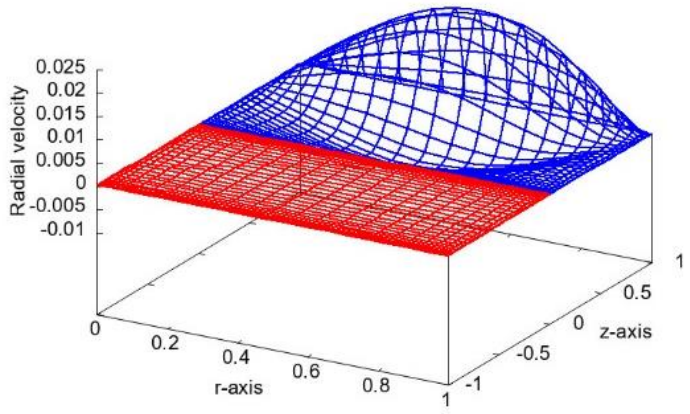

(b)

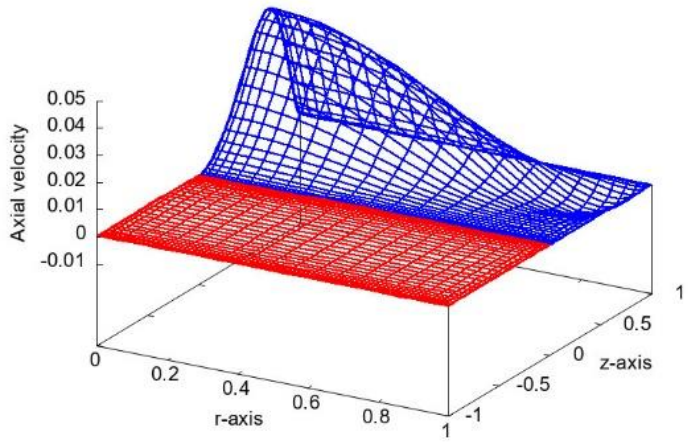

(c)

Figure 42: Velocity components in Two Immiscible Fluids at Re=500, with a Density Ratio of 50 and Dynamic Viscosity Ratio of 0.5. Mesh Grid: Nr=25, $Nz_{UpFluid}$=30, $Nz_{downfluid}$=30. (a) Tangential velocity (b) Radial Velocity (c) Axial Velocity

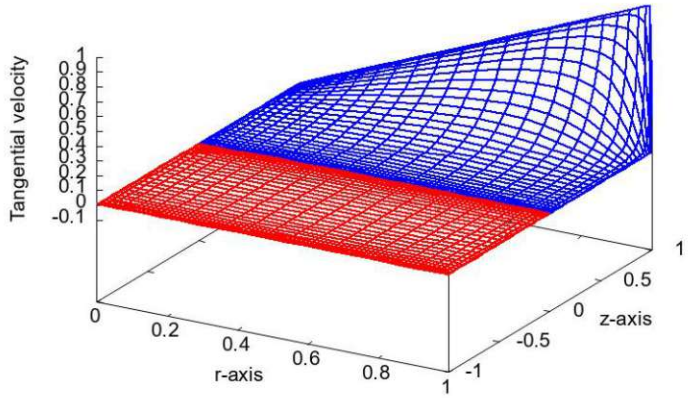

(a)

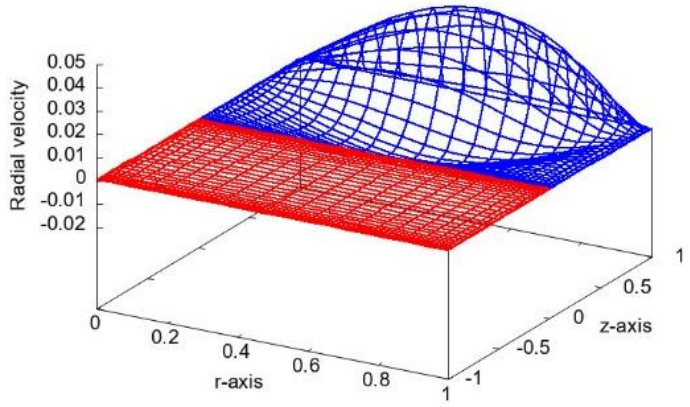

(b)

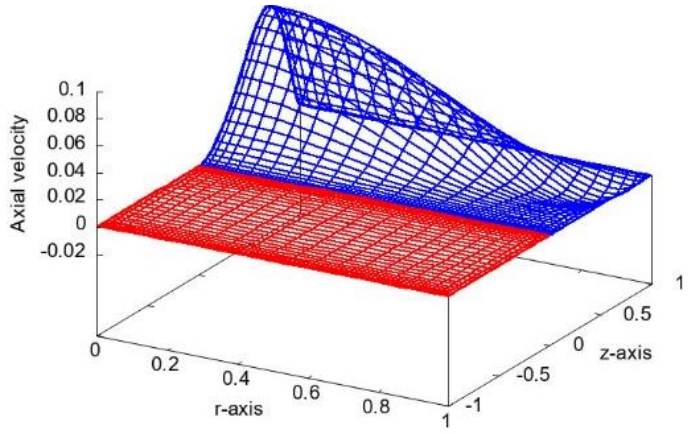

(c)

Figure 43: Velocity components in Two Immiscible Fluids at Re=500, with a Density Ratio of 50 and Dynamic Viscosity Ratio of 1. Mesh Grid: Nr=25, $Nz_{UpFluid}$=30, $Nz_{downfluid}$=30. (a) Tangential velocity (b) Radial Velocity (c) Axial Velocity

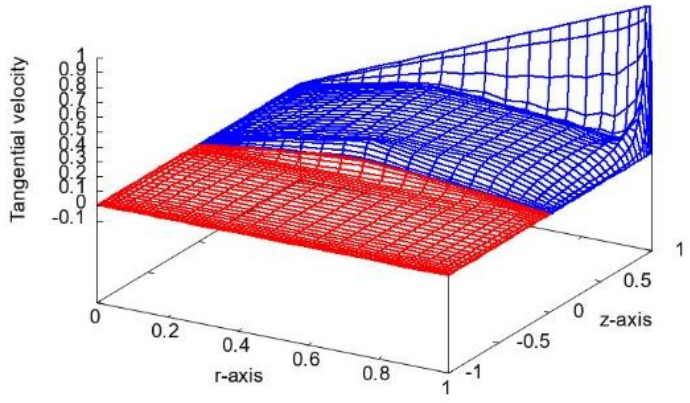

(a)

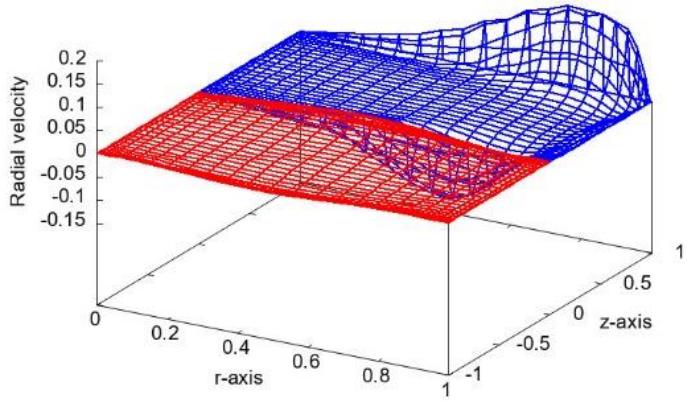

(b)

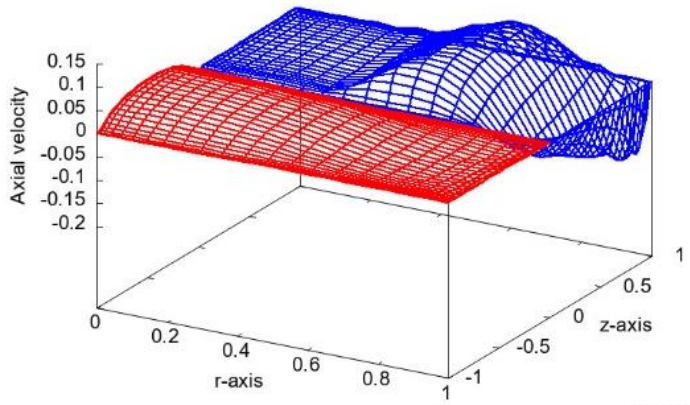

(c)

Figure 44: Velocity components in Two Immiscible Fluids at Re=3000, with a Density Ratio of 2 and Dynamic Viscosity Ratio of 1. Mesh Grid: Nr=25, $Nz_{UpFluid}$=30, $Nz_{downfluid}$=30. (a) Tangential velocity (b) Radial Velocity (c) Axial Velocity

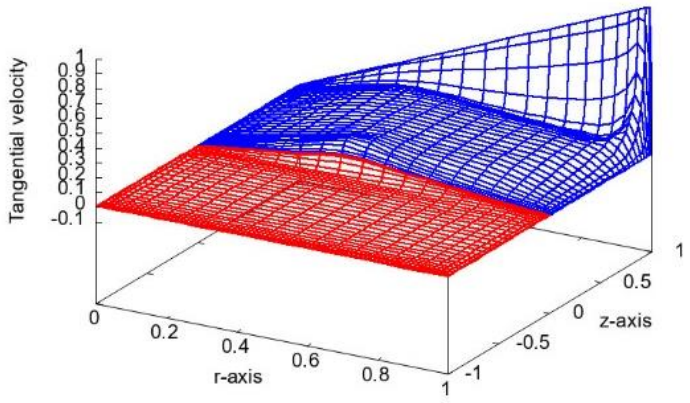

(a)

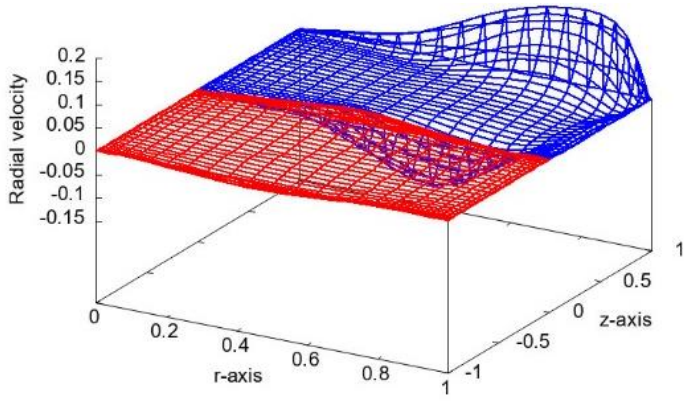

(b)

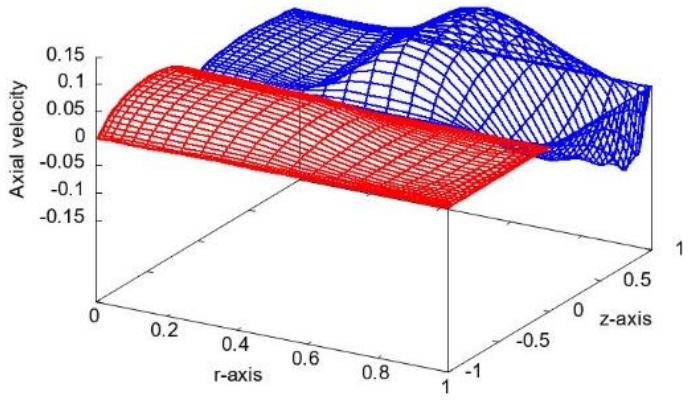

(c)

Figure 45: Velocity components in Two Immiscible Fluids at Re=3000, with a Density Ratio of 2 and Dynamic Viscosity Ratio of 0.5. Mesh Grid: Nr=25, $Nz_{UpFluid}$=30, $Nz_{downfluid}$=30. (a) Tangential velocity (b) Radial Velocity (c) Axial Velocity

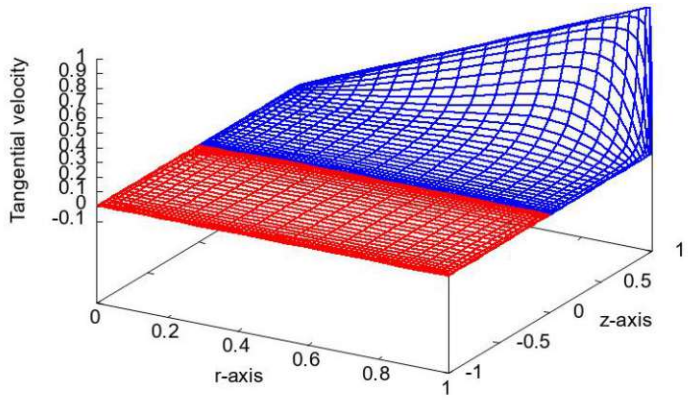

(a)

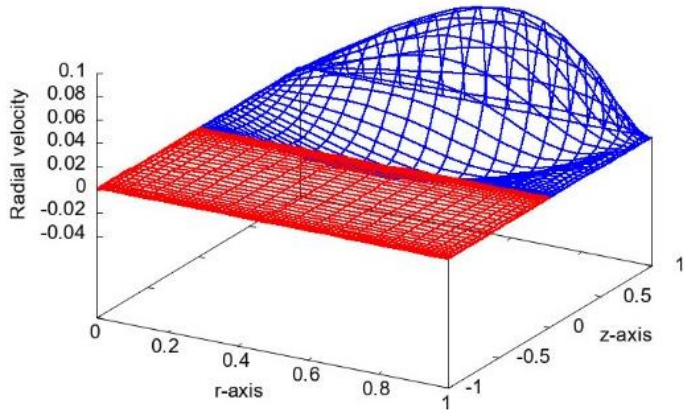

(b)

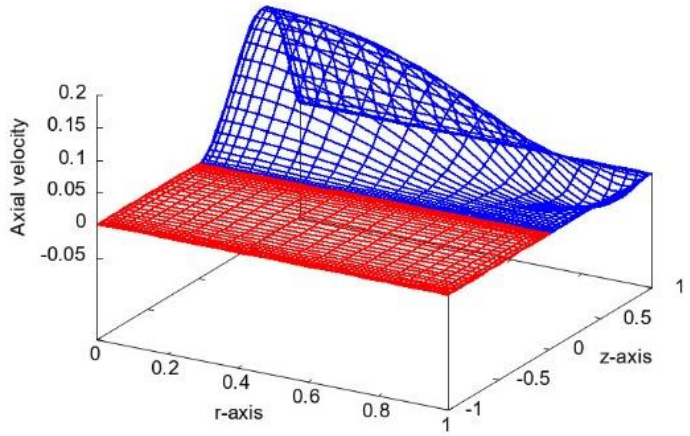

(c)

Figure 46: Velocity components in Two Immiscible Fluids at Re=3000, with a Density Ratio of 50 and Dynamic Viscosity Ratio of 0.5. Mesh Grid: Nr=25, $Nz_{UpFluid}$=30, $Nz_{downfluid}$=30. (a) Tangential velocity (b) Radial Velocity (c) Axial Velocity

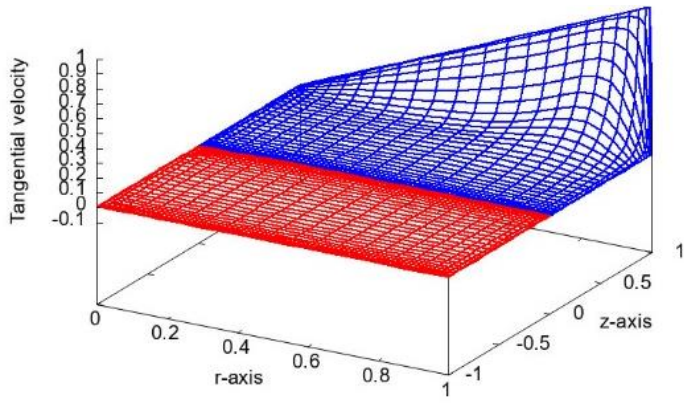

(a)

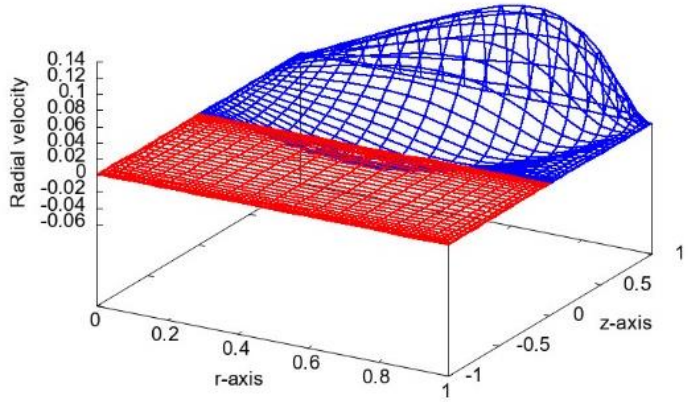

(b)

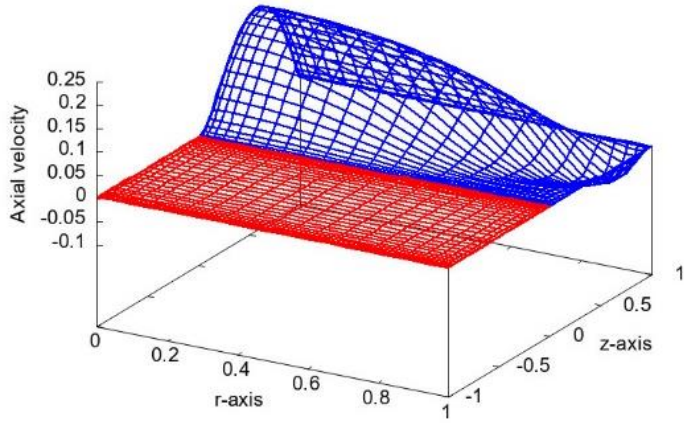

(c)

Figure 47: Velocity components in Two Immiscible Fluids at Re=3000, with a Density Ratio of 50 and Dynamic Viscosity Ratio of 1. Mesh Grid: Nr=25, $Nz_{UpFluid}$=30, $Nz_{downfluid}$=30. (a) Tangential velocity (b) Radial Velocity (c) Axial Velocity

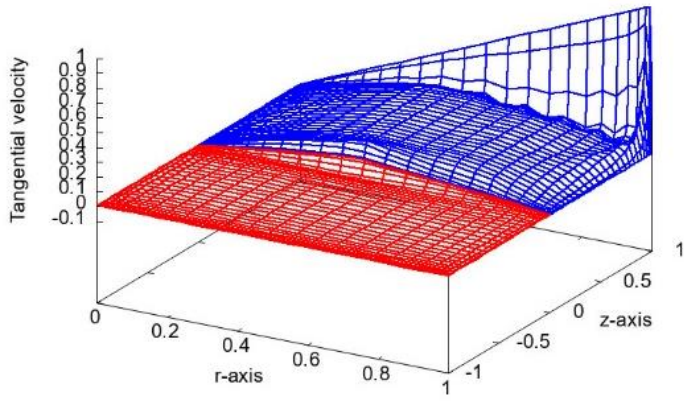

(a)

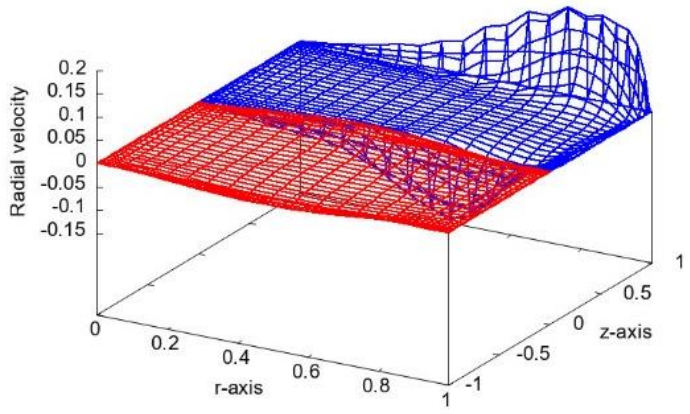

(b)

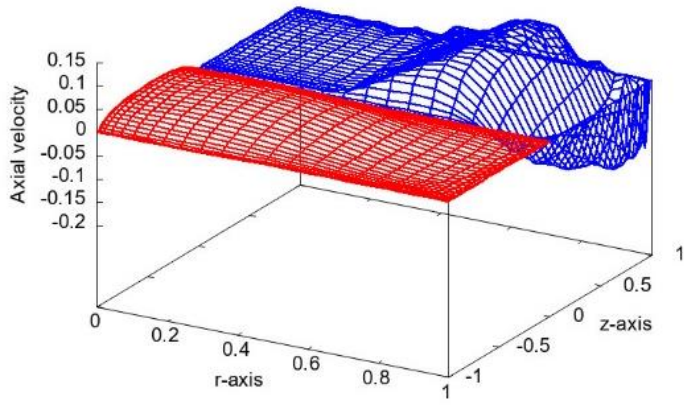

(c)

Figure 48:Velocity components in Two Immiscible Fluids at Re=6000, with a Density Ratio of 2 and Dynamic Viscosity Ratio of 1. Mesh Grid: Nr=25, $Nz_{UpFluid}$=30, $Nz_{downfluid}$=30. (a) Tangential velocity (b) Radial Velocity (c) Axial Velocity

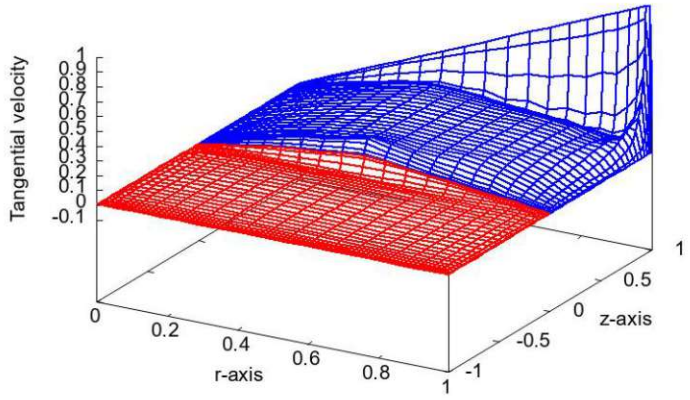

(a)

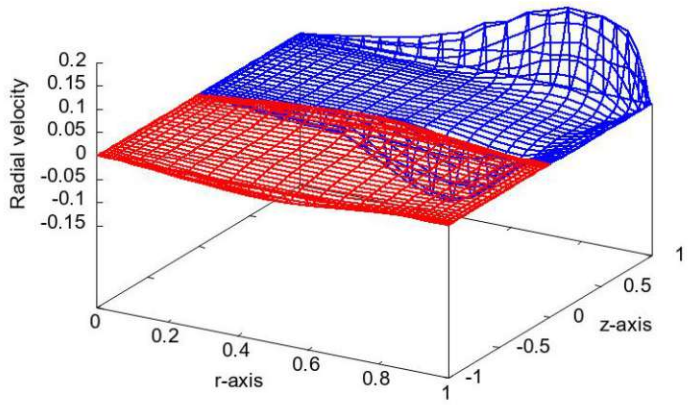

(b)

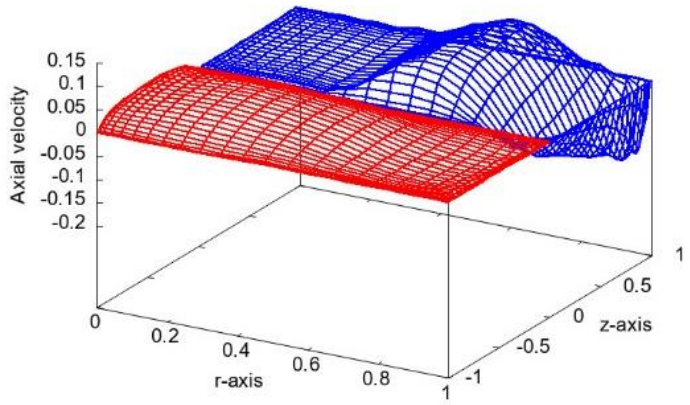

(c)

Figure 49: Velocity components in Two Immiscible Fluids at Re=6000, with a Density Ratio of 2 and Dynamic Viscosity Ratio of 0.5. Mesh Grid: Nr=25, $Nz_{UpFluid}$=30, $Nz_{downfluid}$=30. (a) Tangential velocity (b) Radial Velocity (c) Axial Velocity

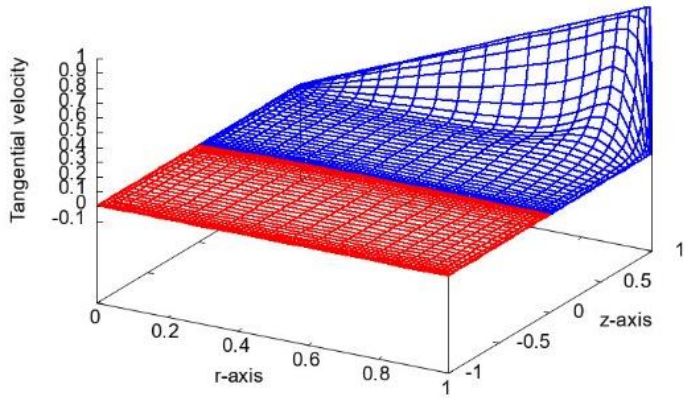

(a)

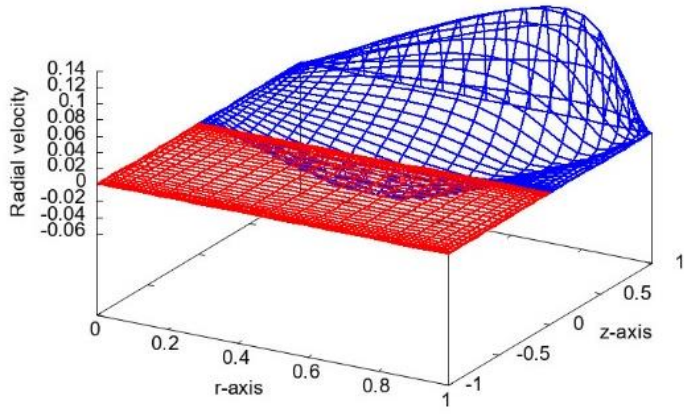

(b)

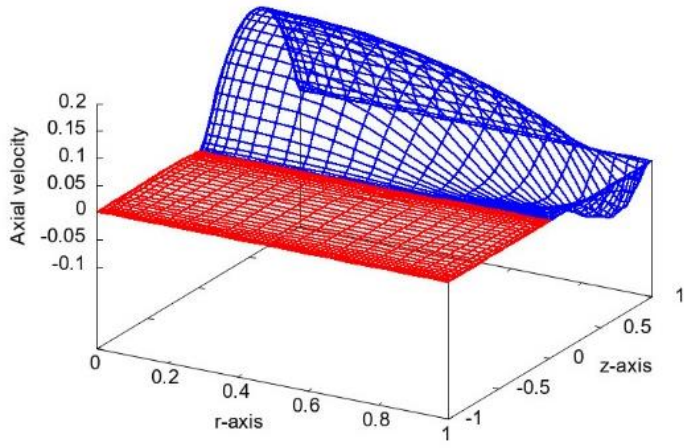

(c)

Figure 50: Velocity components in Two Immiscible Fluids at Re=6000, with a Density Ratio of 50 and Dynamic Viscosity Ratio of 1. Mesh Grid: Nr=25, $Nz_{UpFluid}$=30, $Nz_{downfluid}$=30. (a) Tangential velocity (b) Radial Velocity (c) Axial Velocity